

## INFORMATION TO USERS

The most advanced technology has been used to photograph and reproduce this manuscript from the microfilm master. UMI films the original text directly from the copy submitted. Thus, some dissertation copies are in typewriter face, while others may be from a computer printer.

In the unlikely event that the author did not send UMI a complete manuscript and there are missing pages, these will be noted. Also, if unauthorized copyrighted material had to be removed, a note will indicate the deletion.

Oversize materials (e.g., maps, drawings, charts) are reproduced by sectioning the original, beginning at the upper left-hand corner and continuing from left to right in equal sections with small overlaps. Each oversize page is available as one exposure on a standard 35 mm slide or as a 17" x 23" black and white photographic print for an additional charge.

Photographs included in the original manuscript have been reproduced xerographically in this copy. 35 mm slides or 6" x 9" black and white photographic prints are available for any photographs or illustrations appearing in this copy for an additional charge. Contact UMI directly to order.



Accessing the World's Information since 1938

300 North Zeeb Road, Ann Arbor, MI 48106-1346 USA



Order Number 8809949

**Fabrication, experimental investigation and computer modeling  
of gallium arsenide nonlinear optical devices**

Warren, Mial Evans, Ph.D.

The University of Arizona, 1988

**U·M·I**  
300 N. Zeeb Rd.  
Ann Arbor, MI 48106

---



**PLEASE NOTE:**

In all cases this material has been filmed in the best possible way from the available copy. Problems encountered with this document have been identified here with a check mark .

1. Glossy photographs or pages
2. Colored illustrations, paper or print \_\_\_\_\_
3. Photographs with dark background
4. Illustrations are poor copy \_\_\_\_\_
5. Pages with black marks, not original copy
6. Print shows through as there is text on both sides of page \_\_\_\_\_
7. Indistinct, broken or small print on several pages
8. Print exceeds margin requirements \_\_\_\_\_
9. Tightly bound copy with print lost in spine \_\_\_\_\_
10. Computer printout pages with indistinct print \_\_\_\_\_
11. Page(s) \_\_\_\_\_ lacking when material received, and not available from school or author.
12. Page(s) \_\_\_\_\_ seem to be missing in numbering only as text follows.
13. Two pages numbered \_\_\_\_\_. Text follows.
14. Curling and wrinkled pages \_\_\_\_\_
15. Dissertation contains pages with print at a slant, filmed as received \_\_\_\_\_
16. Other \_\_\_\_\_  
\_\_\_\_\_  
\_\_\_\_\_

U·M·I



FABRICATION, EXPERIMENTAL INVESTIGATION AND COMPUTER  
MODELING OF GALLIUM ARSENIDE NONLINEAR OPTICAL DEVICES

by

Mial Evans Warren

---

A Dissertation Submitted to the Faculty of the  
COMMITTEE ON OPTICAL SCIENCES (GRADUATE)

In Partial Fulfillment of the Requirements  
For the Degree of

DOCTOR OF PHILOSOPHY

In the Graduate College

THE UNIVERSITY OF ARIZONA

1 9 8 8

THE UNIVERSITY OF ARIZONA  
GRADUATE COLLEGE

As members of the Final Examination Committee, we certify that we have read  
the dissertation prepared by Mial Evans Warren

entitled Fabrication, Experimental Investigation and Computer Modeling  
of Gallium Arsenide Nonlinear Optical Devices

and recommend that it be accepted as fulfilling the dissertation requirement  
for the Degree of Doctor of Philosophy

Hyatt M. Gibbs 12/31/87  
Date

Stephen Wood 31/12/87  
Date

Peeyhan Lavan 12/31/87  
Date

\_\_\_\_\_  
Date

\_\_\_\_\_  
Date

Final approval and acceptance of this dissertation is contingent upon the  
candidate's submission of the final copy of the dissertation to the Graduate  
College.

I hereby certify that I have read this dissertation prepared under my  
direction and recommend that it be accepted as fulfilling the dissertation  
requirement.

Hyatt M. Gibbs 12/31/87  
Dissertation Director Date

## STATEMENT BY AUTHOR

This dissertation has been submitted in partial fulfillment of requirements for an advanced degree at The University of Arizona and is deposited in the University Library to be made available to borrowers under rules of the Library.

Brief quotations from this dissertation are allowable without special permission, provided that accurate acknowledgment of source is made. Requests for permission for extended quotation from or reproduction of this manuscript in whole or in part may be granted by the head of the major department or the Dean of the Graduate College when in his or her judgment the proposed use of the material is in the interests of scholarship. In all other instances, however, permission must be obtained from the author.

SIGNED: Mal E. Weaver

## ACKNOWLEDGEMENTS

I would like to thank my advisor, Hyatt Gibbs, for his guidance and support during the work presented here. His enthusiasm, drive, and keen physical insight were crucial to the completion of this dissertation. In addition, I am grateful for his encouragement and understanding, and for the confidence that he has placed in me. I thank Stephan Koch for working closely with me on the computer simulations, for many enjoyable conversations, and for patiently and bravely attempting to teach me the underlying physics of the materials we work with. I would also like to thank Dror Sarid for allowing me to collaborate with his students and work in his laboratory. I am also grateful to Nasser Peyghambarian for serving on my dissertation committee, in spite of a very busy schedule, and for his helpful advice over the years.

All of the research described in this dissertation was performed in collaboration with other students and scientists. Without their help, little would have been accomplished. Special thanks are reserved for Wayne Gibbons, who worked and shared equally in the waveguide research and kept me going through many a discouragement. Keiro Komatsu also deserves many thanks. Without his experience, energy, and hard work, the fabrication of most of the devices to be discussed would not have been accomplished. I learned much more than semiconductor fabrication in working with him. Honto ni, domo arigato. Thanks to Brian McGinnis for an enjoyable collaboration on the etalon-array bistability. Thanks also to Yong Hee Lee, Jack Jewell, Doug Hendricks, "Venky" Venkatesan, Dean Richardson and Greg Olbright for fruitful collaborations, and for sharing their expertise. I've also enjoyed knowing and working with Arturo Chavez-Pirson, Chi Li Chuang, Sam Howells, Ruxiang Jin, Victor Esch and Lon Wang. There are many more than I have space to acknowledge who helped me with friendship, knowledge or assistance during my graduate education.

Finally, I would like to thank my wife, Hiroko, for her patience, support and love throughout, and for her help with the final preparation of the dissertation. My son, Lawrence, has made the last five months very memorable, and this dissertation is dedicated to him.

## TABLE OF CONTENTS

	Page
LIST OF ILLUSTRATIONS .....	6
ABSTRACT .....	9
INTRODUCTION .....	11
THEORY AND MODELING OF GaAs NONLINEAR OPTICAL DEVICES	13
Description of GaAs nonlinear properties .....	13
Modeling of nonlinear Fabry-Perot etalons .....	24
Modeling of optical logic devices .....	40
Waveguide design .....	52
FABRICATION .....	69
Microlithography .....	70
Reactive ion etching .....	77
Fabrication of etalon arrays .....	88
Fabrication of quantum dot structures .....	93
Fabrication of waveguide devices .....	98
OPTICAL EXPERIMENTS .....	105
Etalon array experiments .....	105
Waveguide experiments .....	115
CONCLUSIONS .....	127
APPENDIX A: LISTING OF DYNAMIC BISTABILITY PROGRAM ..	130
APPENDIX B: LISTING OF DIFFERENTIAL GAIN PROGRAM ....	143
APPENDIX C: PHOTOLITHOGRAPHY RECIPE .....	162
REFERENCES .....	166

## LIST OF ILLUSTRATIONS

Figure	Page
1. Representative GaAs absorption spectrum . . . . .	14
2. Simplified band structure diagram of direct-gap semiconductor . . . . .	16
3. Comparison of experimental and theoretical absorption and refractive index for GaAs . . . . .	22
4. Schematic of Fabry-Perot etalon operation . . . . .	26
5. Representative input-output characteristic of a nonlinear Fabry-Perot etalon . . . . .	28
6. Representative bistable hysteresis plot for a dispersive etalon . . . . .	30
7. Calculated GaAs absorption as a function of carrier density at 885 nm . . . . .	31
8. Calculated GaAs change in refractive index as a function of carrier density at 885 nm . . . . .	32
9. Switch-up intensity and transmitted intensity from steady-state calculations . . . . .	34
10. Input intensity versus output intensity for a steady-state simulation of a nonlinear etalon . . . . .	35
11. Time-dependent calculation of transmitted intensity versus input intensity for a 2- $\mu\text{m}$ thick etalon . . . . .	36
12. Reflected intensity versus input intensity for a 2- $\mu\text{m}$ thick etalon . . . . .	37
13. A series of experimental loops for a 2- $\mu\text{m}$ thick GaAs etalon . . . . .	39
14. Latched AND gate modeled for a GaAs etalon . . . . .	42

LIST OF ILLUSTRATIONS—Continued

Figure	Page
15. Modeling of pulse-timing effects for AND gate operation with coincident pulses . . . . .	44
16. Modeling of pulse-timing effects for AND gate operation with one pulse delayed 10 ns . . . . .	45
17. Modeling of pulse-timing effects for AND gate operation with one pulse delayed 20 ns . . . . .	46
18. Differential energy gain versus switch-pulse intensity for different ratios of temporal pulse width to carrier relaxation time $\tau$ . . . . .	49
19. Three-layer slab waveguide geometry . . . . .	55
20. Illustration of ridge waveguide and strip-loaded waveguide structures . . . . .	60
21. Division of strip-loaded waveguide structure into different effective index regions . . . . .	62
22. Four-layer slab waveguide geometry . . . . .	65
23. Calculated transmitted intensity versus input intensity for a 200- $\mu\text{m}$ thick GaAs etalon . . . . .	68
24. Illustration of main fabrication steps . . . . .	71
25. Schematic illustration of reactive ion etching chamber . . . . .	78
26. Main components of Semigroup RIE 1000 reactive ion etching system. . . . .	85
27. An etched array of 9 X 9- $\mu\text{m}$ square mesas in a 1.5- $\mu\text{m}$ thick layer of GaAs . . . . .	89
28. Micrograph of very small posts etched in a MQWS by CAIBE . . . . .	94
29. Micrograph of very small posts etched in bulk GaAs by CAIBE . . . . .	95

LIST OF ILLUSTRATIONS--Continued

Figure	Page
30. Micrograph of very small posts etched in GaAs by RIE. . . . .	96
31. Cross section of ridge waveguides . . . . .	98
32. Structure of samples grown by MBE at NEC in Japan . . . . .	100
33. Strip-loaded waveguide structure . . . . .	101
34. Micrograph of strip-loaded waveguide . . . . .	102
35. Micrograph of nonlinear directional coupler . . . . .	103
36. NOR-gate response of 76 Å MQWS etalon . . . . .	106
37. Experimental setup for streak-camera observation of fast, two-wavelength NOR-gate in etalon array . . . . .	108
38. Streak-camera trace of pump pulse, AND gate transmission and NOR gate transmission. . . . .	110
39. Fast optical bistability in GaAs etalons . . . . .	113
40. Experimental setup for observation of optical bistability in waveguides . . . . .	116
41. Hysteresis loop for increasing-absorption optical bistability in a GaAs ridge waveguide . . . . .	119
42. Optical bistability in a strip-loaded waveguide . . . . .	122
43. Bistable operation of MQWS waveguide showing switching through two orders of Fabry-Perot transmission. . . . .	123
44. Hysteresis loop showing competition between thermal and electronic nonlinear mechanisms . . . . .	125

## ABSTRACT

Nonlinear optical switching and logic devices based on GaAs nonlinear Fabry-Perot etalons have been investigated theoretically and experimentally. The theoretical modeling has been performed with the first realistic and easily computed theory of GaAs nonlinear optical properties near the band edge. Both steady-state and dynamic calculations have been performed for optical bistability with GaAs etalons. High-transmission operation is predicted for certain etalon detunings from the excitation wavelength. Various logic-gate functions have simulated with the model. An investigation of differential energy gain in transient, one-wavelength operation was performed. The conclusion is that useful differential gain is not achievable in transient, one-wavelength operation if the pulse width is less than about ten times the carrier lifetime in the material. Waveguide structures with single-mode transverse confinement were designed and optical bistability was predicted for long GaAs etalons similar to cleaved waveguides.

GaAs nonlinear optical devices were fabricated in forms of interest for application to optical parallel processing and guided wave signal processing. The fabrication work included etalon arrays and waveguide devices fabricated by reactive ion etching. The photolithography and reactive ion etching processes used and developed are described. Preliminary work on ultra-small quantum-confinement structures is described.

Optical experiments were performed on the devices fabricated. The etalon arrays demonstrated extremely fast relaxation times for GaAs etalon devices, and

demonstrated the ability to control material parameters through the fabrication process, by increasing the surface recombination rate of charge carriers. Fast optical bistability at low powers was also demonstrated in the array devices. Strip-loaded waveguides with cleaved ends were operated as optical bistable devices with conclusive evidence that the mechanism was electronic in origin. Nonlinear phase shifts of greater than  $2\pi$  were observed in some waveguides. Such large nonlinear phase shifts are of great interest for the development of other nonlinear optical waveguide devices.

## INTRODUCTION

The first observation of optical bistability in sodium vapor (McCall, Gibbs, Churchill and Venkatesan [1975]) and the subsequent observations in semiconductors (Karpushko and Sinitsyn [1978], Gibbs, McCall, Venkatesan, Gossard, Passner and Wiegmann [1979] and Miller, Smith and Johnston [1979]) and at room temperature in structures composed of gallium arsenide (GaAs) and aluminum gallium arsenide (AlGaAs) (Gibbs et al [1982]) have encouraged researchers to consider optical bistable devices as the possible basis of an all-optical switching or computing technology. This is still a largely unrealized goal, but a sizable research effort in this direction has resulted in interesting nonlinear optical devices and a better understanding of the physical principles of their operation. All-optical logic gates (Jewell et al [1985]) and studies of the origin of GaAs nonlinearities (Lee et al [1987]) are a couple of good examples of this. Optical bistability refers to a system exhibiting two possible stable optical output states for a single input value. A Fabry-Perot etalon containing a nonlinear optical material is one type of device that can exhibit optical bistability. Such a device can be an all-optical switch or logic element, as will be discussed in detail later. For a review of the physical principles and the historical development of the field of optical bistability, see Gibbs [1985].

The main emphasis of the work reported here has been to develop optical bistable structures in GaAs or GaAs-derived materials that are more suitable for the applications that have been envisioned for this technology. Two-dimensional

arrays of such devices for possible application in optical computing or parallel signal-processing systems and waveguide structures for integrated optics or optical fiber systems were studied. Besides the fabrication of these devices, the testing of their performance and the development of a computer model of the basic GaAs nonlinear Fabry-Perot etalon is also discussed.

The organization of this thesis is in three main sections. The first is a discussion of the nonlinear optical properties of GaAs, the theory of nonlinear Fabry-Perot etalons and a computer model for the GaAs etalons. The second section describes the fabrication of both etalon arrays and waveguides. The third section is an account of the optical experiments performed to date with these devices, and is divided into etalon array and waveguide experiments. A final chapter discusses the implications of the present work, and makes some recommendations for future efforts.

## THEORY AND MODELING OF GaAs NONLINEAR OPTICAL DEVICES

The optical response of a material is usually divided into two experimentally measurable quantities, its absorption and index of refraction. Both of these properties generally have a spectral dependence. In some materials, these properties may change with varying excitation intensity. Such materials are referred to as nonlinear optical materials. Only with the development of the laser has it been possible to systematically investigate optical nonlinearities and to develop devices that utilize them. This is because optical nonlinearities typically require very large fields or intensities for observation. Some semiconductors show an abrupt edge in their absorption spectrum, and large nonlinear effects are observable at relatively low intensities near this region. In this chapter we will first discuss the origin and behavior of the nonlinear optical properties of GaAs. Next is a discussion of modeling of GaAs nonlinear Fabry-Perot etalons. Last is a discussion of the design of GaAs waveguides for use in nonlinear waveguide devices and experiments.

### **Description of GaAs nonlinear properties**

The nonlinear changes in a semiconductor are changes in both the index of refraction and the optical absorption. These are actually the imaginary and real parts, respectively, of the response function of a material to electromagnetic excitation. These two properties are not independent. The absorption and index,

as a function of excitation frequency, are interrelated by the Kramers-Kronig relations (Hodgson [1970]). It is then possible to consider the origin of optical nonlinearities to be due to absorption changes in the excited material and the resulting index changes due to the Kramers-Kronig transform of the absorption spectrum. The implied causality is artificial, but simplifies the discussion.

A representative absorption spectrum of GaAs at 150 K near the band-edge

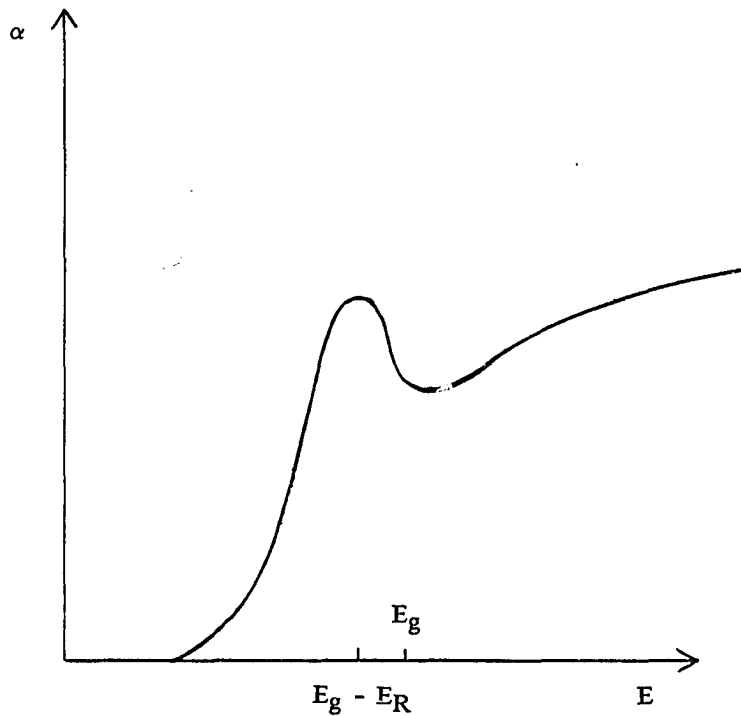


Figure 1. Representative band-edge absorption spectrum of GaAs below room temperature.

is shown in Figure 1. Going from higher excitation energy to lower, one can divide the spectrum into three regions. The interband region, with a roughly

constant absorption  $\alpha$ . An exciton region, which is a sharp peak at low temperature, but not at higher temperatures. The last is a band-tail region at lower energy that has an exponential drop in absorption as a function of energy. Each of these regions can be primarily attributed to certain absorption mechanisms.

The interband region is due to direct transitions of excited electrons from the valence band to the conduction band. The band structure of GaAs (and other similar direct-gap semiconductors) is illustrated in Figure 2. A direct-gap semiconductor has the conduction-band minima and valence-band maxima at the same point in  $k$  space. In this case transitions between the valence and conduction bands do not need additional momentum transfer interactions with phonons (the lattice). Without considering the Coulomb interaction between the excited electrons and holes, the absorption edge would occur exactly at the energy-gap minimum and the absorption would have a  $\sqrt{E}$  dependence.

In reality, the Coulomb forces between the charged carriers are very significant. Electrons in the conduction band and holes in the valence band are able to form bound states called excitons. In the Wannier approximation, the exciton has a binding energy and Bohr radius like a hydrogen atom. In a relatively large-gap semiconductor like GaAs, the binding energy is weak, about 4.2 meV, and the Bohr radius is approximately  $140 \text{ \AA}$ . The binding energy of the exciton is often used as a unit of energy and referred to as a Rydberg,  $E_R$ . In a pure semiconductor at absolute zero, the exciton absorption would appear as a Rydberg series of lines below the interband absorption edge with a continuum at the band edge. In real semiconductors at higher temperatures, the lines are broadened, and often merge into a single feature due to interactions with impurities and phonons. Phonon interactions are the most important broadening

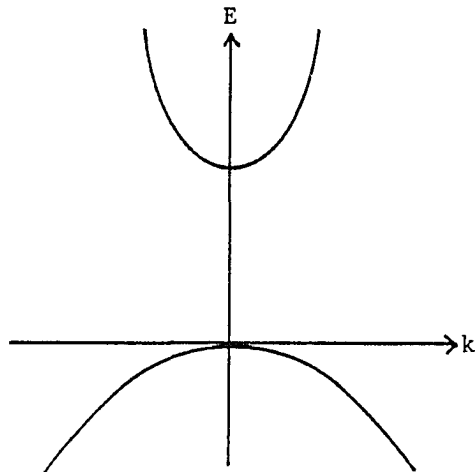


Figure 2. Simplified band structure of a direct-gap semiconductor.

mechanism in materials of high purity (Chemla and Miller [1985]). This broadened absorption line is prominent in Figure 1. At room temperature in bulk GaAs, the exciton feature is significantly broadened and often not resolvable, but it still contributes to the band-edge absorption. The full-width at half-maximum of the exciton line in bulk GaAs at room temperature is very nearly one Rydberg (Alperovich, Zaletin, Kravchenko and Terekhov [1976]).

Going to lower energy from the exciton absorption, the absorption is seen to fall-off with an exponential dependence. This is referred to as the band-tail or Urbach-tail region after its discoverer (Urbach [1953]). It is a nearly universal

behavior seen in many materials, including almost all semiconductors. The absorption tail has been attributed to excitonic interactions. Redfield and Dow [1972] have attributed it to ionization of the exciton by interactions with the Coulomb fields due to impurities, lattice vibrations, etc. Sumi and Toyozawa [1971] attribute the band tail to self-trapping of the exciton.

There are other possible contributions to the absorption edge of a semiconductor that have not been included in this description. Two-photon absorption is one such mechanism.

There are two fundamentally different nonlinear mechanisms at the band-edge of GaAs. The first we will consider is band filling. As direct transitions occur, the allowed electron and hole states become filled. Further transitions into those states are blocked by the exclusion principle, and consequently the absorption contribution due to direct interband transitions become saturated for that excitation energy. Of course, the carriers occupy these states for a finite lifetime.

The other mechanism is due to coulomb interactions between the charge carriers. Two resulting effects are bandgap renormalization and screening of the excitons. Both are caused by many-body effects in the system of excited electrons and holes. In bandgap renormalization electrons or holes are able to redistribute themselves within their bands in order to minimize their energy. This energy is partially due to their mutual intraband Coulomb repulsion (correlation) and the exclusion principle (exchange). By assuming a correlated state, the electrons and holes are able to lower their total energy below that of the uncorrelated state (Haug and Schmitt-Rink [1985]). The overall effect is called bandgap renormalization, because the bandgap is defined as the difference between the electron energy and hole energy at  $k=0$ .

A charged particle surrounded by other particles of opposite charge has a reduced Coulomb field due to superposition of the fields of the other particles. This effect is referred to as screening. The attraction between an electron and hole to produce an exciton can be reduced by intraband Coulomb effects, mostly from other free carriers and excitons. Since increasing screening reduces the binding between the electron and hole, there is eventually a carrier density at which a bound state is no longer possible in a 3-dimensional material. The carrier density for which this occurs is referred to as the Mott density and roughly corresponds to the density at which there is one excited electron for each exciton volume ( $a_0^3$ ) of material (Mott [1974]). An interesting fact is that the exciton feature is not observed to shift position in bulk GaAs as the carrier density increases. Although the exciton binding energy ( $E_{bx}$ ) is reduced by the screening effects, the band-gap energy ( $E_g$ ) is also reduced a similar amount by bandgap renormalization. The exciton position in the absorption spectrum is given by the difference:

$$\hbar\omega = E_g - E_{bx}$$

and remains excitation independent. (Fehrenbach, Schafer, Treusch and Ulbrich [1982]).

The combined effects of the nonlinear changes in band-edge absorption change the index of refraction as well. The changes in both absorption and index of refraction are illustrated in Figure 3, as computed using the plasma theory and measured experimentally (Lee et al [1987]).

The previous discussion of nonlinear optical effects was for bulk GaAs in particular. The modeling of nonlinear optical devices that will be discussed later was based on a theoretical model of the band-edge nonlinearities of bulk GaAs. Some of the experimental work reported was performed with devices fabricated with multiple-quantum-well-structures (MQWS). Consequently, a brief discussion of what MQWS are and how their optical properties differ from bulk GaAs is in order.

MQWS are composed of alternating epitaxial layers of two compositionally different semiconductors. In this case the layers are GaAs and  $\text{Al}_x\text{Ga}_{1-x}\text{As}$ . The mole fraction of aluminum is  $x \cong 0.30$ , which gives a good lattice match with GaAs and a bandgap difference of 0.37 eV (Casey and Panish [1978]). The alternating bandgap energies in one direction gives one-dimensional confinement to carriers in the GaAs layers. The carriers are unconfined in the other two dimensions. The optical properties of MQWS are different from those of bulk GaAs because of the highly anisotropic nature of the structure and because of the one-dimensional confinement.

If the GaAs layers are thinner than the exciton diameter, the confinement increases the exciton binding energy but not the phonon-broadened linewidth. The optimum enhancement of the exciton absorption for the layer thickness  $L_z$  is for  $0.5a_0 < L_z < a_0$ . (Chemla, Miller, Smith, Gossard and Wiegmann [1984]) There is some inhomogeneous broadening introduced by variations in the layer thickness. The exciton feature can be readily observable at room temperature for such MQWS, and is shifted to higher energy compared with bulk GaAs because of the quantum confinement effects. In addition to enhancement of the exciton feature, it is also split into two peaks. The anisotropy of the MQWS splits the degeneracy

of the upper valence band resulting in two different hole subbands. One is referred to as the heavy hole and the other as the light hole, according to the differences in their effective masses. In a high quality MQWS with thin wells, this splitting can be observed in the absorption spectrum. Recent measurements on MQWS with different well thicknesses have shown that the change in refractive index  $\Delta n$ , achievable with a given carrier density increases as the well thickness decreases (Park et al [1987]). Because of the quasi-two-dimensional nature of the excitons and carriers in the MQWS, the mechanisms for the nonlinear changes are somewhat different. Phase-space filling becomes a more important factor than band filling and screening for the apparent saturation of the exciton resonance (Schmitt-Rink, Chemla and Miller [1985] and Haug and Schmitt-Rink [1984]).

The highly anisotropic nature of MQWS introduces a polarization dependence in the optical properties of MQWS. The previous discussion was for the absorption spectrum of MQWS in which the light is propagating with its polarization parallel to the quantum well layers. Measurements by Weiner et al [1985] with single-quantum-well waveguides have shown that for light polarized perpendicular to the quantum wells, the absorption edge is apparently blue-shifted because the holes in the valence band are once again degenerate.

The theory of the band-edge nonlinearities of GaAs is well established, but it is still under development for MQWS. A quantum-mechanical Green's-function theory has been developed for the band edge of bulk GaAs (Haug and Schmitt-Rink [1984] and Haug [1988]). Although successful, the theory is computationally involved and cumbersome. A simpler, semi-empirical approach has been developed by Banyai and Koch [1986]. Without going into the details of the

theory, one can briefly describe it as an extension of Elliott's theory for band-edge absorption (Elliott [1957]). The Elliot theory was successful for low temperatures and vanishingly small carrier densities. The Banyai-Koch theory extends Elliott's result to arbitrary carrier densities and temperatures through inclusion of the many-body Coulomb effects. The theory assumes the electrons and holes are in quasi-equilibrium, which is reasonable for room-temperature operation and pulse lengths greater than a few picoseconds. The generalized Elliot formula for the semiconductor absorption given by Banyai and Koch is:

$$\alpha(\omega) = a_0 A(\omega) \sum_{\lambda} |\Phi_{\lambda}(\mathbf{r}=0)|^2 \delta_{\Gamma}(\hbar\omega - E_{\lambda})$$

where  $A(\omega) = \tanh \{[\hbar\omega - \mu(N)]/2k_B T\}$  is a band-filling factor.  $\mu$  is the sum of the chemical potentials for the electrons and holes. If  $\mu > \hbar\omega > E_g$ , the medium exhibits optical gain.  $k_B$  is the Boltzman constant and  $T$  the absolute temperature. The  $\Phi_{\lambda}$  are the eigenstates and the  $E_{\lambda}$  are the eigenvalues of the Wannier equation with a screened Coulomb interaction.  $\delta_{\Gamma}$  is an exciton lineshape function that is chosen to fit the known exciton broadening and the band-tail region. The theory includes the nonlinear effects of band filling, band-gap renormalization, and exciton screening described earlier for GaAs. Previous experimental checks performed by Y. Lee et al [1987] are illustrated in Figure 3.

The Banyai-Koch theory has been used to generate values of the band-edge absorption of GaAs for different values of carrier density  $N$  and excitation energy  $\hbar\omega$ . The corresponding index of refraction changes were obtained by numerical Kramers-Kronig transformation of the absorption values. Using these tabulated

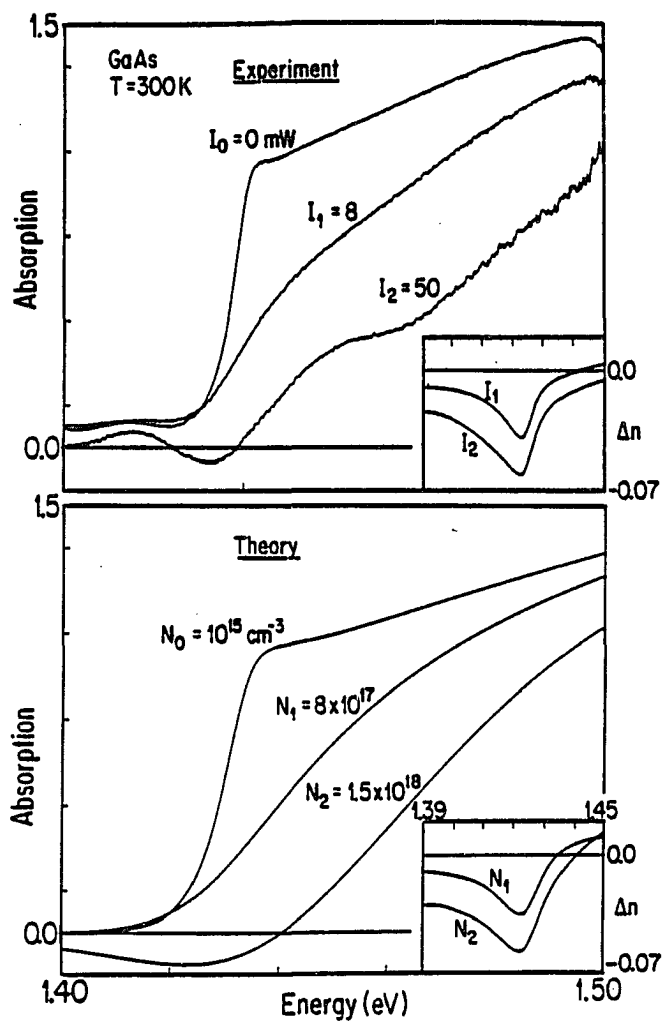


Figure 3. Comparison of experimental and theoretical absorption and refractive index spectra for room-temperature GaAs. The experimental absorption plots (a) are labeled with the excitation power in milliwatts for a  $15\text{-}\mu\text{m}$ -diameter spot on the sample. The excitation frequency is inside the absorption band. The theoretical absorption plots (b) are labeled with the electron-hole-pair densities  $N$  ( $\text{cm}^{-3}$ ). The inserts show the corresponding dispersive (refractive index) changes obtained by Kramers-Kronig transformation of the absorptive changes.

values for absorption and changes in index of refraction, it was possible to do realistic modeling of the behavior of GaAs nonlinear devices.

### Modeling of nonlinear Fabry-Perot etalons

The basic concept behind the nonlinear etalon devices is the Fabry-Perot interferometer (Born and Wolf [1970]). This device consists of two partially reflecting mirrors separated by a distance  $L$  (see Figure 4). This forms a resonant cavity. The light which is sent into the cavity undergoes multiple reflections at the mirrors, and it suffers some losses due to diffraction, transmission through the mirrors, and absorption in the material filling the space between the mirrors. If the light in the cavity is sufficiently coherent, interference will occur between the counter-propagating beams. If the light wavelength is such that an integral number of half-waves will exactly span the distance between the mirrors, the interference will be constructive. In this case, the intensity in the cavity is very high and the transmission through the etalon can be large; close to 100%, if the losses are small. If, on the other hand, the light wavelength is not in resonance with the cavity length, the light in the cavity interferes destructively and the light intensity in the cavity is low with very little transmitted through the device. To make a device that is nonlinear in its intensity dependence, it is necessary to fill the space between the mirrors with a material that has excitation-dependent absorption and index of refraction.

If we assume the Fabry-Perot cavity to be of length  $L$ , with lossless mirrors of reflectivity  $R$ , an approximate solution for the Fabry-Perot transmission can be obtained:

$$\left| \frac{E_t}{E_0} \right|^2 = (1-R)^2 \frac{1}{(e^{\alpha_{\text{tot}}L/2} - R e^{-\alpha_{\text{tot}}L/2})^2 + 4R \sin^2(\beta/2)} .$$

$E_t$  and  $E_0$  are the amplitudes of the transmitted and incident fields, respectively.  $\beta$  is the round-trip phase difference for the etalon, and  $\alpha_{\text{tot}}$  is the total, single-pass absorption in the material. To achieve this solution, one has already eliminated the field dynamics in the cavity by assuming that the resonator round-trip time for the light in the cavity is much less than the material relaxation time (Bischofberger and Shen [1979]); this is sometimes referred to as the bad-cavity limit. The spatial field variations, such as standing waves, have also been ignored by using the mean-field approximation. The various derivations of this solution are referenced in Koch, Peyghambarian and Gibbs [1987]. In the mean-field approximation,  $\alpha_{\text{tot}}$  and  $\beta$  are spatial averages over the etalon length

$$\alpha_{\text{tot}} = \frac{1}{L} \int_0^L dz \alpha[N(z)]$$

and

$$\beta/2 = - \left[ \delta + \frac{\omega}{c} \int_0^L dz \Delta n[N(z)] \right] .$$

In the latter expression,  $\delta$  contains all carrier density-independent phase shifts of the linear medium and of the mirrors and  $\Delta n$  is the carrier density-dependent

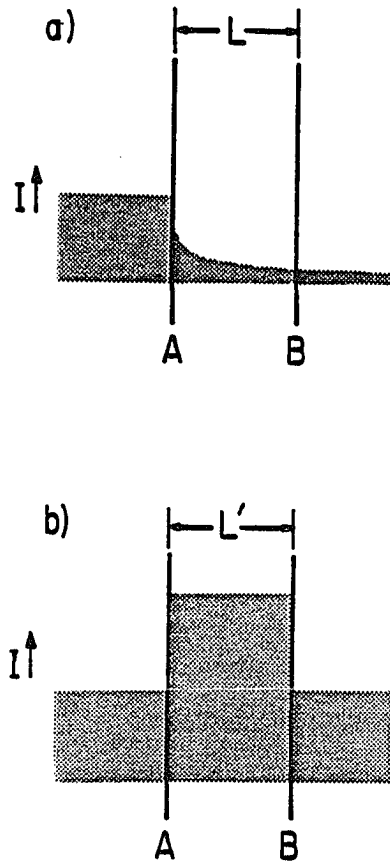


Figure 4. Schematic of Fabry-Perot etalon: in (a) separation  $L$ , between mirrors A and B, is not an integer number of half wavelengths; in (b), the separation  $L'$  is an integer number of half wavelengths. The shaded regions represent the relative light intensities before, after and inside the etalon.

change in index. In the presence of carrier diffusion, it is a good approximation to assume that the carrier density is spatially homogenous. The transmitted intensity  $I_T$  of the resonator can be written

$$I_T = I_0(1-R)^2 \frac{1}{(e^{\alpha(\omega,N)L/2} - Re^{-\alpha(\omega,N)L/2})^2 + 4R\sin^2(\delta + \omega\Delta n(\omega,N)L/c)}, \quad (1)$$

Similarly, for the reflected intensity  $I_R$ ,

$$I_R = I_0R \frac{(e^{\alpha(\omega,N)L/2} - e^{-\alpha(\omega,N)L/2})^2 + 4\sin^2(\delta + \omega\Delta n(\omega,N)L/c)}{(e^{\alpha(\omega,N)L/2} - Re^{-\alpha(\omega,N)L/2})^2 + 4R\sin^2(\delta + \omega\Delta n(\omega,N)L/c)} \quad (2)$$

where  $I_0$  is the incident intensity and  $\alpha$  and  $\Delta n$  are explicitly dependent on the excitation frequency and carrier density, as discussed earlier.

A useful concept for the Fabry-Perot etalon is the finesse of the resonator  $F$ , defined by the ratio of the separation of adjacent transmission peaks to the full width at half maximum (FWHM) of a peak. A parameter  $F$  can be defined as

$$F = \frac{4R}{(e^{\alpha L/2} - Re^{-\alpha L/2})^2}$$

which is in turn related to the finesse by  $F = \frac{4}{\pi^2} F^2$ .

If the absorption  $\alpha$  decreases with increasing carrier density, the losses in the etalon will decrease sharply, so that an initially opaque device can "switch-on" to a highly transmitting state. After the initial switch-on, the saturated absorption would give a linear device transmission. If the index of refraction changes with carrier density, so does the optical path length between the mirrors. This causes the etalon to tune in or out of resonance with a fixed light frequency. These dispersive effects can be quite varied. A nonlinear etalon can be switched-on by being initially detuned from resonance or switched-off by being initially in resonance. The device can be shifted through more than one such resonance, if

the index continues to shift for increasing carrier density without saturation. Primarily dispersive nonlinear etalons have been of the most interest for logic and switching applications. It should be noted that the reflected light from a primarily dispersive nonlinear etalon shows the complementary behavior to the transmitted light. Since these are all-optical devices, there is no need for external non-optical power sources or addressing mechanisms.

Figure 5 illustrates a typical nonlinear response of a nonlinear Fabry-Perot

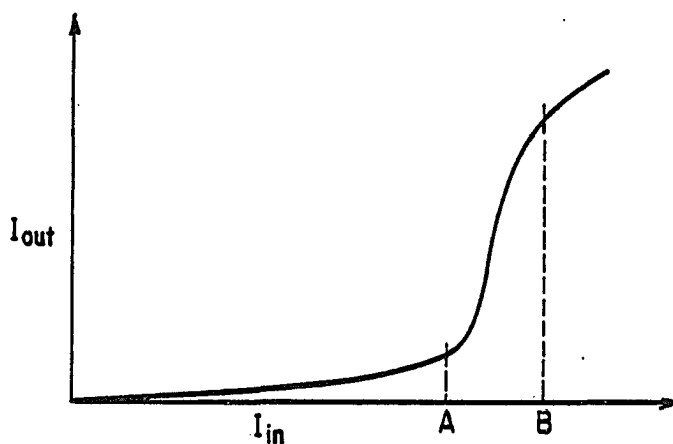


Figure 5. A representative plot of output intensity versus input intensity for a nonlinear etalon that does not exhibit bistability. The etalon is initially not in resonance with the light and is tuned into resonance with increasing intensity, so that the etalon becomes highly transmitting.

etalon. For a linearly increasing incident intensity, the transmission of the device shows a nonlinear dependence. If the nonlinear response of the material and the feedback from the etalon's mirrors are sufficient, the device will exhibit bistable

behavior. This is usually illustrated by the hysteresis behavior of the device when a pulse is incident with linearly rising and falling edges. Figure 6 shows such a hysteresis loop for a purely dispersive nonlinear material. If the device is not actually bistable, it may still exhibit a smooth hysteresis loop without the sharp switch-up and switch-down regions. As a simple example of an optical logic gate, consider the nonlinear response in Figure 5. If the total light intensity on the device is the value at point A, the transmission is low. If additional light signals are present to make the incident light intensity at point B, the device is highly transmitting. This type of response can be an AND or an OR gate depending on whether the system requires one or two light beams (representing logic values of 1) to increase the intensity from A to B. Negating functions can be performed in reflection and more complex logic operations are possible if more than one wavelength of light is used.

The intensity of light in the cavity is coupled to the change in refractive index  $\Delta n$  by the absorption of light and creation of charge carriers in the intracavity material. If the decay of the excited carriers through various recombination mechanisms is included, and one again assumes the diffusion-dominated spatially-homogeneous case, one has a differential rate equation for charge-carrier excitation and decay:

$$\frac{dN}{dt} = -\frac{N}{\tau} + \frac{\alpha(\omega, N)}{\hbar\omega} I, \quad (3)$$

where  $\tau$  is the relaxation time for the carriers and  $I$  is the light intensity inside the medium. In the case of an optical resonator,  $I$  is the internal intensity with standing wave effects assumed to be washed out by diffusion. The internal

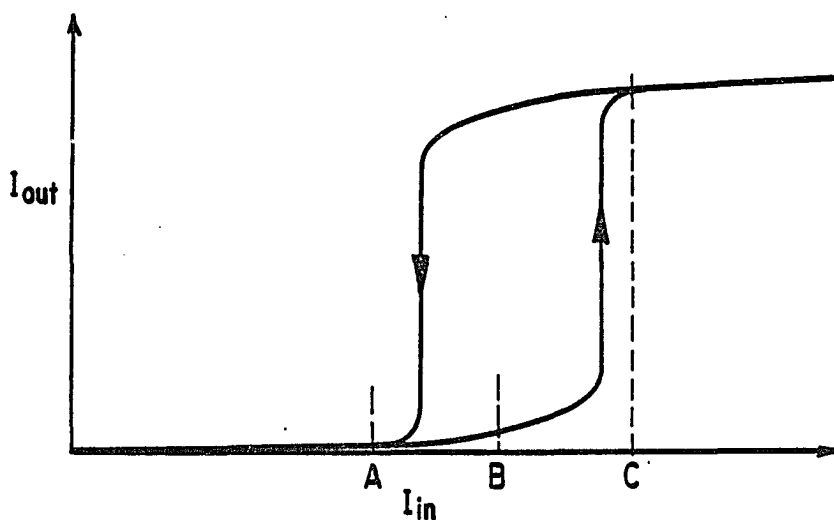


Figure 6. A representative hysteresis plot for a primarily dispersive etalon. The arrows indicate the curves followed when the device has increasing input intensity (switch-up) and decreasing input intensity (switch-down).

intensity is related to the transmitted intensity  $I_t$  by

$$I = I_t \frac{1 + R}{1 - R} . \quad (4)$$

Using the microscopic results for the optical material properties, the rate equation (3), and equations (1) and (2) for the nonlinear Fabry-Perot etalon given previously, it is possible to model semiconductor etalons. In the computer programs that have

been developed, the nonlinear optical properties of GaAs,  $\alpha(\omega, N)$  and  $\Delta n(\omega, N)$  are calculated from the Banyai-Koch plasma theory. Figures 7 and 8 illustrate calculated values for the absorption  $\alpha$  and change in index of refraction  $\Delta n$  for room-temperature GaAs as a function of carrier density  $N$  for  $\hbar\omega = 1.4039$  eV

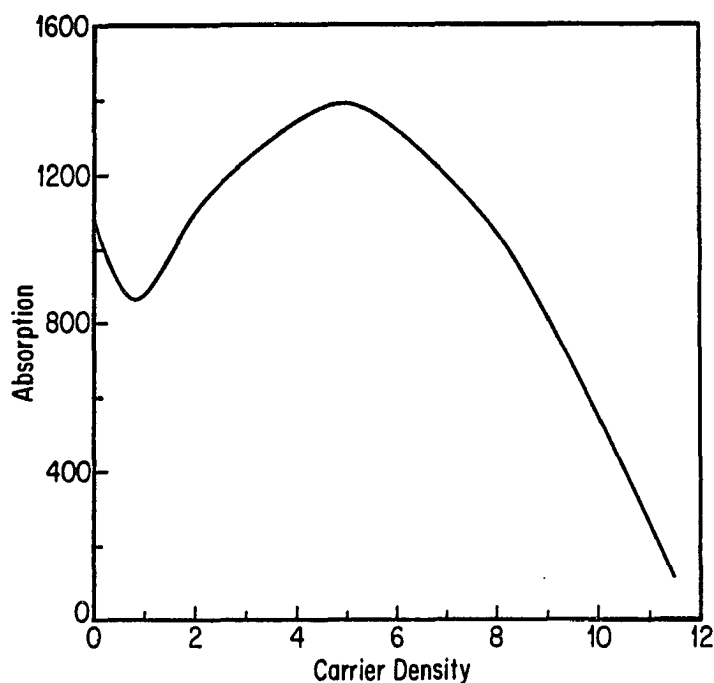


Figure 7. Calculated GaAs absorption  $\alpha$  as a function of carrier density  $N$  ( $\times 10^{17}$  cm<sup>-3</sup>) at  $-4 E_R$  below the band edge (885 nm).

excitation energy, which is four Rydbergs below the bandedge. The calculated values for a range of carrier density values  $N$  and one or two given excitation frequencies  $\omega$ , are stored in look-up tables. The coupled equations (1) and (3) are then solved numerically for a given excitation pulse or pulses using values for the

index and absorption obtained from the look-up tables by linear interpolation. The parameters in the look-up tables could easily be those calculated for a different material or perhaps obtained by experimental measurements of a material. With the model, it has been possible to explore different operating regimes and device parameters, including some that have not been tried experimentally.

The changes in the optical properties of a GaAs etalon with optical excitation can be complex. An important early goal of this project was to optimize the performance of etalon devices in terms of a few fundamental operating parameters.

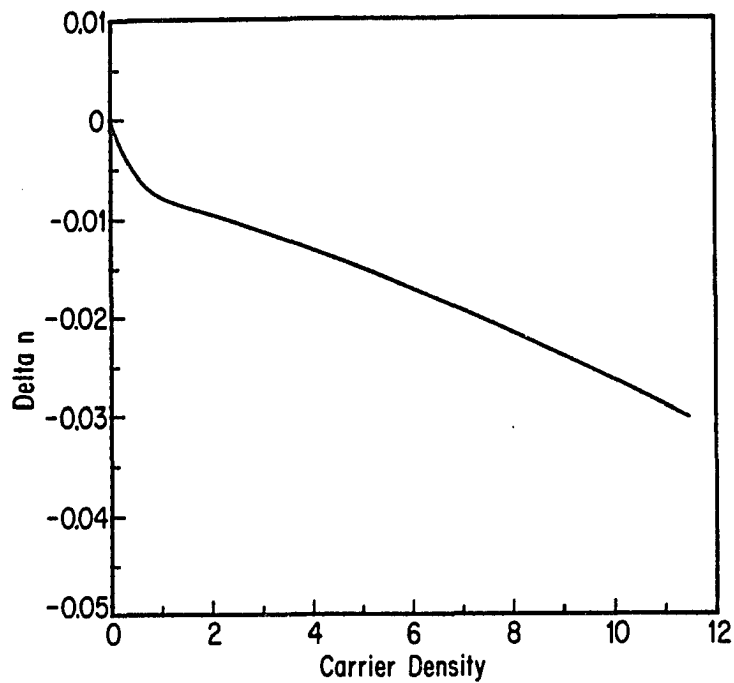


Figure 8. Calculated change in GaAs index of refraction  $n$  as a function of carrier density  $N$  ( $\times 10^{17} \text{ cm}^{-3}$ ) at  $-4 E_R$  below the band edge (885).

Some earlier work has been done on optimizing nonlinear etalons (Miller [1981]) using a purely dispersive model. In that study it was possible to analytically solve for optimum parameters. In the case of the combined dispersive and absorptive model of this study, it is not possible to treat the problem analytically and numerical methods must be used. In order to try many values of a chosen parameter, the devices were modeled in steady-state. This involves setting the derivative in equation (3) to zero and solving the system of equations for a sequence of carrier densities. A critical parameter in operating the semiconductor etalons is the initial resonance frequency of the etalon. This frequency is determined by the optical thickness of the etalon as described earlier. The GaAs etalon was modeled in steady-state operation for a large range of optical thicknesses in order to determine if there was an optimum initial detuning for the devices. The detuning of the etalon from the laser frequency is calculated from the optical thickness of the etalon. Figure 9 illustrates the results of such a calculation. The two curves superimposed in Figure 9 are points taken from the steady-state bistability curve as illustrated in Figure 10 for each increment of optical thickness. The upper curve in Figure 9 is the incident intensity required for switch-up measured at point A in Figure 10. The lower curve is the transmitted energy after switch-up as measured at point B in Figure 10. One can see for the series of widely separated scans in etalon thickness in Figure 9 that there is a definite maximum-transmission detuning for the etalon. The detuning for maximum transmission is unfortunately not the same as for lowest power operation. This means that any system design utilizing the transmitted intensity of the etalons must consider the best compromise for those two desirable attributes. The slow rise in switch-up intensity with etalon thickness is attributable to the

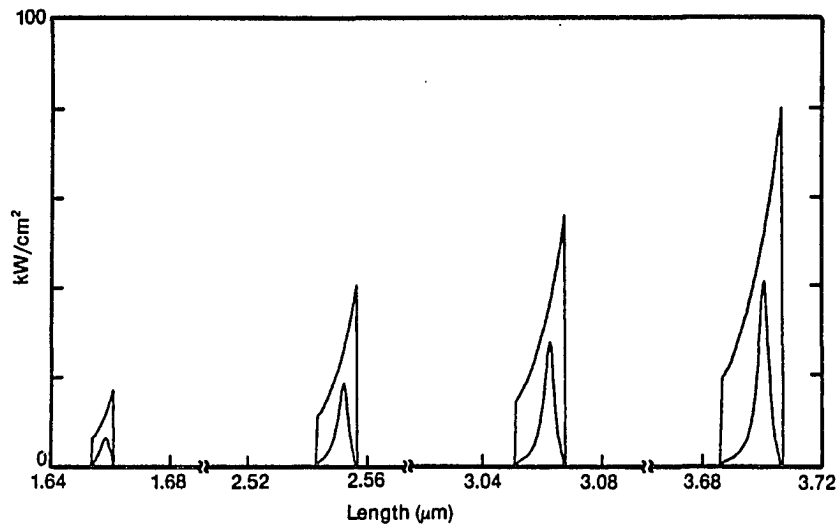


Figure 9. Calculated switch-up intensity (upper plot) and transmitted intensity after switch-up (lower plot) as a function of GaAs thickness (which determines the resonant wavelength of the etalon). A few widely separated thicknesses are shown.

change in etalon finesse with thickness. The etalons are assumed completely filled with GaAs, and the excitation frequency is kept constant in this calculation. The thicker etalon has a broader transmission peak that has to be shifted further to obtain bistability, and therefore requires higher intensity. The free-spectral range also changes with the etalon thickness, so that the separation between adjacent Fabry-Perot transmission peaks, and consequently the separation between adjacent thickness ranges that show bistable operation, gets smaller with increasing etalon thickness. The curves plotted in Figure 9 are not for adjacent, but for several widely separated resonances.

The bistable operation of GaAs etalons was also modeled in a time-dependent study. The hysteresis loops typically used to illustrate bistable operation are obtained by using an input pulse with a triangular intensity dependence on time.

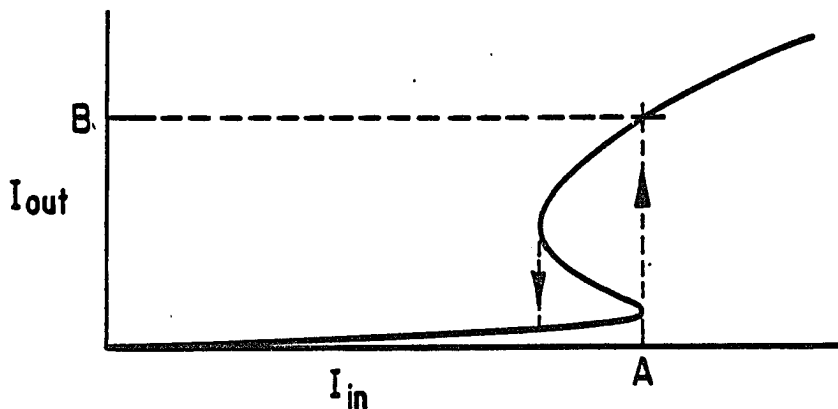


Figure 10. Input intensity versus output intensity for a steady-state simulation of a nonlinear etalon. The arrows indicate switch-up and switch-down for the dynamic response. Point A is the input intensity at switch-up and point B is the output intensity after switch-up.

Since the time for the light in the etalon to decay away is much shorter than the carrier lifetime in the material, the effective time constant for the devices is the carrier lifetime. For GaAs devices that have not had some special modification to reduce the carrier lifetime, the lifetimes are typically a few tens of nanoseconds. For these calculations, the carrier lifetime was assumed to be 10 ns. The results can be applied to other carrier lifetimes by scaling the pulse widths, since the ratio of the pulse width to the carrier lifetime is the important parameter in the calculation. The dynamic calculations were performed for a variety of different device parameters. A listing of the program used for the bistable loop calculations is given in appendix A. Figure 11 shows plots for dynamic simulations performed at several different detunings and pulse lengths. The plots in Figure 11d show the corresponding steady-state curves. The high transmission operating regime is

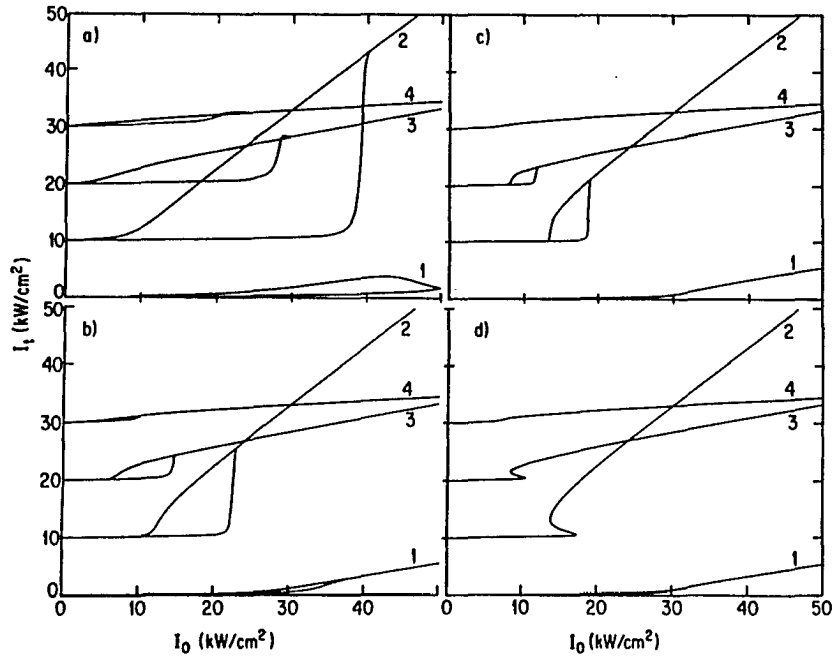


Figure 11. Transmitted intensity versus input intensity computed for a  $2\text{-}\mu\text{m}$  thick etalon at room temperature for the excitation energy  $\hbar\omega = 1.4032\text{ eV}$ , well below the exciton resonance at  $1.420\text{ eV}$ . Figs. 11a - 11c are obtained assuming pulsed excitation with a triangular pulse of full width  $10\tau$  (a),  $100\tau$  (b), and  $1000\tau$  (c). Fig. 11d shows the steady-state results. The different curves 1 - 4 in each figure are for the detunings  $\Delta\hbar\omega = \hbar\omega_R - \hbar\omega = -0.0170\text{ eV}$ ,  $-0.0142\text{ eV}$ ,  $-0.0115\text{ eV}$ , and  $-0.008\text{ eV}$ , respectively.  $\hbar\omega_R$  is the resonator eigenfrequency, and the mirror reflectivity  $R = 0.9$ . The baseline for the transmitted intensity in curves 2, 3, and 4 has been shifted by 10, 20, and 30  $\text{kW}/\text{cm}^2$ , respectively.

clearly present in the dynamic simulations as well. The predicted high transmission operation is due to a combination of the dispersive and absorptive properties of GaAs. In this case, the detuning of the etalon is initially far enough

away from the excitation frequency that the intensity in the cavity has built up to the point that the absorption is saturated by the time the device has dispersively tuned through resonance. Figures 11a, b and c illustrate the effect of different pulse lengths of the same intensity. Since the total change in carrier density in the material is related to the total energy in the light pulse, it is clear that switching intensities are higher for the shorter pulses.

The reflected signal from the front face of the semiconductor etalon has not been discussed. It can also show a bistable response to the input light intensity. Figure 10 shows a bistable loop in reflection for the same conditions as the transmitted loop number 2 in Figure 11b above. From Figure 12 it is apparent

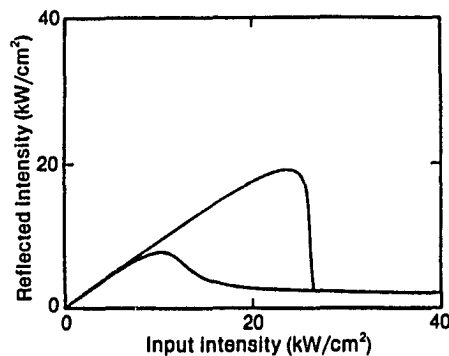


Figure 12. Reflected intensity versus input intensity for the same conditions as in Figure 11b (2).

that the reflected signal is a negating function. For low intensities, the reflectivity of the etalon is very high. If the switching threshold is passed, the device becomes highly transmitting and the reflected signal goes low. The device could function as a NOR or NAND gate, depending on the bias and signal levels used.

Although a systematic study comparing the results of the model with experimental measurements has not been performed, some comparisons with

previous experiments (Jewell [1984] and Sahlen, Olin, Masseboeuf, Lundgren and Rask [1987]) have shown good agreement for the predicted switching power and detuning. Quantitative predictions of the model should be considered with caution, since the theory is based on a plane-wave model and experiments are usually performed with Gaussian beams. The qualitative predictions of the model are what are most important for determining the optimum operating parameters and the feasibility of some applications of the etalons. Figure 13 is a series of photographs taken from an oscilloscope showing the change in shape of a bistable hysteresis loop for an etalon of 2  $\mu\text{m}$ -thick GaAs with approximately 90% mirrors. The etalon detuning from Figure 13a to 13c is to lower energy, further from the laser detuning. The detuning was varied by moving the focussed light spot location on the slightly wedged etalon. The trend toward higher-contrast operation is evident and in qualitative agreement with the predictions illustrated in Figure 9. There was insufficient power available during the experiment to saturate the absorption completely. The model includes only one absorption mechanism: direct, one-photon transitions, and does not include any unsaturable absorption mechanisms. As the intracavity intensity increases, two-photon absorption may become important. Two-photon absorption would be, effectively, an unsaturable absorption mechanism.

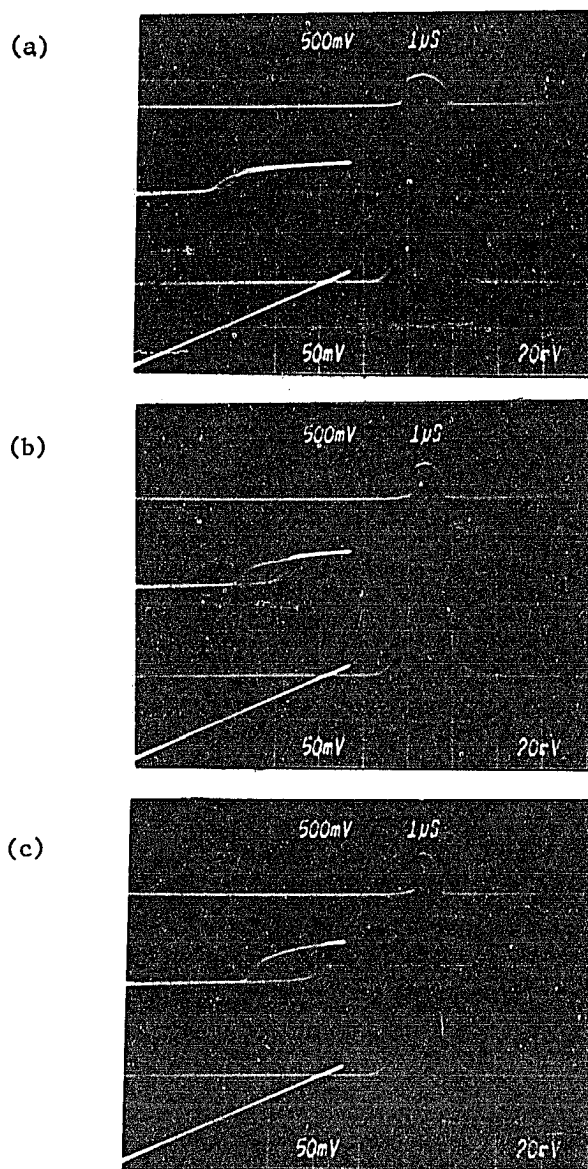


Figure 13. A series of experimental bistable loops for a 2- $\mu\text{m}$  bulk GaAs etalon with 90% mirrors. The etalon detuning is further (to longer wavelength) from the excitation wavelength (885 nm) from a to c.

## Modeling of optical logic devices

There are certain logic operations that are possible with a bistable device. Since the device will maintain one of two discrete output states for some range of input intensity, it is possible to use the device in a latched mode. In that case, the device would be biased by a holding beam that has an intensity positioned between the switch points on the bistable loop. The switching pulse that actually is the input logic pulse (or pulses) then only has to be sufficiently large for the total incident intensity to exceed (for a sufficient time) the switch-up threshold (see Figure 6). The device, once switched, would remain in a high-transmission state until the device is turned off by interruption of its bias power or some other mechanism. One advantage of the latched operation is the ability to hold the logic output state for a long time, in order to simplify the problem of synchronizing the gates with the arriving light pulses. By "clocking" the bias onto the devices it is possible to control and synchronize bistable devices even when their response time is much slower than the propagation time of the signals between gates. (Smith, Walker, Tooley and Wherrett [1987]) Another advantage of the latched operation is the ease of achieving differential gain. The nonlinear etalons are operated as passive devices without producing gain, relative to the *total* incident power onto the devices. It is possible to achieve differential gain, in which the device is able to transmit (or reflect) a larger signal than the *switching* pulse when used as a latched device. Part of the output energy comes from the transmitted portion of the bias. In this case the bias energy is treated as a power supply for each device and only the switching pulse need come from the previous devices in cascaded operation.

In the bistable or latched operation, the ability of the device to be held in the high state after switching makes it possible to control the length of the transmitted pulse by the length of time the bias is held. This allows the restoration of the full switching pulse in time, without losing energy during the time the device is switching on or off and the device is not at the full high state.

The use of bistable devices as latched logic elements was simulated as shown in Figure 14. The device modeled is operating as an AND gate with the switching pulse being two superimposed logic "high" input pulses. In the plots shown, the switching pulse (Figure 14a ) was deliberately made a short, high intensity pulse compared to a much longer bias pulse in order to have good time resolution in studying the switching dynamics and to more easily illustrate the differences in the roles of the bias and switching pulses. In practical application, the transmitted pulse after switch-on would need to be identical to the switching pulse, with some gain. There is a practical limitation on how much differential gain one can obtain from a bistable device. This is illustrated in Figure 14b which shows that as the switching pulse gets closer to the minimum steady-state switching threshold, the response of the system slows down and the switching of the device is delayed. This is a well-known property of first-order phase transitions such as optical bistability, and is commonly called critical slowing down (Ma [1976]). In order to get larger values of differential gain in the devices, it is necessary to set the bias closer to the switch-on point on the bistable curve and use the smallest switching pulse possible. The time response of the device is then slowed by the effects of critical slowing down. Consequently, for latched operation of bistable devices, there is another compromise necessary between the two desirable features of speed and high gain.

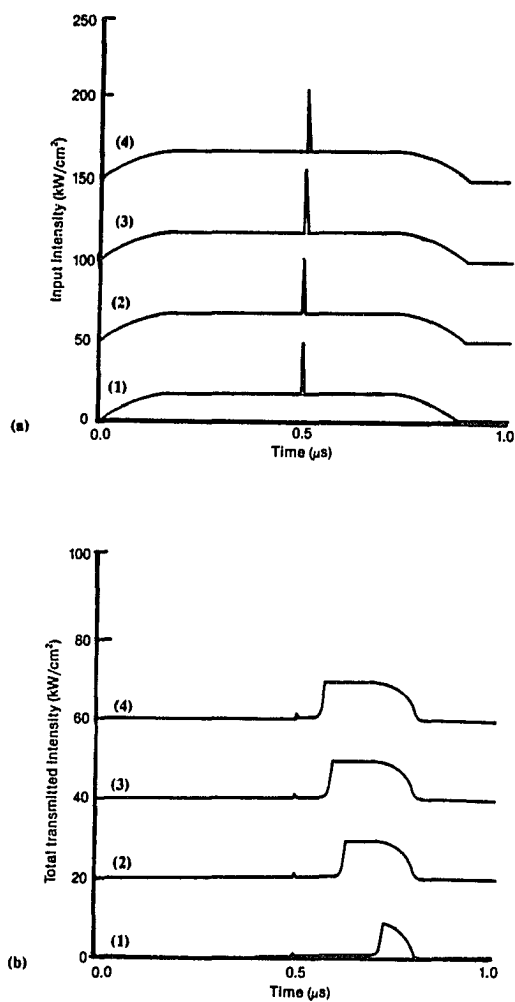


Figure 14. Latched AND gate modeled for a GaAs etalon. The input pulses (a) consist of a short switching pulse and a longer bias pulse. The device parameters are the same as for Fig. 11 (2). The switching pulses are increasing by  $2 \text{ kW}/\text{cm}^2$  in intensity from curve 1 to curve 4. The transmitted pulses (b) show increasing delay for the smaller switching pulses. The baselines for curves 2,3, and 4 have been shifted by 10,20, and  $30 \text{ kW}/\text{cm}^2$ , respectively.

Timing skew due to unequal propagation times of signals, and jitter due to random variations in device response are both problems of concern in fast electronic systems. It is often claimed that optical systems would be free of these problems. This is not entirely true, although timing problems should be more manageable. The linear optical elements used in an optical system can be made free of skew by provision of equal optical paths for signals through the system. For lenses this is an inherent property, but holographic elements, beamsplitters and prisms will require careful compensation for the optical path differences these devices would produce.

The nonlinear devices can be expected to have variations in their response times in a system. The effects of jitter in the input signal arrival times are illustrated in Figures 15, 16, and 17. The single large input pulse is the superposition of two coincident pulses which are delayed in the other plots. If the design and operating parameters of a semiconductor device are specified, the systems tolerances necessary for their application can be studied with such computer simulations.

It is evident from the earlier discussion that the actual complete switching time of a latched bistable logic gate must be longer than its nonlinear response time. The switch-up time of a GaAs etalon has been measured to be on the order of one picosecond (Migus et al [1985]). The switch-off times of the devices are however much slower. The switch-off time is determined by the carrier lifetime in the device. This gives a switch-off of a few tens of nanoseconds in typical devices tested to date. It is possible to use several tricks to reduce the carrier lifetime in the devices by increasing the rate of carrier recombination. Fabricating the GaAs layer without any passivating cover layer of AlGaAs to

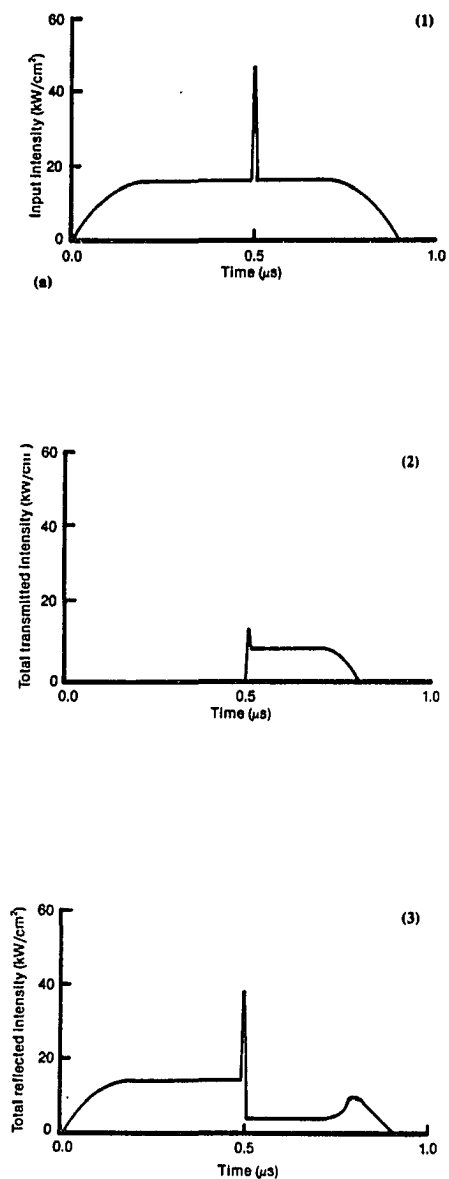


Figure 15. Modeling of pulse-timing effects for AND gate operation. Plots 1, 2, and 3 are of input pulses, transmitted intensity and reflected intensity, respectively. In this series, the switching pulses are coincident.

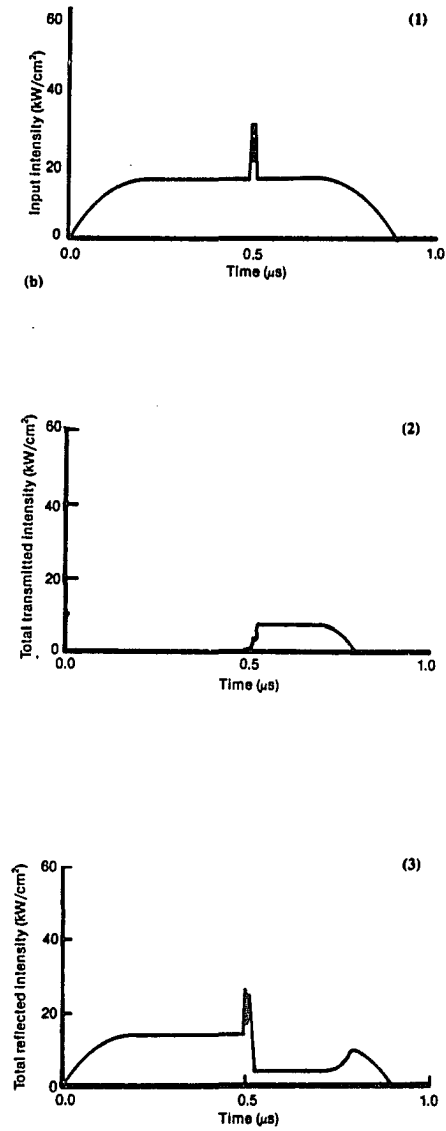


Figure 16. Modeling of pulse-timing effects for AND gate operation. Plots 1, 2, and 3 are of input pulses, transmitted intensity and reflected intensity, respectively. In this series, one pulse suffers a delay of 10 ns.

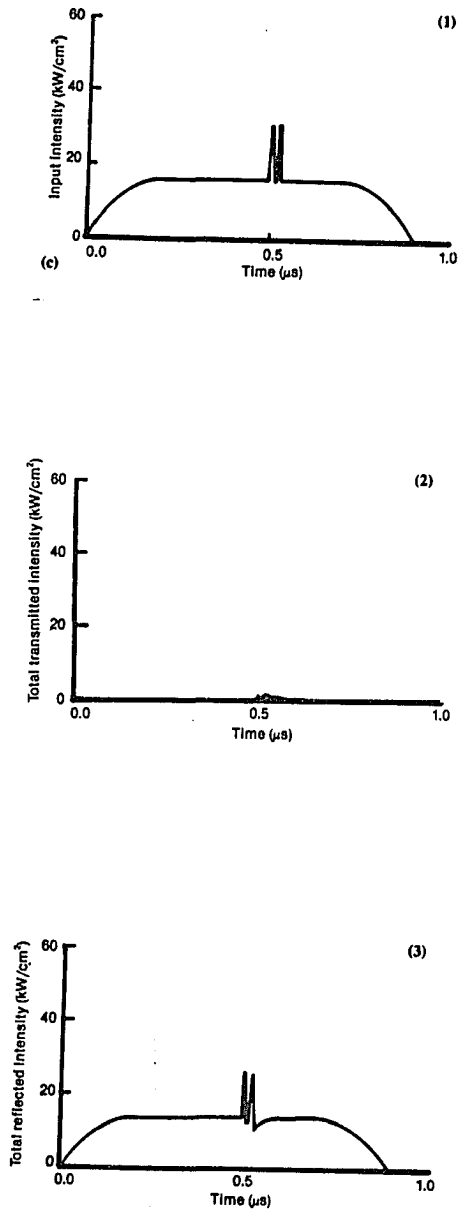


Figure 17. Modeling of pulse-timing effects for AND gate operation. Plots 1, 2, and 3 are of input pulses, transmitted intensity and reflected intensity, respectively. In this series, one pulse suffers a delay of 20 ns.

increase surface recombination (Lee et al [1986]), etching microscopic structures into the GaAs to further increase surface recombination (Lee et al [1986]) or damaging the semiconductor to produce recombination sites (Silberberg et al [1985] and Lee et al [1986]) have all been successful approaches. Device relaxation times of around 100 picoseconds have been demonstrated. There is however, an intrinsic drawback to this idea for latched bistable devices. Reducing the carrier lifetime in the material greatly increases the intensity necessary to create the carriers that make the device switch, when the light pulse is longer than the material response time. (See equation (3).)

A considered alternative approach to etalon logic is to operate the devices in a transient regime where the devices are not latched and bistable operation is not even necessary. In this case, one is just operating the device on the switch-up side of its hysteresis curve which functions as a threshold. The switch-down response of the device is still determined by the carrier lifetime, but the much shorter light pulse can be well on its way by then. The operating frequency of the individual device is still determined by its relaxation time (disregarding thermal limitations). Since the light pulses used for transient operation can be much shorter than the carrier lifetime in the material, the techniques mentioned earlier for reducing the carrier lifetime may be applied. The short pulses require high intensities to achieve the needed pulse energies, but such pulses are readily created with several types of laser systems. A major concern with transient operation is whether or not it is possible to achieve useful differential gain and restorable logic operation. In transient operation, the bias pulse is used to bring the device close to the switching threshold, and the nearly coincident switching pulse must be sufficient to push the device over the threshold. In order to obtain

differential gain, the etalon must transmit enough of the bias pulse to more than compensate for the loss of the transmitted switching pulse. To achieve restoration of the switching pulse, the bias pulse must be longer than the switching pulse so that the narrowing of the switching pulse is compensated for.

To study the feasibility of obtaining differential energy gain in transient operation, we have assumed two-pulse excitation as described above. For the 2- $\mu\text{m}$ -thick etalons assumed, the cavity round-trip time is approximately 30 femtoseconds. This is much less than both the excitation pulse length and the material relaxation time, so the assumptions of equation (1) are still valid. The differential energy gain is then obtained as the total transmitted energy (bias and switch pulses present) minus the transmitted energy in the presence of the bias pulse only, both divided by the switch-pulse energy. A listing of the program for the transient calculations is given in appendix B. Examples of the results for Gaussian-shaped pulses are plotted in Figure 18. The different curves show that as the length of the pulses is shortened, the differential energy gain is seen to decrease. Calculations have been made for different bias intensities and other ranges of switch-pulse intensity. Further simulations used switching pulses much less than the carrier lifetime (one picosecond FWHM) and longer bias pulses to investigate the possibility of increasing the gain by delaying or advancing the arrival of the short switching pulse relative to the bias pulse. The effects were negligible. The conclusion is that passive nonlinear etalon devices cannot exhibit useful differential energy gain for operating pulses shorter than about  $10\tau$ . In short pulse operation, the carrier excitation integrates over the indistinguishable incident light pulses. The Fabry-Perot peak position shifts with the integrated pulse energy and does not show a sharp enough threshold in transmission to

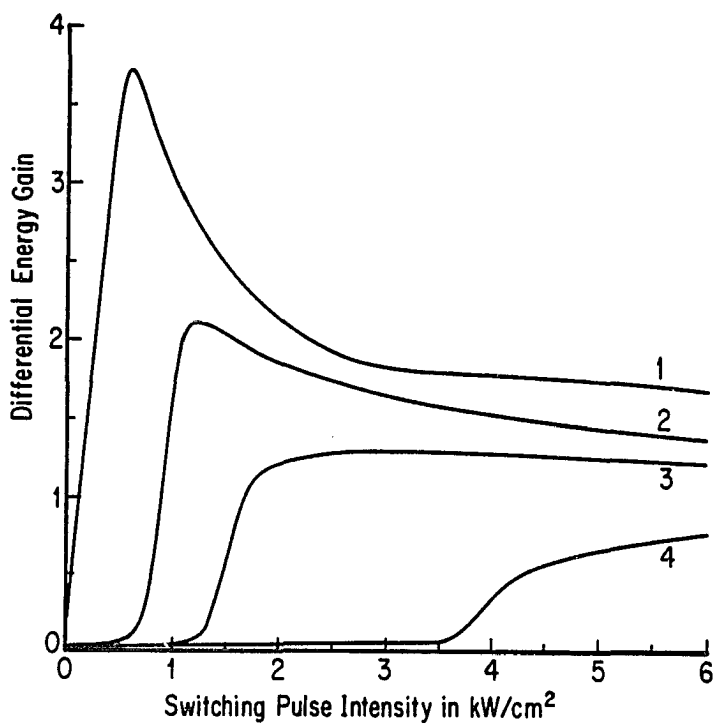


Figure 18. Differential energy gain versus switch-pulse intensity for different ratios of temporal pulse width to carrier relaxation time  $\tau$ . The parameters are those of Fig. 11 (2), and the peak intensity of the bias pulse was kept at  $17.1 \text{ kW/cm}^2$ , i.e., just below the steady state switch-up value. Curves 1, 2, 3, and 4 are for Gaussian pulses with FWHM pulse widths of  $100\tau$ ,  $50\tau$ ,  $25\tau$ , and  $10\tau$ , respectively.

achieve appreciable differential gain. In order to achieve single-wavelength, cascaded optical logic gates that can operate with picosecond pulses it will be necessary to dramatically reduce the carrier lifetimes in the semiconductor material.

The discussion so far has assumed that all of the incident light on an optical logic device is of the same frequency. In consequence, it is not possible to tell which part of the output signal came from the bias or from the switching beams. Nonlinear semiconductor etalons have been operated as all-optical switching devices with two different light wavelengths (Jewell et al [1985]). One wavelength is chosen for high absorption inside the band edge of the semiconductor, where carriers will be generated very efficiently. Both the bias and switching (input signal) beams are at this wavelength. The other wavelength is below the band edge in energy, and very little absorption occurs. This light acts as a probe of the state of the etalon. It does not significantly affect the state of the device itself, and can be of high or low intensity.

The advantages of this kind of operation are that it is very efficient in its use of bias and switching energy and the etalon can have different properties for the two different wavelengths of light. The two different wavelengths are absorbed to different degrees in the etalon, and the mirrors can have different reflectivities for the two wavelengths. For the highly absorbed wavelength, the mirror reflectivity should be lower to match the absorption losses and allow efficient coupling of the switching and bias beams into the etalon even when the Fabry-Perot peak is shifting. For the longer wavelength, the absorption is very low, and high contrast in the transmitted signal is desirable. By using higher reflectivity mirrors, the etalon can have a very high finesse and the resulting

sharp Fabry-Perot peaks give high contrast in the output signal. A two-wavelength device can be used in either latched or transient operation. Since the probe beam does not provide the switching energy and is not highly absorbed, achieving differential gain and restoration of the input signal in transient operation is possible. The major difficulty with the two-wavelength operation is obviously that the output signal is not the same wavelength as the input signal. This is a more serious problem than just requiring more than one light source. Since the output beam is the longer wavelength, it is not an efficient switching energy source for a later device. It is possible to switch a device using the longer wavelength as the switching pulse and the shorter wavelength as the probe (Jewell [1984]), however the power requirements and output contrast are so different that restorable logic operation is not practical. In principle, it should be possible to cascade such devices in a limited way by using a material with an absorption-edge that is shifted further to longer wavelength for each device, each device requiring another light source. For any useful application of two-wavelength operation to restorable logic systems, it must be possible to use either of the two wavelengths to switch the device with similar performance. A material with a sharp, isolated absorption feature that can be readily saturated by light of slightly higher or lower energy is needed.

### Waveguide design

So far, this discussion has been concerned with the physical operating principles of nonlinear etalon devices. There are actually two forms of the devices that are considered for application. One can easily visualize two-dimensional arrays of thin etalons that would be addressed by holographic optical elements. The major advantage of such a scheme is the ability to take advantage of the natural parallelism of optics. Even moderately fast devices could use massive parallelism to have enormous computational throughput. The discussion so far has been of this kind of device, with a thickness of a few microns. Another form is a waveguide etalon in which the end faces of the etalon are mirrors just like in the etalon array, but the etalon is a waveguide hundreds of microns thick. In this case the waveguide structure provides transverse confinement of the light, which would otherwise be lost by diffraction in an etalon of such length and of small cross section. Therefore, the use of waveguide structures allows longer interaction lengths for the light propagating in the material. In principle, one can still get a large phase shift in a nonlinear waveguide with a very small change in the material index of refraction. The other side of the argument is that because of long interaction length, the light source must be detuned far from the band edge to have acceptable losses, and consequently only small index changes are possible anyway.

A possible advantage of waveguides is that they have small cross sections in which diffraction is not a problem. This could allow a smaller total energy requirement for switching. Etalon devices can be made into waveguides by etching very small posts into the sample that can provide similar confinement

over shorter distances (Jewell, Scherer, McCall, Gossard and English [1987]). Waveguides are also interesting because of the ease with which they can be integrated into monolithic structures. With GaAs-based technology, it is entirely conceivable to have a waveguide switching device on the same chip as laser sources and detector/amplifier circuits. In practice, the fabrication and input coupling of a waveguide etalon device on such a chip would pose some problems, due to the need for end-facets and their reflectivity. Balanced against these considerations are a couple of problems not yet mentioned with waveguides. The parallelism inherent in free-space optical systems is defeated and there are substantial coupling losses in III-V waveguide devices, particularly when the end faces must be fairly reflective. Another loss mechanism of importance in waveguides is scattering from roughness and defects in the waveguide interfaces and surfaces and from internal material defects.

Waveguides function by the light inside the higher index medium reflecting from the lower index medium. For a given guide structure, there may be some angles of incidence on the cladding layers for which the light is totally reflected for both cladding layers. The angles that fulfill this condition, and the resonance condition that the total phase difference for two reflections ( a full round-trip across the guide layer ) be  $2\pi$ , define the modes that are allowed to propagate in the waveguide without radiative losses (ideally) (Kogelnik [1985]). Light rays coupled into the waveguide that do not have the right internal angle of incidence will be rapidly attenuated by transmission into the cladding layer. It is possible to carry this geometrical ray-optics picture to a very sophisticated level, but it becomes clumsy and unworkable.

A more general approach is to solve the electromagnetic wave equation for the specific boundary conditions imposed by the waveguide structures. We can start with the simplified Maxwell equations for an optically isotropic medium without magnetization,

$$\nabla \cdot \mathbf{E} = 0 \quad (5)$$

$$\nabla \times \mathbf{H} = \epsilon_0 n^2 \frac{\partial \mathbf{E}}{\partial t} \quad (6)$$

$$\nabla \cdot \mathbf{H} = 0 \quad (7)$$

$$\nabla \times \mathbf{E} = -\mu_0 \frac{\partial \mathbf{H}}{\partial t} \quad (8)$$

The wave equations can then be obtained:

$$\nabla^2 \mathbf{E} = \mu_0 \epsilon_0 n^2 \frac{\partial^2 \mathbf{E}}{\partial t^2}$$

and

$$\nabla^2 \mathbf{H} = \mu_0 \epsilon_0 n^2 \frac{\partial^2 \mathbf{H}}{\partial t^2}.$$

If we consider a dielectric slab waveguide with the geometry shown in Figure 19, in which the structure is homogeneous in the  $z$  direction and the requirement that the wave is propagating along  $z$  with a constant phase velocity, the electromagnetic waves can be written in the form

$$E(x,y,z,t) = E(x,y)\exp[i(\omega t - \beta z)]$$

$$H(x,y,z,t) = H(x,y)\exp[i(\omega t - \beta z)]$$

where  $\omega$  is the angular frequency and  $\beta$  is the propagation constant in the  $z$

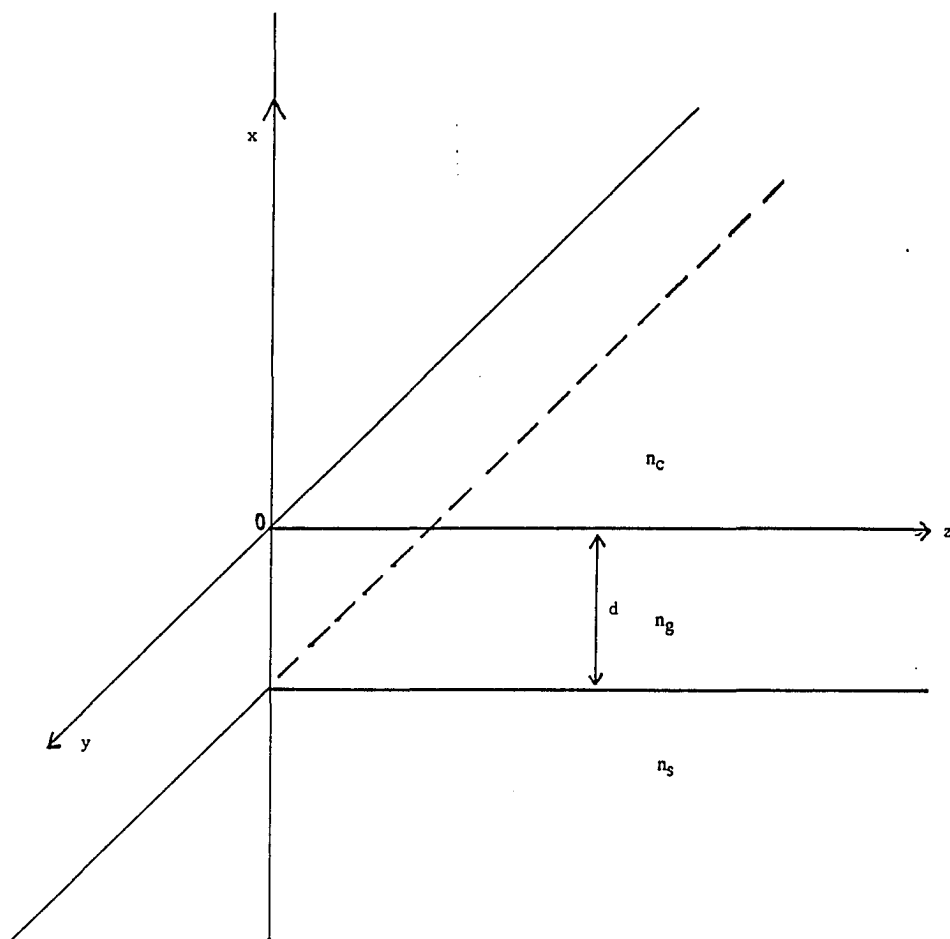


Figure 19. Three-layer slab waveguide geometry.

direction. The wave equations can then be separated into transverse and

longitudinal components

$$\{\nabla_t^2 + [n^2(x,y)k_0^2 - \beta^2]\}E(x,y) = 0$$

$$\{\nabla_t^2 + [n^2(x,y)k_0^2 - \beta^2]\}H(x,y) = 0$$

where  $\nabla_t^2 = \nabla^2 - \mathbf{e}_z \frac{\partial^2}{\partial z^2}$  where  $\mathbf{e}_z$  is the unit vector in the z direction and  $c^2 = 1/\mu_0\epsilon_0$ .  $k_0$  is the propagation constant for the field in vacuum, related to the angular frequency by  $k_0 = \omega/c$ . The effective index for the waveguide can be defined as  $N = \beta/k_0$ .

The boundary conditions that apply in the absence of surface charge or current are

$$E_{2t} = E_{1t}$$

$$H_{2t} = H_{1t}$$

for an interface between two media, labelled 1 and 2. The subscript t refers to the tangential component. For negligible magnetization and assuming for the moment, a linear medium, we also have:

$$n_2 E_{2n} = n_1 E_{1n}$$

and

$$H_{2n} = H_{1n}$$

where the coefficients  $n$  are the refractive indices and the subscripts  $n$  refer to the normal component.

The slab waveguide geometry in Figure 19 is an asymmetric structure with a guiding region of thickness  $d$  with an index  $n_g$ . The cladding and substrate layers are assumed to be infinitely thick and of indices  $n_c$  and  $n_s$ . From the earlier geometrical optics arguments  $n_g > n_c$  and  $n_s$ .

Due to the different boundary conditions, it is common to consider the modes in the waveguide to have two different linear polarizations. One is the E field parallel to the waveguide layers (TE or transverse electric) and the other is with the E field perpendicular to the layers (TM or transverse magnetic).

For the TE case, the transverse wave equation can be written,

$$\left\{ \frac{\partial^2}{\partial x^2} + [n_q^2 k_0^2 - \beta^2] \right\} E_y = 0 \quad (9)$$

where  $q = g, c$  or  $s$ .

The fields for a guided mode are required to vanish at infinity. Applying that principle and the boundary condition at  $x = 0$  and  $x = -d$ , the solutions for equation (9) can be written

$$E_y = \left\{ \begin{array}{ll} Ae^{-\gamma_c x} & x \geq 0 \\ A\cos(\kappa x) + B\sin(\kappa x) & 0 \geq x \geq -d \\ [A\cos(\kappa d) - B\sin(\kappa d)]e^{\gamma_s(x+d)} & x < -d \end{array} \right\}$$

where  $\kappa^2 = (n_g^2 k_0^2 - \beta^2)$ ,  $\gamma_c^2 = (\beta^2 - n_c^2 k_0^2)$  and  $\gamma_s^2 = (\beta^2 - n_s^2 k_0^2)$ . The solutions are similar to those for a quantum-mechanical particle in a potential well, with oscillatory solutions in the well and exponentially decaying ones outside the well. The magnetic and electrical fields are related through equations (6) and (8). It can be shown that

$$H_x = -\frac{\beta}{\omega\mu_0} E_y$$

and

$$H_z = -\frac{i}{\omega\mu_0} \frac{\partial E_y}{\partial x}$$

Since  $H_z$  is continuous across the interface, the derivatives of the previous solutions for  $E_y$  must be continuous. The following relations can be solved for:

$$B = -\frac{\gamma_c}{\kappa} A$$

$$\tan(kd) = \frac{\kappa(\gamma_s + \gamma_c)}{\kappa^2 - \gamma_s \gamma_c} \quad (10)$$

The last equation is a form of the waveguide dispersion equation. Through the defining relations for  $\kappa$ ,  $\gamma_s$  and  $\gamma_c$  it defines the allowed values of  $\beta$  in terms of the layer indices, layer thicknesses and light frequency. Since the equation can have multiple roots, there can be multiple guided modes that are allowed. The allowed modes are numbered from the zero-order mode up. If either  $\gamma_c$  or  $\gamma_s$  is

zero-valued or imaginary for a given mode, the field is not decaying outside the guiding region, and that mode is said to be above cutoff, as well as all higher-order modes. It is possible in an asymmetric slab waveguide, with TE polarization, to have no modes above cutoff. For TM polarization there is always at least one allowed mode, and a symmetric guide structure will always have at least one for either polarization. A single-mode waveguide is one which has been designed so that only the lowest-order mode is below cutoff.

For TM polarization, the wave equation is written

$$\left\{ \frac{\partial^2}{\partial x^2} + [n_q^2 k_0^2 - \beta^2] \right\} H_y = 0$$

where  $q = g, c$  or  $s$ . A similar application of the boundary conditions gives the solutions:

$$H_y = \begin{cases} Ce^{-\gamma_c x} & x \geq 0 \\ C \cos(\kappa x) + D \sin(\kappa x) & 0 \geq x \geq -d \\ [C \cos(\kappa d) - D \sin(\kappa d)] e^{\gamma_s (x+d)} & x < -d \end{cases}$$

where  $\kappa^2 = (n_g^2 k_0^2 - \beta^2)$ ,  $\gamma_s^2 = (\beta^2 - n_s^2 k_0^2)$ ,  $\gamma_c^2 = (\beta^2 - n_c^2 k_0^2)$  and

$$D = -\frac{n_g^2 \gamma_c}{(n_c^2 \kappa) C}$$

$$\tan(kd) = n_g \frac{2\kappa(n_c^2 \gamma_s + n_s^2 \gamma_c)}{n_s^2 n_c^2 - n_g^4 \gamma_s \gamma_c} \quad (11)$$

The preceding analysis is only for a slab waveguide that has confinement in one-dimension only. For nonlinear devices based on semiconductor waveguides, the diffraction losses in the unconfined direction could greatly increase the power requirements. Consequently, it is necessary to design and fabricate waveguides that have confinement in the transverse direction as well. There are a variety of schemes available for doing this. Kogelnik's review describes a few of them. The two most practical for semiconductor fabrication by the facilities available to us were the ridge waveguide (Goell [1973] and Somekh, Garmire, Yariv, Garvin and Hunsperger [1974]) and the strip-loaded waveguide (Furuta, Noda and Ihaya

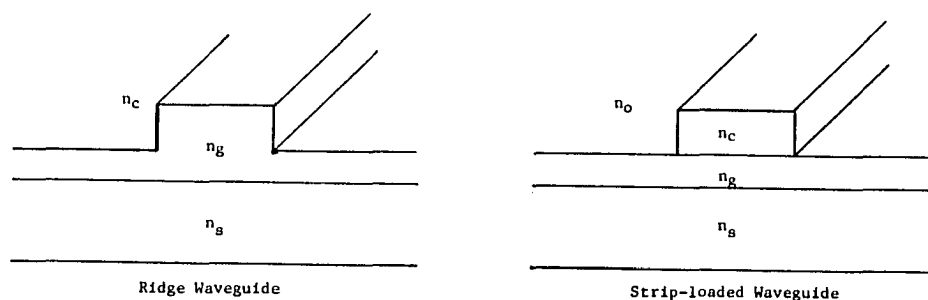


Figure 20. Illustration of ridge waveguide and strip loaded waveguide structures for transverse confinement of light. Guiding region is in layer of index  $n_g$ .

[1974] and Ramaswamy [1974]). The two types are illustrated in Figure 20. The advantages of these two structures include the ease with which they may be fabricated by photolithography and etching, and the fact that the light is confined

in the region below the etched structure, so that the surface roughness from etching has less effect than in a rib or strip waveguide that is formed by completely etching to the substrate layer.

Although some ridge waveguides were fabricated and used in experiments as described in the experimental results, they were multimode devices that were fabricated from samples that were designed for other purposes. That experience convinced us that it was necessary to design single-mode waveguides. Strip-loaded waveguides were used in subsequent experiments and their design will be explained. The design of ridge waveguides is very similar and is well summarized in Kogelnik and in more detail in Gibbons [1987]. The strip-loaded structure was investigated by Ramaswamy, who not only analyzed it by the effective index method, but also checked the theory by fabricating and testing real waveguides of sputtered glass.

As depicted in Figure 21, the strip-loaded structure can be separated in the transverse ( $y$ ) direction into three regions. Each of these has a  $\beta$  and an effective index  $N$ , for each mode that can propagate in the slab in that region. The three regions can be considered a symmetrical slab waveguide as depicted in Figure 19. The calculation of the allowed modes in the  $y$  dimension is then a straightforward application of the asymmetric-slab-waveguide treatment presented earlier. The slab waveguide structure in each region is not three layers, but four, two of which are semi-infinite. Ramaswamy has solved the boundary-value problem for the TE polarization. Solutions for both the TE and TM polarization case are shown here. The derivation of the solutions is an extension of the method for the three-layer slab waveguide described earlier. The four-layer slab geometry is illustrated in Figure 22.

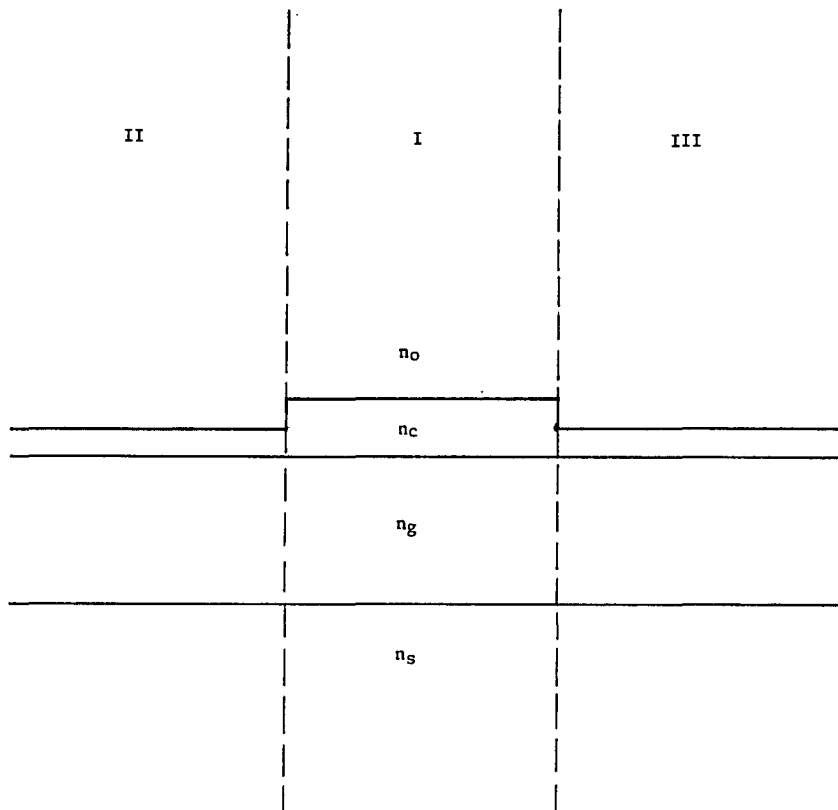


Figure 21. Division of strip-loaded waveguide structure into three regions of different effective index for light in the guiding layer.

For TE polarization, the solutions for the wave equation are:

$$E_y = \left\{ \begin{array}{ll} Ae^{-\gamma_o(x-t)} & x \geq t \\ Be^{\gamma_c x} + Ce^{-\gamma_c x} & t \geq x \geq 0 \\ D\cos(\kappa x) + E\sin(\kappa x) & 0 \geq x \geq -d \\ [D\cos(\kappa d) - E\sin(\kappa d)]e^{\gamma_s(x+d)} & x < -d \end{array} \right\}$$

An additional set of solutions for  $H_z$  can be obtained as in the three-layer case. Simultaneous solution of the coupled set of equations yields several equations relating the various amplitude coefficients and the following waveguide dispersion equation:

$$\tan(\kappa d) = \tan^{-1} \left\{ \frac{\gamma_s}{\kappa} \right\} + \tan^{-1} \left\{ \frac{\gamma_c(1-\eta e^{-2\gamma_c t})}{\kappa(1+\eta e^{-2\gamma_c t})} \right\} + m\pi$$

where  $\eta = \frac{\gamma_c - \gamma_0}{\gamma_c + \gamma_0}$ .

Similarly, for TM polarization the dispersion equation can be derived:

$$\tan(\kappa d) = \tan^{-1} \left\{ \frac{\gamma_s n_g^2}{\kappa n_s^2} \right\} + \tan^{-1} \left\{ \frac{\gamma_c n_g^2(1-\eta e^{-2\gamma_c t})}{\kappa n_c^2(1 + \eta e^{-2\gamma_c t})} \right\} + m\pi.$$

The definitions of  $\kappa, \gamma_c$  and  $\gamma_s$  are the same as earlier and  $\gamma_0^2 = (\beta^2 - n_0^2 k_0^2)$ .

In practice, the design for the strip-loaded guide structure is arrived at by guessing a trial structure for the waveguide, including layer indices and thicknesses and an etched depth and width for the strip, and calculating the waveguiding properties of the structure. For strip-loaded guides, the layer structure is a four-layer slab waveguide. Equations (12) and (13) can be solved for the propagation constant  $\beta$ , and for the number of allowed modes in the direction perpendicular to the layers. When a structure is found that is single-mode in the vertical dimension, the effective indices can be calculated for the two different regions in figure 21, using the etch depth selected. The effective indices

are then used in equations (10) and (11), which are solved for the number of transverse guided modes in the structure for a selected strip width. The calculations can be performed quickly with a small computer and the design process can be interactive, arriving eventually at a structure that is predicted to be single mode in both dimensions and for both polarizations.

The design of the waveguide structures requires knowledge of the refractive indices of the materials used, as well as the physical guide dimensions. The refractive index values were obtained from a recent review by Adachi [1985]. Adachi gives equations for calculating a number of physical parameters of AlGaAs as a function of aluminum concentration. The equations are of a semi-empirical nature and have been fitted to published, experimentally-measured values. The actual refractive indices for the materials in our waveguides is not known.

Layer structures with both bulk GaAs and MQWS guiding regions were designed by the effective index method. Three different designs were completed and were sent to three different crystal-growing groups to be produced by molecular beam epitaxy (MBE). Only NEC of Japan actually came through with samples in a few months. Samples were received much later from Boeing, but have not been characterized yet. The NEC material has been used for waveguide optical bistability studies. The waveguides have the mode structures predicted, but a systematic study of the accuracy of the effective index method has not been performed. The effective index method assumes that the loading strip is much wider than it is thick and Ramaswamy cautions that the method works best far from cutoff. Our structures only marginally satisfy these requirements. Given this, plus the uncertainties in the actual indices of the semiconductor layers, it

would not be surprising if the designs are not very accurate in regard to predicted

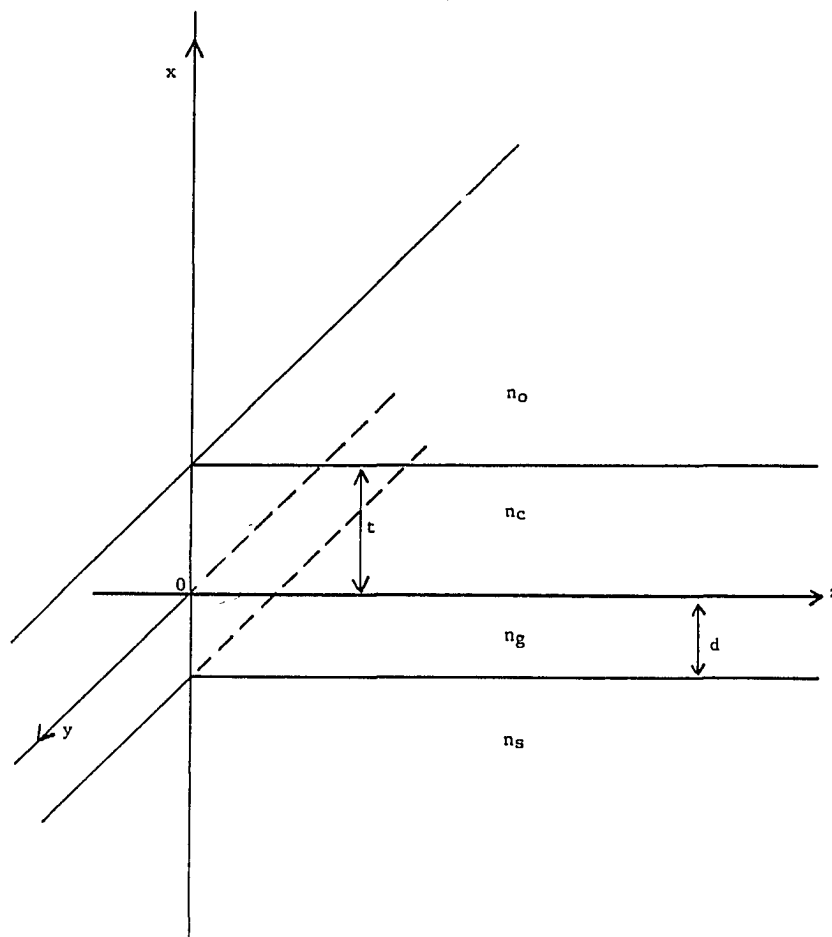


Figure 22. Four-layer slab waveguide geometry.

$\beta$  values and cutoff parameters.

As an independent effort in waveguide devices, Wayne Gibbons and Dror Sarid developed a model for a GaAs nonlinear directional coupler (NLDC) and a GaAs nonlinear Mach-Zhender interferometer (Gibbons and Sarid [1987] and Gibbons [1987]). The models are based on a coupled-mode analysis (Kogelnik

[1985]) of the devices combined with the plasma theory for the semiconductor nonlinearities. Details of their work will not be reported here. Their model is based on rectangular-cross section channel waveguides imbedded in a homogeneous lower index medium. In order to model real devices utilizing strip-loaded waveguides, equivalent channel-waveguide parameters for the strip-loaded waveguides were calculated from the propagation constants calculated by the effective index method. The NLDCs fabricated to the designs based on the model have not shown the predicted behavior. The confinement of the waveguides is apparently greater than predicted by the NLDC model. The discrepancy between the theory and the experiment may be partly explained by the use of the calculated waveguide parameters in the model.

If a waveguide has reflective ends that are sufficiently flat and smooth, it can be considered a long Fabry-Perot etalon. The actual propagation of light in the device is different from that in a simple etalon without transverse confinement, however the interference effects are very similar. The model for GaAs nonlinear Fabry-Perot etalons was used to investigate the possibility of utilizing such a waveguide etalon as an optical bistable device. The model assumes that infinite-extent plane waves are propagating through the etalon normal to the parallel mirror planes. It also does not include propagation losses other than absorption by the semiconductor. Thermal effects are also ignored. Furthermore, the nonlinear properties of GaAs, as predicted by the plasma theory, have not been experimentally investigated at the large detunings from the band edge that may be needed for nonlinear waveguide devices. Since most of these shortcomings should conspire to make the model optimistic in its predictions, the calculations were performed to see if waveguide etalons could show optical bistability under "best-

case" conditions. The model did predict that optical bistability should be observable, under these idealized conditions, at low intensities. This was encouraging. In addition, it called attention to the fact that waveguide length was an important parameter. If the waveguides were too long, the small free spectral range could be less than the laser linewidth. If they were too short, it would be difficult to be convinced that they were actually waveguides. Consideration of these factors led us to concentrate our efforts on waveguides in the 200- $\mu\text{m}$  range. Figure 23 is from a calculation for a GaAs etalon 200  $\mu\text{m}$  thick and with 30% reflectivity mirrors formed by the uncoated ends of the waveguide. The four different loops are for four different detunings of the etalon. The four detunings were simply chosen to obtain hysteresis loops closest in appearance to the experimental loop in Figure 42. The contrast of the waveguide bistability is less than that of the etalons. It is not possible to obtain the saturating, high-contrast operation in the waveguides that was predicted for the shorter etalons. This is because the long waveguides do not require a very large index change to get the necessary phase shift. The device can switch through a Fabry-Perot peak and have its output limited before the internal intensity in the device approaches saturation. The model did predict one could switch through a few orders of the Fabry-Perot resonance, and saturation effects could be seen at the higher intensities. Since the model is not a very realistic one for the waveguide etalons, the full range of simulations described earlier for the shorter etalons was not attempted. The same kinds of logic-gate and switching operations can be predicted for the waveguide devices, although the current experimental optical losses and power requirements are not very encouraging.

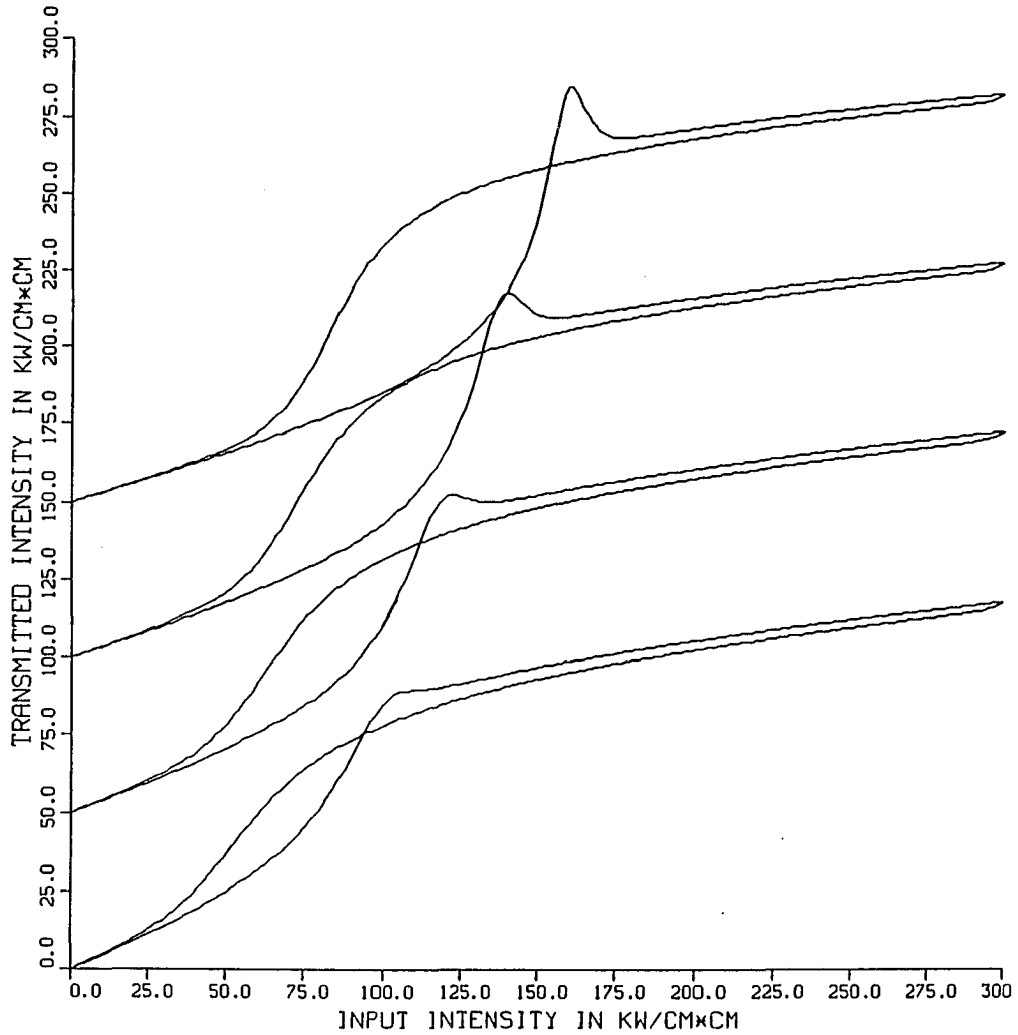


Figure 23. Transmitted intensity versus input intensity for a 200- $\mu\text{m}$  long GaAs etalon at room temperature for an excitation energy of 1.373 eV ( $-11.2 E_R$  below the band edge). The reflectivity of the mirrors is assumed 30%. Detunings of the etalons from, top to bottom, are  $-0.00034$ ,  $-0.0003$ ,  $-0.00026$ , and  $-0.00022$  eV.

## FABRICATION

A major part of this research has been the application of microlithographic fabrication technology to the fabrication of optical bistable devices. There are a few important reasons for doing this. For nonlinear optical switching or logic devices to be practical, they should be producible by modern fabrication techniques. Since the active material is a semiconductor of some current interest for electronic devices, and the structures of interest are planar, microlithographic fabrication technology such as used for integrated circuits is an obvious choice. In addition, there are benefits due to the ability to produce very small structures by this technique. Smaller-size devices can benefit from the resulting change in carrier recombination rates and from reduction of the device volume. The latter can produce a device with lower power requirements since the nonlinear optical mechanism is dependent on the charge-carrier density in the material. This is assuming that the device is operated on a short enough time scale that faster carrier recombination does not increase the power requirement. The other interesting capability of microlithographic fabrication is that it can produce large numbers of almost perfectly identical devices. Although the nonlinear optical devices discussed are very simple in construction, their operating characteristics are critically dependent on their physical dimensions. The precision available with microlithography is capable of producing large numbers of devices of similar physical properties. For several possible applications, particularly as arrays of switching elements, this is an essential requirement.

## **Microlithography**

Microlithography is essentially a photographic process that has evolved into a very sophisticated manufacturing technology (Newman [1980] and King [1981]). Its fundamental purpose is to create a pattern on the surface of a material that precisely replicates the size and shape of some original pattern. The pattern is in the form of an additional coating of some substance on the material surface that will resist further processing that affects the uncoated parts of the material. For this reason, the material used to impart the pattern is usually referred to as a resist with a prefix according to its exposure source (i.e. photoresist or e-beamresist).

The technique used predominately in the fabrication of our devices is contact photolithography, which will be described in some detail. In addition, some use was made of e-beam direct-write lithography and this was the method used to commercially prepare our photomasks. Contact photolithography consists of one-to-one reproduction of a photomask pattern onto a photoresist layer by contact printing under ultraviolet exposure. The basic steps are outlined in figure 24. A recipe with more precise processing steps for our photolithography process is given in appendix C. (The discussion here is on the principal steps and their explanation.) The resolution limits of the process are determined by the light wavelength (in our case primarily 365 and 405 nm from a mercury arc lamp), the thickness of the photoresist and the "hardness" of the contact. The latter refers to the pressure used to push the resist layer into intimate contact with the mask surface. The harder contact gives high resolution, but can be costly in broken samples and worn-out photomasks. The photomask consists of a glass or quartz

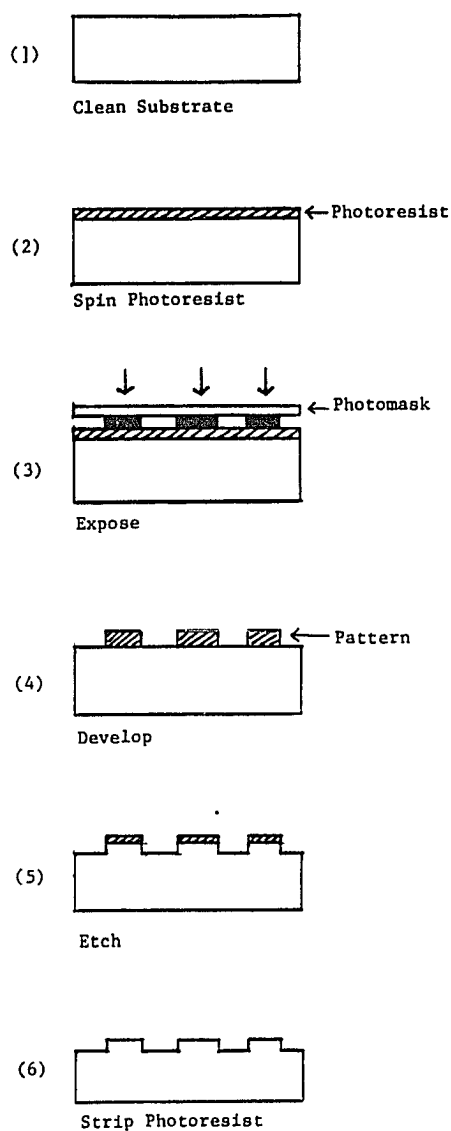


Figure 24. An illustration of the main processing steps used in fabricating etalon arrays and waveguides by photolithography and reactive ion etching.

plate with the pattern etched into a metal film on one side. The resist contact must occur on the metal side, which is somewhat fragile. It is possible to do submicron-feature contact photolithography with careful processing and deep UV exposure. The initial fabrication of etched arrays at Caltech was performed with a high quality contact mask aligner suitable for approximately one micron feature sizes, and designed for research and development flexibility. Our later efforts at the University of Arizona were first performed with mixed success using the surplus production aligners in the electrical engineering department. The difficulty was primarily in obtaining reproducible results due to constant changes in the machine characteristics, primarily lamp intensity and contact pressure. Reproducible results were obtained only by putting together a very simple homemade system consisting of a mercury lamp exposure system, that was surplused from an unsold commercial mask aligner, and a homemade vacuum chuck. The vacuum chuck consists of an aluminum plate with an o-ring groove machined in the center. A hole was drilled through the plate edgewise to intersect with a hole drilled from the face inside the o-ring sealed region. A vacuum line is connected to the hole and the vacuum seal is provided by the o-ring contacting the surface of the photomask. The pull of the vacuum applies the hard contact and the contact can be adjusted for various substrate thicknesses by using shims under the substrate (which sits face-up in the center of the o-ring groove) and changing to o-rings of different thickness. The system is primitive but has performed quite well. The major limitation of the system is that it is not capable of precise alignment of the mask with a pattern already existing on the substrate. This would be a necessary requirement for a multi-layer process such as adding ohmic contacts onto etched features.

The photoresist layer on the substrate is applied by spin-coating. The resists are sold in liquid solution in the desired viscosity. Spin speed, time duration for spinning and the resist viscosity determine the thickness of the resist layer. The resist thickness is important, not only for photolithographic resolution, but also for its ability to survive later processing intact. A thicker resist layer is generally going to last longer. There are two types of photoresist, positive and negative. The roles are entirely analogous to photographic film processing. A positive resist reproduces the opaque regions of a photomask by virtue of the exposed resist dissolving in its developer. A negative resist hardens on exposure, the unexposed regions being dissolved away. In positive resists, the exposure to UV light activates chemical reactions that destroy the polymeric bonding. Negative resists are directly polymerized by exposure to the UV light. Positive resist is the most commonly used and was used for our devices. Most of the fabrication was done with KTI 820 photoresist with a viscosity of 27 centistokes. Photoresist has a limited shelf life, so best results were obtained with fresh material.

The determination of proper exposure times is a combination of trial-and-error and careful measurement and control of the processing parameters and the final resist pattern dimensions. Exposure levels can be measured with a UV-sensitive exposure meter, and the exposure time controlled with an electronic timer. A few different exposure times can be tried. The development time is interrelated with the exposure time, so care should be taken to stay near recommended development times. The developed patterns can be examined microscopically to determine the size of the features and to look for signs of overexposure or underexposure. Overexposure will cause isolated features to come out smaller, and the effect is enhanced when other features are nearby.

Underexposure gives larger features, and exposed regions between adjacent features may not dissolve completely in the developer. Exposures need to be checked frequently with test runs because some parameters, such as the lamp intensity, are time-dependent.

The developers for photoresists are proprietary solvent mixtures that selectively dissolve the unhardened resist regions. Development is a fairly tolerant processing step. It can be observed visually, as the dissolving resist can be seen streaming into solution and a change in apparent texture of the substrate surface can be noted due to the appearance of regular surface features.

The amount of solvent present in the resist layers before and after development has an affect on its physical properties, particularly hardness and durability. The solvent content is regulated by several intermediate baking steps between the main process steps in figure 24. A prebake of the substrate is typically used to remove adsorbed water and allow better adhesion of the resist layer. After spinning, the very-liquid resist is hardened by a high temperature bake. This is important for the resist to survive the rigors of hard contact printing. After development, a further bake is used to harden the resist more so it will survive longer in the etching process.

The microlithography process is very dependent on cleanliness. When the mask pattern is exposed, every dirt and dust particle on the mask or resist layer is reproduced into the resist layer as a defect that can render a fabricated device useless or inferior. Cleanliness of the substrate before spinning is also critical, since poor photoresist adhesion is disastrous. Ultrasonic cleaning in a series of solvents is used for both mask and substrate. One of the greatest difficulties in the fabrication of devices at the Optical Sciences Center has been the lack of a

clean room for our activities.

After the subsequent processing of the photoresist-patterned device, it is usually necessary to remove the photoresist. Two different methods have been used to remove photoresist in this project. One is to burn the resist off in an oxygen glow discharge with the reactive-ion-etching system. This is often called plasma ashing. The other is to ultrasonically clean the substrate in acetone. The latter technique has been slightly more reliable. Stubborn cases sometimes require both techniques. While on the subject of photoresist removal, it is worth mentioning a technique called "lift-off". This technique is often used to produce a patterned coating on a substrate without having to etch the pattern into the layer. In this case, a photoresist layer is prepared, exposed and developed on the surface of the substrate as described earlier. A thin-film coating is then deposited on top of the resist mask. The coating will of course, cover both the resist layer and the uncovered substrate regions where the resist was dissolved by the developer. The substrate can then be dipped in a solvent solution to remove the underlying resist layer. The film adhering to the substrate surface will remain while the film deposited on resist will be lifted-off into the solvent solution. The technique is limited in application by resist and film thickness and the strength and adhesion of the film. The metallic etch masks described later for producing quantum dot samples were fabricated by this method.

The masks used to print the photoresist have been described briefly already. In the case of contact photolithography, they are one-to-one masters, and any flaw or departure from the desired dimensions will be reproduced in the devices. The masks used were commercially prepared by Micromask Inc. of Sunnyvale, CA from drawings or, in the case of the directional coupler patterns, from magnetic

tape records produced with a computer-aided-design system. The dimensions and detail of such masks are beyond the capabilities of current optical systems, so electron-beam direct-write lithography was used. E-beam lithography utilizes a scanning electron beam very similar to that used for scanning electron microscopy. The beam is steered and modulated under computer control to write a pattern onto a substrate coated with a resist layer that is sensitive to the electron flux. The effect of the flux is polymerization of the exposed region much like the effect of UV exposure on negative photoresist. A system for photomask fabrication typically has a resolution of a tenth or a few tenths of a micron. High-resolution systems are capable of writing 20-nm-wide features. Such a system was used for fabrication of quantum-dot structures that will be described later.

## Reactive ion etching

The purpose of the pattern produced by photolithography is to provide a selective barrier for some further processing of the device. In the case of the devices described here, the next step was to etch the substrate material to provide relief structures in the semiconductor layers that would provide light confinement, physical separation or carrier confinement in the material. All these structures are of necessity small. In addition, it is often required that certain layers in the structure be etched completely through. There are a large number of wet chemical etches that have been developed over the years for GaAs and AlGaAs. Some of these are capable of smooth, uniform etching. The problem with wet-chemical-etching techniques is their isotropic etching characteristic. This makes it very difficult to reproduce precise dimensions by wet etching, due to the tendency of an isotropic etch to etch the sides of a masked feature as quickly as it is etching the unmasked substrate. The result is undercutting of the masked region with the undercutting increasing with etch depth. An anisotropic etch process is a directional etching process that allows deep etching of structures without undercutting. Dry etching processes that utilize low-pressure glow discharges in some reactive-gas mixture were developed for this purpose in the seventies (Melliar-Smith and Mogab [1978]). The basic mechanism for the directionality of the etching is the momentum transfer from bombardment by ions in the discharge. The process is generically referred to as plasma etching. The particular version used in our work is called reactive ion etching or RIE. Chapman [1980] and Coburn [1982] are two good introductions to the field.

The production of a plasma or glow discharge is necessary for two reasons: one is to produce species that are far more chemically reactive than the feed gases typically are, and the other is to produce ionized species that can be accelerated by electrical fields for directional effects. A glow discharge is produced by exposing the low pressure gas mixture to an electric field intense enough to ionize some of the atoms or molecules, and maintain itself by producing more ions by

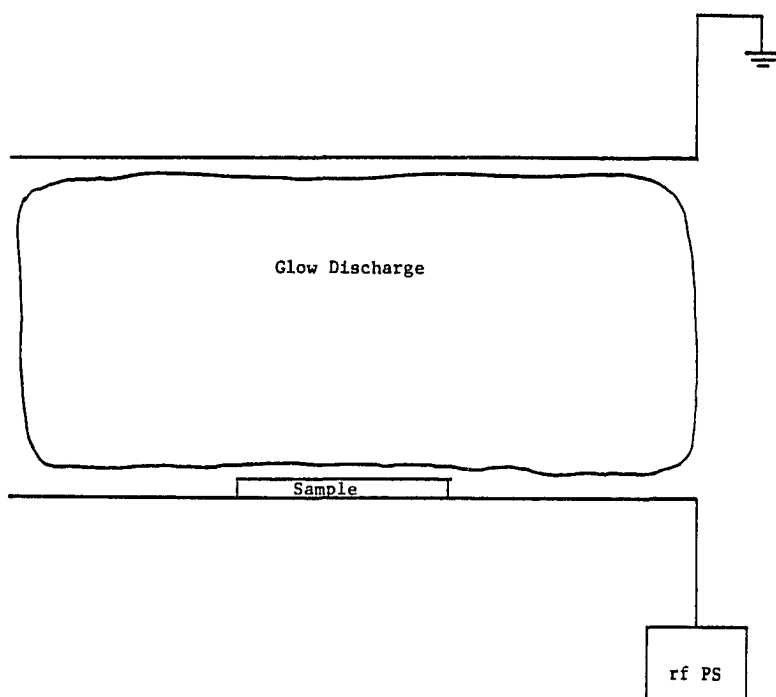


Figure 25. Schematic illustration of reactive ion etching chamber.

collision processes than are lost by recombination processes. Either a DC or AC field can produce such a plasma. There are definite advantages to using a high-frequency AC field for reactive ion etching, and all systems use radio-frequency fields to produce the plasma. A schematic reactor chamber is shown in figure 25. The substrate to be etched is typically a semiconductor that can be considered a dielectric. If a DC field were applied across the electrodes, with the substrate on the cathode, the substrate would initially experience bombardment by positive ions from the glow discharge. However, the substrate would soon acquire a positive charge sufficient to compensate for the potential between the electrodes. The positive-ion bombardment and the glow discharge would cease. Application of an AC field allows the positive charge in the substrate to be neutralized during the part of the cycle in which the substrate is subjected to electron bombardment. The situation is even better due to the great difference in mass between the positive ions and the negative electrons. The heavier positive ions are not accelerated as much by the field as the lighter electrons. The positive and negative currents must be equalized so the substrate develops a negative charge, referred to as a self-bias. Combined with the inability of the ions to follow the rapidly oscillating field, the self-bias allows for continuous bombardment of the substrate by the positive ions (Chapman [1980]).

The plasma itself is a complex mixture of gas atoms and molecules, ionized atoms or molecules, free electrons and free radicals. The degree of ionization in the plasma is actually quite small, about  $10^{-4}$ . At the pressures typical for reactive ion etching, 10-100 mT, a great variety of collisions are occurring. These collisions serve both to sustain the plasma by secondary ionization and also to produce a variety of free radicals by fragmentation of the gas molecules. The

overall temperature of the plasma is around 500 °C.

From the name, reactive ion etching, and the foregoing description of a glow discharge, it would be easy to think of the etching of the substrate as occurring by chemical reactions between the substrate material and the positively charged ions that collide with it. The truth is somewhat more complicated. The actual etch mechanisms of course vary with the specific chemicals and physical parameters. Generally, the positive-ion collisions seem to provide the activation of chemical reactions with other constituents via the momentum transfer that occurs. The free radicals in the plasma tend to be extremely reactive, and they are believed to be the primary reactants in many cases (Coburn [1982]). It is the ion collisions that give the etching its directional character. The reaction products of the etching process must be volatile enough to be pumped away by the vacuum system. The ion collisions are not extremely energetic, a few eV, and are usually (and preferably) below the sputtering threshold. If nonvolatile reaction products are formed, they are not sputtered away physically, and the substrate is quickly passivated by a protective coating. This is an important tool for obtaining etch selectivity.

There are a number of properties of a particular reactive-ion-etching process that are of interest. These include etch rate, selectivity, anisotropy, roughness or aggressiveness of the etch, and its damage to the etched substrate. The parameters that are controllable by the user are chemical composition and mixture of the etchant gases, pressure, gas flow rates, substrate temperature, rf power level, chamber and electrode geometry, external bias voltage, substrate preparation and use of dielectric isolation or conductive shielding around the substrate. Many of these parameters are closely coupled to each other. Many of the recent

developments in etching technology are attempts to acquire more direct control over the physical process parameters. For example, the positive-ion kinetic energy is mostly a function of gas composition, pressure, rf power density, and bias voltage. These are all coupled in a complex way and other factors, such as electrode geometry and placing the sample on a dielectric material, can be important. Reactive-ion-beam etching has been recently developed (Powell and Downey [1984]) in which the ion bombardment is supplied by an ion gun and, in some versions, a reactive gas supplied by differential flow near the substrate. The extra expense and complexity is to allow control of the ion kinetic energy independent of the gas composition and pressure near the substrate.

Despite the complexity of the process, there are a few basic rules to remember when developing a RIE process that are helpful in understanding the results obtained. The kinetic energy of the bombarding positive ions affect the etch anisotropy (directionality), selectivity, overall rate, and the damage to the material. Higher ion energy yields more directionality, less selectivity, and more damage. Etch rate is not as strong a function of ion energy as one might think, since non-ionized species do a major part of the work. The ion energy is controlled by the pressure of the gases (limiting the mean-free-path of the ions), the bias voltage of the substrate (which can be controlled by an external power supply), and the rf power level applied. The rf power density (actually an intensity in  $W/cm^2$ ), taking into account the electrode area, is the relevant factor, and some systems have unequal electrode areas to further complicate things. A small dielectric substrate on a large electrode surface tends not to etch well, presumably due to the tendency for many ions not to arrive at the substrate when so close to the bare electrode. It is common practice to either provide a large

dielectric surface under the sample or to cover the whole power electrode face with a plate of quartz or some other dielectric material.

The gas composition affects the etch rate, selectivity and the roughness of the etched regions. The roughness of the etching is closely related to the etch rate; very aggressive etching tends to leave rougher surfaces. They also tend to be less selective and more isotropic.

Etch selectivity is not only a matter of selecting between two different chemical composition layers (e.g., GaAs and AlGaAs) in order to stop at an interface. The limit on the depth one can etch in an anisotropic reactive ion etch is the lifetime of the photoresist or other material used to mask the substrate. The mask will erode by etching or simple sputtering during the process, and the more selective the process is relative to the mask material, the deeper one can etch before failure of a given mask thickness. Metallic masks are sometimes used for greater etch resistance, particularly if the process allows a lot of sputtering or if oxygen is present in the gas mixture.

The gas flow rates also affect the etching rate. Increasing flow rates will increase etch rates up to some point, beyond which the rates will decline slowly (Chapman [1980]). The substrate temperature also primarily affects the etch rates, higher temperatures favoring higher rates.

Developing a process consists of systematically changing one parameter at a time until either satisfied with the quality, or forced by an impatient thesis advisor to go with what you have. Some parameters that are hard to change and not well understood, such as the system geometry, are usually best left alone. Each change in a parameter should be checked more than once for repeatability. Beautiful, but unrepeatably, etching results can cause serious mental disorders.

Avoid using parameters at the edge of the equipment's ability to measure and control them.

A generic reactive-ion-etching system consists of a number of subsystems designed to provide measurement and control functions as well as the basic processing environment. The vacuum system is primary, and consists of the chamber with some means of loading in the substrates, a pumping system, and the necessary valves. Vacuum gauges are necessary to monitor the process pressure, and one is usually linked to a servo-controlled throttle valve positioned in line with the chamber to maintain a constant chamber pressure in spite of fluctuations in gas flow or pumping speed. A gas-flow control system allows flow of a mixture of gases into the chamber. Typically several flow channels are available, each with a mass-flow controller that maintains a preset flow rate for each channel. With the servo-controlled throttle valve, it is possible to control the pressure and flow rates independently over a limited range. The rf subsystem consists of the chamber electrodes, rf power supply and a tuning network to provide impedance matching. Usually there is some provision to monitor the self-bias voltage and to modify that with an external DC power supply.

Most of the etching for this thesis was performed on a commercial system, the RIE 1000 from The Semigroup of Sunnyvale, CA. The system is illustrated schematically in figure 26. The pumping system is a dual-stage system. An independently valved turbopump with its own forepump is designed to evacuate the chamber to the  $10^{-5}$  Torr range before starting the processing. This is to strip water vapor and residual gases from the substrate and chamber before etching. The process pumping system is a Roots blower, designed for high pumping speed in the less-than-one Torr range, and a large mechanical pump behind that. In

order to protect it, the mechanical pump has an oil filter and scrubber system to remove corrosive gases and etch products. All the mechanical pumps are filled with inert Fomblin (trademark) oil that resists attack by corrosive gases and acids. The system is not currently capable of etching at process pressures of less than 40 to 50 milliTorr. It is possible to modify the system to do the process pumping through the turbo-pump by putting it in-line with the Roots-blower and large mechanical pump. A new baseplate for the chamber would have to be obtained and nitrogen-purge of the turbo-pump bearings connected. So far, good results have been obtained at higher pressures and this modification has not been necessary.

The rest of the system is very similar to the "generic" system described earlier. A capacitance manometer is used to monitor process pressure and provide feedback for the servo-controlled throttle valve. The pressure transducer drifts by a few milliTorr with each run, a common problem. A cold-cathode ionization gauge was purchased that can be temporarily fitted to a chamber flange in order to check the system base pressure and the true zero point for the capacitance manometer. The RIE 1000 has an industrial process controller to run the system with automatic monitoring and programmable control of most of the user-controlled parameters.

The first applications of reactive ion etching were for silicon device processing (Bondur [1976]). Development of processes for GaAs devices has occurred more recently (Smolinsky, Chang and Mayer [1981] and Burton, Gottscho and Smolinsky [1984]). The first reactive-ion-etching in this work was performed at the California Institute of Technology in collaboration with T. Venkatesan and B. Wilkins (Venkatesan et al [1986]). The system used had been temporarily

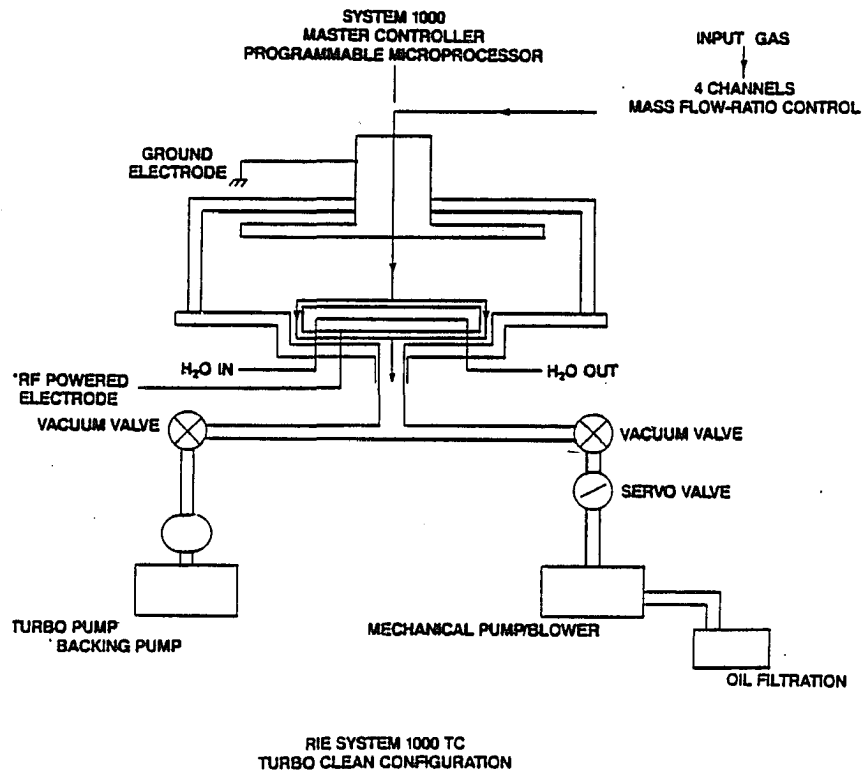


Figure 26. A schematic of the main components of the Semigroup RIE 1000 reactive ion etching system.

installed at Caltech, but was assembled at Bell Laboratories. It differed from our present system primarily in lacking automation and using a diffusion pump as the process pump. The diffusion pump resulted in very low processing pressures. The etch process used was a selective etch based on Freon-12 ( $\text{CF}_2\text{Cl}_2$ ) which etches GaAs at a good rate, but etches AlGaAs only very slowly (Hikosaka, Mimura and Joshin [1981]). The basis of the selectivity is the reaction of the aluminum in the AlGaAs layer with fluorine-containing reactants in the plasma to form  $\text{AlF}_3$ , which is a nonvolatile solid, passivating the surface. The gas mixture consisted of Freon-12, helium and oxygen in a 2:1:1 ratio. The inert helium increases ion impingement on the substrate, and the oxygen minimizes formation of polymer on the substrate, with some loss of photoresist endurance. The pressure is low, 10 milli Torr, with an rf power density of  $0.25 \text{ W/cm}^2$ . The substrates were placed on silicon wafers with no attempt to insure good thermal contact. Small squares of sheet molybdenum were positioned around the substrate on the silicon wafer. Experience had shown that this increased the etch rate substantially. The reason for this is not known, but one can speculate on the effects of induced fields from the molybdenum on the positive ions.

The etched structures by this method are quite smooth, as shown in figure 27. The selectivity was apparently good, but no attempt was made to quantitatively measure the AlGaAs etch rate. The rate for GaAs was  $0.2 \mu\text{m}/\text{min}$ . This process was installed on the RIE 1000 after its arrival at Optical Sciences. Results were never as good as on the Bell Labs system. The etch rates were quite low, leading to problems with photoresist survival. By varying some parameters, it was possible to obtain larger etch rates, with very rough surfaces. Since selectivity has not been required for our devices, the Freon-12 process has

been replaced with the  $\text{BCl}_3$  process. If selective etching is needed in the future, a rearrangement of the vacuum system described earlier may be helpful.

The impetus for developing another etch process was the need to etch multiple-quantum-well structures. Such structures consist of alternating layers of GaAs and AlGaAs. If the two materials do not etch at similar rates, the edges of the etched structures will be rough. If the etch is too selective, etching of the AlGaAs layers would be impossible with a photoresist mask because of the long times involved. Both  $\text{BCl}_3$  and  $\text{Cl}_2$ , and mixtures of the two, were initially studied as nonselective etchants based on published reports (Tamura and Kurihara [1984]). A systematic characterization of the etch properties as a function of gas mixture and other parameters was carried out by Doug Hendricks and is reported in detail in his Master's thesis. (Hendricks [1987]) The best process was a pure  $\text{BCl}_3$  plasma at 40-50 milliTorr with an rf power density of  $0.4 \text{ W/cm}^2$  on the RIE system. This compares well with the published parameters in a different system. The finalized procedure includes laying the substrates on silicon wafers with some vacuum grease between them to increase the thermal contact. The silicon wafer is in turn contacted to the water-cooled rf electrode with a small amount of vacuum grease. The characterization studies had shown that the etch rate varied strongly with the thermal contact of the substrate, presumably due to temperature dependence of the etching. This process is currently in use, but still suffers from a tendency for etch rates to vary from run to run. The quality of the etching obtainable is illustrated in figures 30, 34 and 35.

### **Fabrication of etalon arrays**

The first devices fabricated were the arrays of  $9 \times 9 \mu\text{m}$  mesas pictured in figure 27. The arrays of GaAs elements or pixels could then be sandwiched between dielectric coatings to make etalon arrays. There were two motivations for the etching. One was to provide isolation of the individual devices from each other on the scale of the focal spot sizes used to operate them. Studies of diffraction in GaAs bistable devices had shown limitations of device spacing due to crosstalk between adjacent focussed spots on a single device. (Tai, Moloney and Gibbs [1982]) By etching all the way to the underlying AlGaAs etch stop layer in a GaAs on AlGaAs structure grown by MBE, it was possible to achieve complete isolation of the individual squares. The other motivation was to shorten the switch-off time of the devices. The switch-off time of a GaAs nonlinear Fabry-Perot etalon operating as a bistable optical switch is determined by the relaxation time of the charge carriers excited in the semiconductor. By etching small structures into the GaAs layer without the usual AlGaAs top window, it was possible to make devices with non-passivated surfaces close to the charge carriers on five sides. The surfaces provide recombination sites for the charge carriers and can considerably shorten the carrier lifetime in the material.

The selective-etch process was advantageous, because it was possible to use the molecular-beam-epitaxy process to define the etch stopping point. The MBE process is capable of growing layers with interfaces between layers that are almost atomically flat. By using a selective etch that could stop promptly at the AlGaAs layers, the individual GaAs pixels could be completely isolated without further weakening the structure by etching into the AlGaAs layer. The disadvantage of

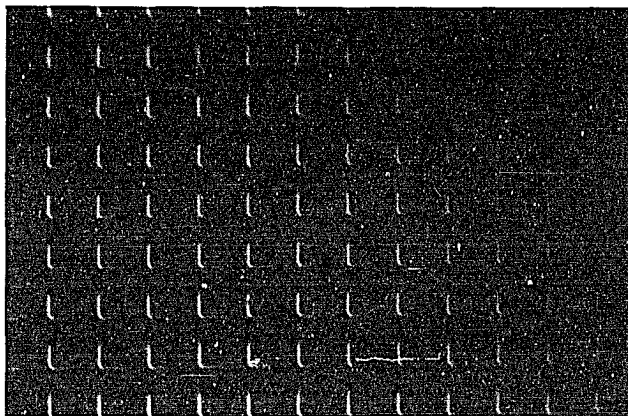


Figure 27. An etched array of 9 X 9- $\mu\text{m}$  square mesas in a 1.5- $\mu\text{m}$  thick layer of GaAs.

the selective-etch process is that one is limited to the use of bulk GaAs for the devices. Since the fast carrier recombination was one of the goals, multiple-quantum-well samples would not have been appropriate anyway, since the barrier layers would prevent diffusion of carriers to the top surface.

The structure used was a simple 1.5- $\mu\text{m}$ -thick layer of GaAs on top of a 0.25- $\mu\text{m}$   $\text{Al}_{0.35}\text{Ga}_{0.65}\text{As}$  stop layer. The structure was grown at Caltech by Steve Smith in Amnon Yariv's research group. Conventional contact photolithography, as outlined before, was used to pattern the sample with a photoresist etch mask. A

photomask was specially prepared for the project at Bell Communications Research by e-beam lithography. Photolithography was accomplished with Kodak 820 photoresist and a Karl Suss contact mask aligner. The exposure and development steps were very similar to those outlined earlier in the discussion of photolithography. The patterned pieces, approximately one centimeter square, were etched in the Freon-12, helium and oxygen mixture for 10 minutes to etch completely through the 1.5  $\mu\text{m}$  thick GaAs layer. Patterns of square mesas that were approximately 5, 10 and 20  $\mu\text{m}$  on a side were prepared by this technique.

The next step in the processing consisted of removal of the GaAs substrate upon which the MBE layers were grown. The exact preparation of an array sample depended on whether it was to have mirrors applied by physically sandwiching between two coated glass mirrors, or if one or more reflective coatings were to be directly applied. In all cases the substrate was necessarily removed. First the substrate side was ground to a thickness of 20-30  $\mu\text{m}$  with aluminum oxide polishing compound or commercial lapping film. The remaining substrate was then removed by a wet chemical selective etch using 30% hydrogen and concentrated ammonia (LePore [1980]). This technique is based on use of a liquid jet system to remove the weak oxide layer that the etching solution creates on the GaAs surface. The procedure currently used has changed somewhat from the one written up by Jack Jewell (Jewell, Gibbs, Gossard, Passner and Wiegmann [1983]). Only a single stop layer is used, and the sample is usually mounted on a sapphire substrate before the grinding step and left mounted the same for etching. It may seem odd to utilize two different selective etch processes, one a dry (plasma) process and the other a wet process on the same device. Some experimentation on using the Freon-12 selective etch to remove the substrate was

performed with the system at Caltech. The results were mixed, with some polymer deposition occurring. The Freon-12 etch tried at Optical Sciences was too slow to be practical. The main difficulty with using a dry etch to remove the substrate layer is the lack of a physical means of removing surface contamination after closing the chamber and during the etch process. Any dust that settles on the surface or any polymer or sputtering deposition that occurs during the etch will act as a mask layer, leaving an uneven etch surface. The jet etching process physically washes the surface during etching, preventing such an occurrence. The disadvantage of the jet process is that it cannot currently be utilized for samples larger than a few millimeters in diameter. The published selectivity ratio for GaAs versus AlGaAs for the Freon etch (Hikosaka, Mimura and Joshin [1981]) is much higher, as high as 200 for a 30 % aluminum concentration, compared with 20 for the jet etch with a similar aluminum concentration (LePore [1980]). Substrate removal by selective reactive ion etching may still be an attractive option for devices in which the mirrors are applied by direct thin film deposition onto the structure itself by a process such as MBE. In those cases an etch defect would only be a localized fault and not affect the whole etalon structure.

In order to form higher finesse etalons, it is necessary to apply mirrors to the outside surfaces of the GaAs arrays. One method used is to sandwich the sample between dielectric-coated coverslips with a small amount of UV-setting glue (Norlund #61). A simple fixture is used for this purpose that allows the contact of the mirrors to be adjusted by three screws. By monitoring the interference fringes in the sample with a monochromatic, near-IR source and an IR-sensitive microscope or TV camera, the fixture can be adjusted for the uniformity and detuning of the etalon. Mirrors can also be applied to the sample by direct

deposition of the dielectric coatings. In that case, the detuning of the etalon is determined by the physical thickness of the material, and there is no latitude for adjustment of the detuning.

### Fabrication of quantum dot structures

As discussed earlier for MQWS, confinement of charge carriers to small spatial structures can change the material's nonlinear properties. Recently, Banyai and Koch have described the effects of producing three-dimensional quantum confinement structures in a semiconductor such as GaAs that are somewhat larger than the Bohr diameter of the excitons in the bulk material (Banyai and Koch [1986]). Such quantum-confinement structures can be created by etching isolated mesas or posts into a multiple-quantum-well structure. Although the structures are similar in shape to the arrays, there is a major difference in scale. The theory predicts large effects only for devices (in GaAs) of 50 to 150 nm in diameter. Features of this size are beyond the capabilities of photolithography. Instead, electron-beam lithography, which has been briefly mentioned, was utilized through the National Nanofabrication Facility at Cornell University. There a JEOL JBX 5DU electron-beam pattern generator was used to fabricate an etch mask by direct-write onto the resist. The resist used was PMMA (polymethyl methacrylate), a common e-beam resist. A 2500-Å layer was spin-coated and baked. After exposure and development of the dot pattern, which now consists of small holes in a hardened resist layer, 800 Å of nickel was evaporated onto the sample. The PMMA layer was then "lifted-off" with methylene chloride as a solvent, leaving small metal dots behind as an etch mask.

The completed metal on semiconductor patterns were etched by both reactive-ion etching and chemically-assisted ion-beam etching (CAIBE). CAIBE is a variation of RIBE in which an ion beam is produced and directed at the substrate to be etched. The ion beam consists of inert gas (Argon) ions accelerated to a

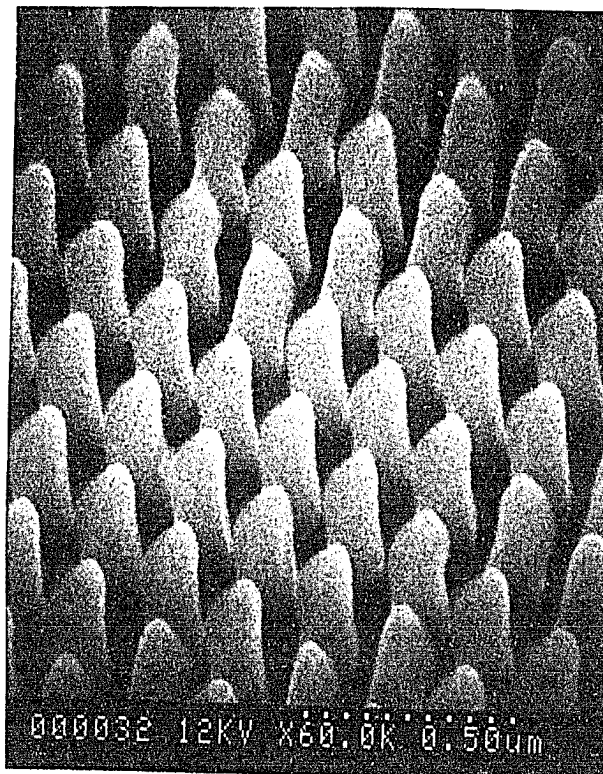


Figure 28. SEM micrograph of very small posts etched in a 299 Å MQWS sample to make quantum dots.

moderate energy (500 eV). A separate gas inlet is positioned near the substrate to allow a flow of reactive gas ( $\text{Cl}_2$  in this case) across the substrate. The ion bombardment activates the chemical reaction of the gas with the surface. The mechanisms are similar to those of RIE, but the process parameters are more controllable. The etching is highly directional due to the ion beam. The etch rate is about  $0.5 \mu\text{m}/\text{min}$  and no selectivity is observed between the GaAs and the AlGaAs. The same process has been recently used to etch mirror facets for high-

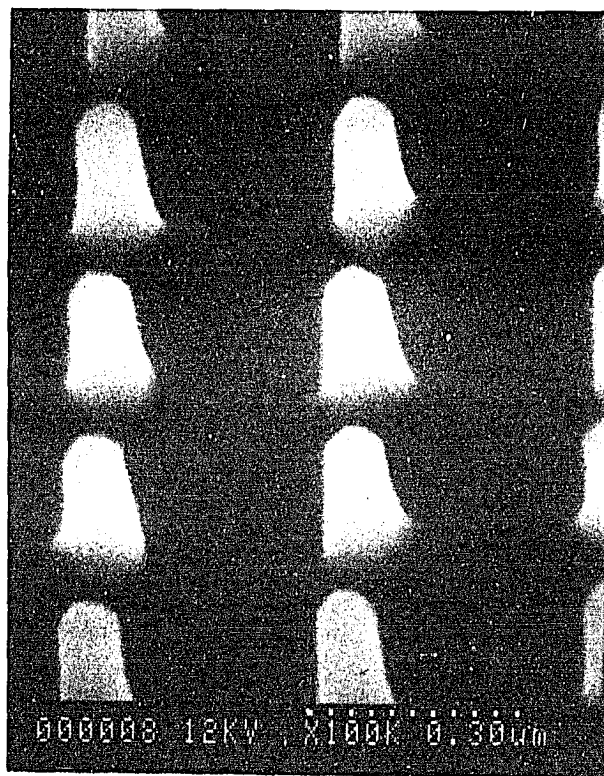


Figure 29. SEM micrograph of posts etched in bulk GaAs by CAIBE with  $\text{Cl}_2$ . Shallower etching results in more uniform features.

power laser diodes (Tihanyi et al [1987]). An actual MQWS sample with  $299 \text{ \AA}$  wells was etched by the CAIBE method, as well as several bulk GaAs practice pieces. The MQWS sample served as a test of the technique to be sure that the tall, thin structures could be etched in the MQWS material. Figure 28 is a scanning-electron-microscope (SEM) micrograph showing 120-nm-diameter posts etched in the 30-nm wells to a depth of 800 nm. Figure 29 shows posts etched only 30 nm deep in a bulk GaAs wafer, and illustrates the quality available if the

etching is not so deep. The tapering of the etched structures may be attributable to deflection of the ion beam by grazing-incidence collisions with the structure and mask sides. A few GaAs practice pieces were also etched by reactive ion etching after returning to Optical Sciences. Figure 30 shows a SEM micrograph of

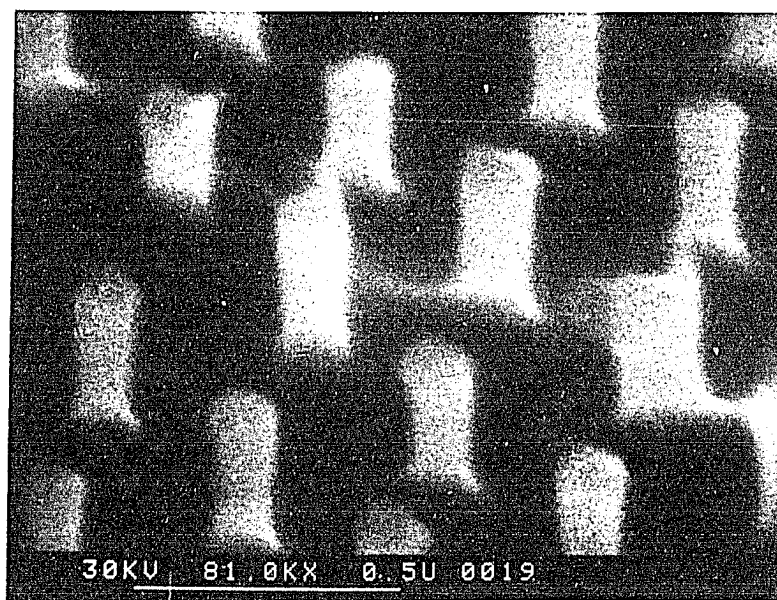


Figure 30. SEM micrograph of sample similar to that in Fig. 29 that was etched by RIE in  $\text{BCl}_3$ . Poor photo quality is attributable to a less capable SEM.

structures etched in GaAs with the  $\text{BCl}_3$  RIE process. The poor quality of the

photograph is attributable to the difference in quality of the SEM available at Cornell University and at the University of Arizona. The etch quality of the reactive-ion etched sample appears good, with more vertical side walls than the CAIBE etched samples. The reactive ion etched structures are perhaps less uniform in size, and most of the original metal mask layer appears to have survived. Although the fabrication process for quantum dot structures has been developed, a suitable sample for actual use has not been obtained at the time of this writing. The plan is to continue the project as soon as a sample is grown to our specifications.

### Fabrication of waveguide devices

The other major fabrication effort was in waveguide devices. The fabrication requirements for waveguides are for smooth surfaces to reduce scattering losses and for uniformity of the etch depth and guide width. Nonlinear operation of waveguide devices requires the capability to use a laser source detuned further from the band edge than for etalon operation. This is to minimize absorption losses. For this reason, it was felt necessary to use MQW structures for some of the devices. It was also necessary to use an AlGaAs cladding layer above the guiding layer to take advantage of lower-loss strip-loaded structures.

The need to produce smooth etching of both GaAs and AlGaAs layers

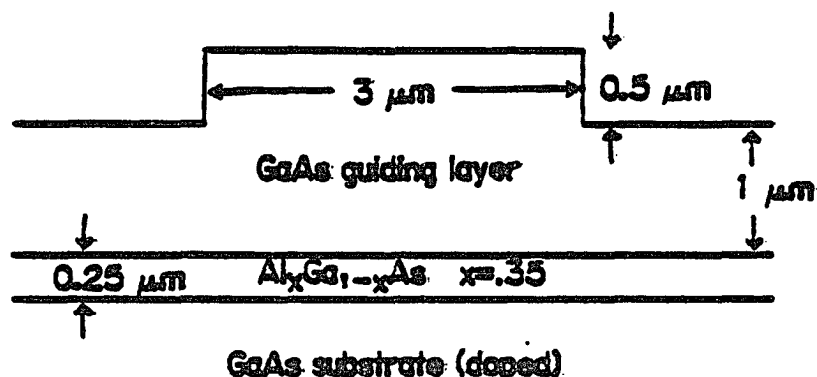


Figure 31. Cross section of ridge waveguides.

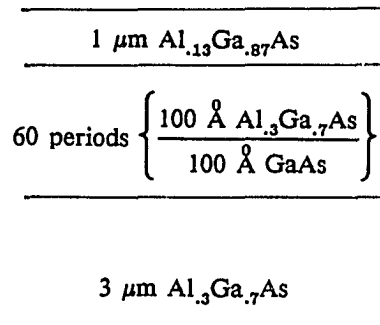
required the use of the  $\text{BCl}_3$  etch process. Since the etch depths are not deep, about one micron, a photoresist mask is sufficient. The devices initially fabricated were simple waveguides to be used for optical bistability studies. The first

waveguides were etched into MBE-grown samples that were on-hand from previous experiments. A quantity of the 1.5- $\mu\text{m}$  bulk GaAs sample that was used for the array work was still available. Ridge-waveguide structures were etched as shown in Figure 31. Due to the thinness of the AlGaAs layer, there were large losses into the substrate. The guides were later found to be multimode, due to the large index difference between air and GaAs and the fairly thick guiding region.

Using the effective-index method outlined earlier, samples for strip-loaded waveguide structures were designed. Both MQWS and bulk GaAs samples were designed and grown to our specifications at NEC in Japan. The two structures are illustrated in figure 32. By etching a strip in the top AlGaAs cladding layer, as shown in figure 33, a single-mode waveguide could be fabricated. Figure 34 is a SEM micrograph of a strip-loaded waveguide with a MQW guiding region. The dark residue near the end of the guide is photoresist that was not completely removed. Its effect on the guiding is negligible.

After successful observation of optical bistability in the strip-loaded waveguides, attention was quickly focussed on fabricating nonlinear directional couplers. The couplers consist of two parallel waveguides that are located close enough to each other for the light to couple coherently from one guide into the other and perhaps back again. The designs for the couplers were originally based on theoretical calculations by Wayne Gibbons and Dror Sarid [1987]. The photomask patterns were laid out with a commercial computer-aided-design system at the NNF at Cornell University. The photomask pattern included a range of guide widths and separations to allow some experimental variation of the design parameters. The process of photolithography and etching of the directional

(a)



(b)

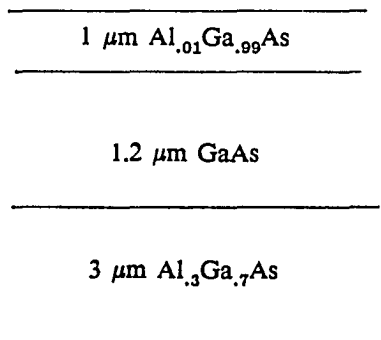


Figure 32. Structure of MQWS (a) and bulk GaAs (b) sample grown by MBE at NEC.

couplers is identical to that for the single waveguides, with the exception that the guide and spacing dimensions are more critical. The photomask includes couplers with spacings between guides of 1,2,3, and 4  $\mu\text{m}$ . Figure 35 shows the end of a directional coupler with a spacing of one micron. The pattern has one guide longer than the other to provide a lead-in for the end-fire coupled light. The

exact etch depth for the strip in the cladding layer in the directional coupler is a

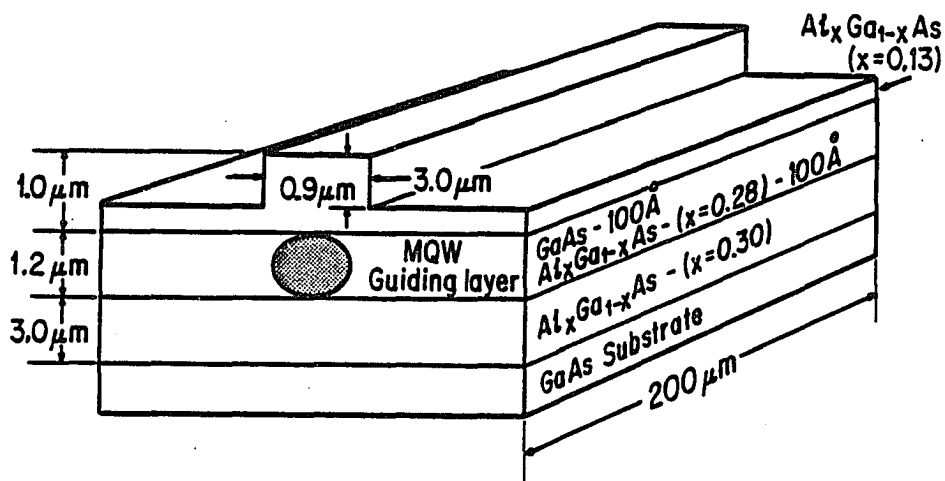


Figure 33. Strip-loaded waveguide structure.

critical parameter. Initial attempts, based on the Gibbons and Sarid calculations, gave waveguide structures in which the light was too tightly confined, so that linear coupling was not observable. Systematic variation of the strip etch depth yielded devices that have shown linear coupling for values of around  $0.8 \mu\text{m}$ . Nonlinear properties of the devices are still under investigation.

The waveguide devices do not require complete removal of the substrate as needed for etalon-type devices. They do, however, require cleaving to a desired length. It is necessary that the cleaved faces be of as high quality as possible, since they have a strong effect on the coupling in and out of the guide. In order to achieve the best cleave possible, part of the substrate is removed by grinding. This makes the sample thinner and easier to cleave into small pieces. The best

sample thickness seems to be around 70 to 60 microns. The cleaving can then be performed by carefully rocking the edge of a fresh scalpel blade onto the edge of the sample. With practice it is possible to cleave pieces less than 150 microns long. It is important that the waveguides are aligned parallel to a cleavage plane during the photolithography step, otherwise all the waveguides will have slanted

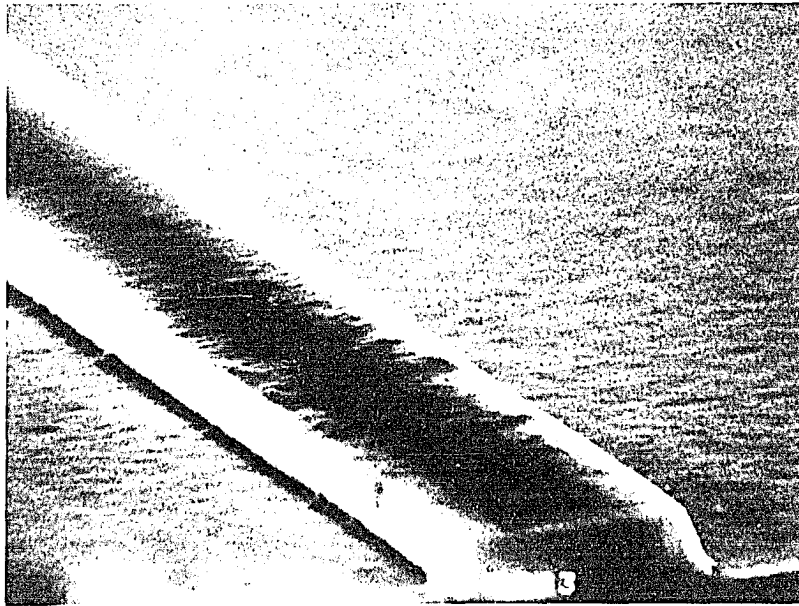


Figure 34. SEM micrograph of strip-loaded waveguide after etching and removal of photoresist layer (some photoresist is still remaining). The scale bar in the micrograph is 5  $\mu\text{m}$ .

ends.

The waveguides resulting from the cleaving process are transverse to the thin slivers of semiconductor. They are extremely fragile, and the shorter pieces can

be very difficult to handle. The sample mounting technique that has been developed is probably not ideal, but it works. The small pieces are handled by vacuum tweezers. Mounting blocks for the sample are prepared by cutting rectangular pieces of some material whose thickness is slightly less than that of the sample. For the optical bistability samples, we used pieces of brass shim stock of the appropriate thickness. For the directional couplers, pieces of microscope slide

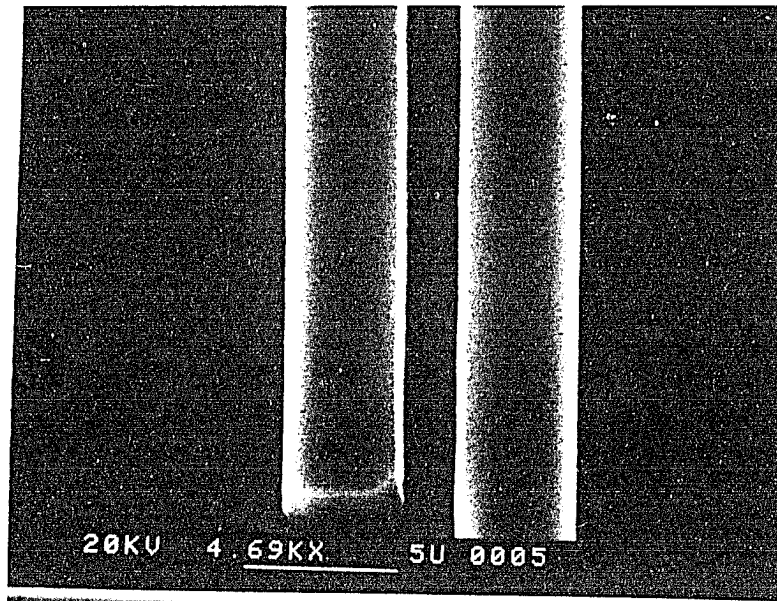


Figure 35. SEM micrograph of input end of directional coupler with  $1\text{-}\mu\text{m}$  spacing between waveguides.

painted black were used. It is important that the block is opaque, otherwise interference fringes may be confusing during sample alignment. One edge of the

block needs to be square and flat. A thin layer of transistor heat sink compound is spread on that edge. The heat sink compound was used for its mild adhesive qualities, rather than its thermal conductivity. With the sample laying waveguide-side down on a clean, flat surface, it can be gently picked up by pressing the coated edge of the mounting block onto the sample. If the block is thicker than the sample width, heat sink compound will cover the waveguide faces. If the sample is greatly tilted, it will probably have to be remounted. The major difficulty with the method is getting heat sink compound on the cleaved faces. The greatest advantage is that the sample can be removed and cleaned by ultrasonic cleaning in acetone or methanol and remounted. The heat sink compound does not seem to dry out. All subsequent handling can be done with the mounting block without damaging the waveguides. A new mounting block is used for each sample.

## OPTICAL EXPERIMENTS

The optical experiments performed with the devices fabricated as described in the previous section are conveniently divided into etalon and waveguide experiments. The apparatus and operating principles are similar for the two types of devices.

### **Etalon array experiments**

The first experiments performed with the etched pixels fabricated with reactive ion etching were measurements of the relaxation time of the devices. Relaxation times were measured for both the etched pixels and for unetched portions of the same sample (Lee et al [1986]). Both measurements were expected to show reduced carrier lifetimes due to the lack of an AlGaAs "window" that normally inhibited surface recombination of carriers. The measurement of the carrier lifetime was based on a direct measurement of the relaxation time or recovery time for the device when operated as an all-optical logic gate.

Earlier experiments with MQWS etalons had demonstrated the use of GaAs etalons as high-speed logic gates (Jewell et al [1985]). The experiment was a two-wavelength pump-and-probe experiment with 7-ps pulses tuned above the band edge for the pump, and an effectively cw probe beam below the band. A full set of logic functions was demonstrated in that experiment. The NOR-gate operation was of particular interest. In this case the probe beam was tuned to resonance

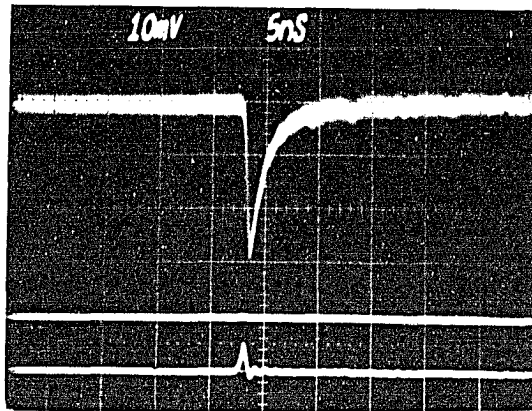


Figure 36. NOR gate response to  $< 14$  pJ pump pulse at 825 nm. Pump pulse is shown on lowest trace. Upper-most trace is transmission of much longer probe pulse at 872 nm. Middle trace shows base-line for probe pulse.

with the unexcited etalon. Excitation by the pump beam detuned the etalon, causing the probe transmission to drop dramatically. The etalon mirrors were optimized for two-wavelength operation. As shown in Figure 36, the relaxation of the device after absorbing the pump pulse can be easily measured. In that experiment, with a conventional MQWS of  $76\text{-\AA}$  well thickness, the relaxation time for the etalon was found to be approximately 5 ns. The actual carrier lifetime in similar samples was measured by Chemla, Miller, Smith, Gossard and Wiegmann [1984] to be 30 ns. The difference can be accounted for by the rapid diffusion of excited charge carriers out of the approximately  $10\text{-}\mu\text{m}$ -diameter focal spot (Lee

et al [1986]).

A similar experiment was initially attempted with the 1.5- $\mu\text{m}$ -thick GaAs "windowless" sample. The relaxation times were unresolvable due to the approximately 0.5-ns response time of the silicon avalanche photodiode detector. It was then decided to go to a streak-camera detection system to obtain higher resolution. The final experimental setup is illustrated in Figure 37. The pump light source was an 82-MHz mode-locked argon laser operating at 514.5 nm with a pulsewidth of 180 ps. An acousto-optic modulator (AOM-1) was used to gate the pulsetrain into 250-ns packets at a 400-Hz repetition rate. This served to reduce the heating of the sample. A second acousto-optic modulator (AOM-2) was driven at the same rate to provide a synchronized series of pulses from a cw dye laser that was tuned below the band-edge of the material (885-889 nm). The photodetector (D-1) was monitored with a fast oscilloscope (Tektronix 7104) to optimize the alignment of the sample and light beams. The trigger source for the streak camera, oscilloscope and function generator was the SYNC-OUT signal from the mode-locker driver which was frequency down-converted through a circuit in a cavity-dumped-dye-laser driver (the cavity dumper was not being used). The circuit was designed to precisely divide the 82-MHz mode-locker frequency and provided a lower frequency trigger source with very little jitter. The streak-camera resolution is 5 ps. The streak-camera data for both AND- and NOR- gate operation are displayed in Figure 38, for samples with and without the etched structure. The etched array shows a 200-ps relaxation time and the unetched sample a 350-ps relaxation time. Deconvolution of the 180-ps input pulse gives carrier lifetimes of 80 ps and 180 ps. Both values are dramatic reductions from the 30 ns of conventional samples. The difference between the etched and

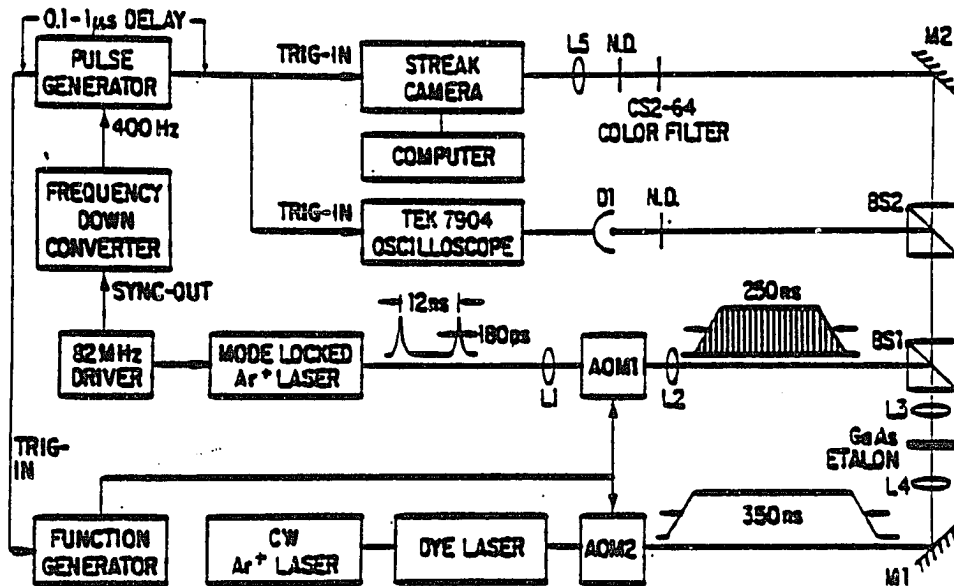


Figure 37. Experimental setup for streak-camera observation of fast, two-wavelength NOR gate in etalon array.

unetched values can be partly accounted for by the increase in surface recombination sites as expected. The actual increase in surface area was proportionately not as large as the decrease in relaxation time. It has been conjectured that surface damage to the edges of the pixels during reactive ion etching might have had an additional effect (Venkatesan et al [1986]). Studies have shown that reactive ion etching of GaAs can produce damage that extends more than 500 Å into the etched surface (Pang et al [1983]). The energy requirements for switching were about 1 nJ per device, which is much larger than the 3 pJ attained in the MQWS NOR-gate experiment (Jewell et al [1985]). This is attributable to differences in the etalon finesse, which was optimized for two-

wavelength operation in the former experiment, and the pump wavelength. In the earlier NOR-gate experiment, the pump beam was only slightly inside the the band edge. In the "windowless" sample measurements, the pump was visible and thus well inside the band, and could be expected to impart considerable thermal energy to the excited carriers.

After completion of the NOR-gate experiments, there was interest in finding out if the etched pixels could show bistability. Initial efforts with a cw dye laser modulated at the usual microsecond pulsewidths showed very poor nonlinear behavior. Some hysteresis could be observed with the unetched sample, but thermal effects were severe. This is attributable to the short carrier lifetimes in the samples. The generation of charge carriers does not integrate over long pulses, but the thermal effects do.

At that time Brian McGinnis had assembled a pulsed dye laser system, consisting of a Quantel passive-Q-switched, neodymium-YAG laser pumping a Littman-type dye laser (Littman and Metcalf [1978]). Although originally built for visible light use, the system could be operated in the near infrared by using LDS-821 dye dissolved in propylene carbonate and changing the grating. Because of the low repetition rate of the pump laser (20 Hz), it was inconvenient to use sampling techniques. Instead, fast plug-ins with a 1-GHz bandwidth were used with a Tektronix 7104 oscilloscope, which has an intensified CRT. The detectors have a 0.5-ns rise time. The dye laser was not capable of tuning far enough into the infrared to observe room-temperature bistability with the bulk-GaAs samples. In order to shift the band edge of the samples sufficiently, they were cooled to 150-160 K with a Joule-Thompson-effect micro-refrigerator manufactured by MMR Technologies.

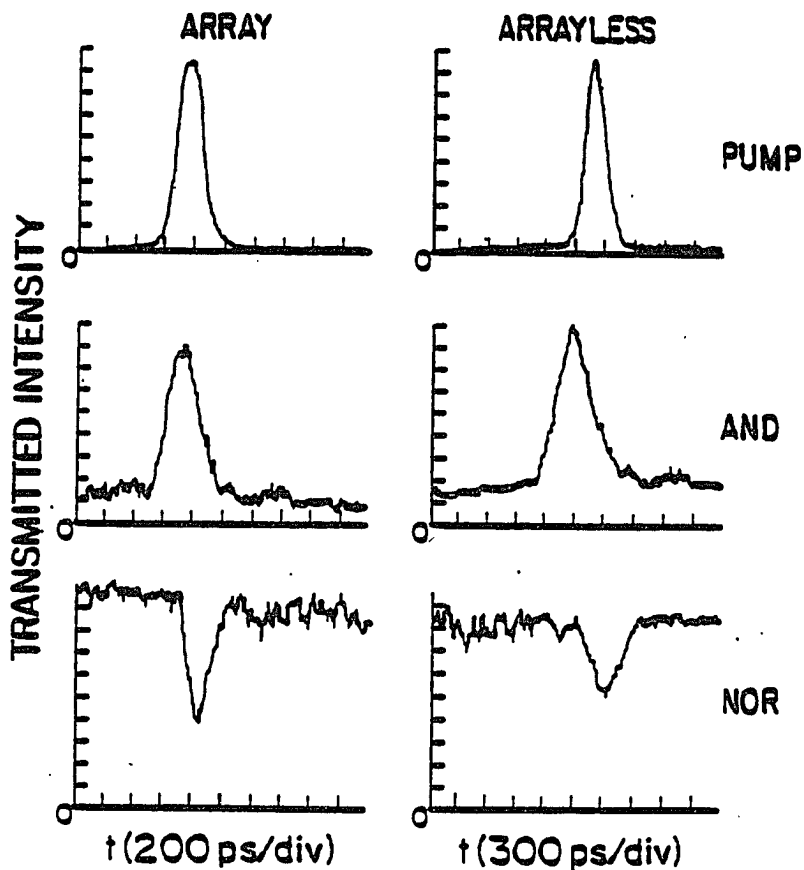


Figure 38. Streak-camera trace of pump pulse, AND gate transmission and NOR gate transmission. Left side is for  $9 \times 9 \mu\text{m}$  etched pixel and right side is for unetched windowless sample.

Hysteresis loops for both the etalons with etched pixels and without etching are shown in Figure 39. The laser pulses were often very noisy, giving the bizarre shapes at the right apex of the curves. Despite the noise, fast switch-up of the device transmission is apparent, as well as the slower switch-down. The light was of 844-nm wavelength in 8-ns FWHM pulses. The peak intensity for

switching an etched  $9 \times 9 \mu\text{m}$  device was 5 mW (Warren, et al [1986]). This is a value that is comparable to the best low-power measurements of optical bistability at room-temperature in MQWS samples. The report of the switching intensity for the arrays was met with some skepticism, so a careful check was made of the accuracy of the optical pulse-energy meter (Laser Precision model Rj-7100) used to make the measurement. The meter was found to give an accurate measurement of the integrated pulse-energy at that wavelength by comparing measurements made with fast detectors and an oscilloscope, and comparing with measurements of average power using commercial power meters. The low-power operation is actually not as unusual as it was first thought. The ratio of pulse length to carrier lifetime for the etched arrays is about the same as that for conventional samples with 10 ns effective carrier lifetimes and 1- $\mu\text{sec}$  pulse length.

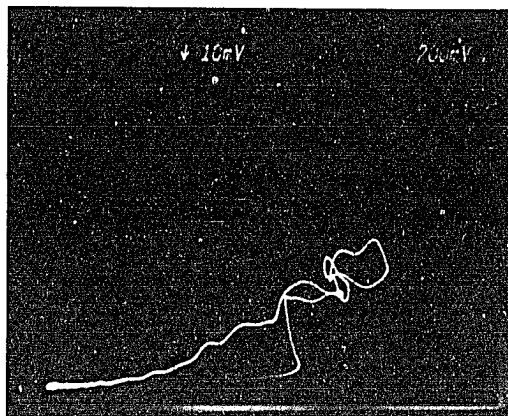
Uniformity is needed for the etalon arrays, so that different positions on the array will show the same response at some fixed wavelength. The NOR-gating and optical-bistability measurements were made with etalons constructed by sandwiching the GaAs samples between glass coverslips that have high-reflectivity dielectric coatings. Most of the etalons were not particularly uniform, since having some wedge in an etalon allows one to vary the detuning of the etalon by physically changing the position of the light beam on the etalon. It is possible to construct a fairly flat etalon by careful adjustment of the mirror spacing during the gluing step described earlier. One of the etalon arrays fabricated in this way was observed in the NOR-gate experiments to be very uniform, with a single interference fringe covering most of the sample. Quantitative measurements of the sample were not made until after the fast optical bistability studies were started. During the first attempts to observe optical bistability with the 10-ns pulses, the

flat etalon sample was thermally damaged. The damage created a bubble in the sample center that affected its optical uniformity. Subsequent optical measurements of the Fabry-Perot peak position at different points on the array, avoiding the damaged region, still showed a spread of approximately 5 nm in position. The instrument widths of the individual etalon pixels varied around 6-8 nm, so flatness achievable by this method is quite good. If flat mirrors are used, better results can be achieved (Jewell, Lee, Duffy, Gossard and Wiegmann [1986]).

A systematic measurement of the uniformity of the array samples, without compensating with external mirrors, would be interesting. Several small pieces were mounted on the inside edge of beveled aluminum washers and sent away for direct dielectric coatings on both sides. The coatings were specified to have 90-92 % reflectivity for GaAs substrates. The fluorescence from a LDS-821 dye jet was used as a broadband source and the spectral transmission peaks were monitored with the optical multichannel analyzer (OMA). Microscope objectives allowed one to focus substantially all of the incident light onto a single pixel. Alignment of individual pixels with the focussed light could be monitored with a TV camera.

The quality of the coatings varied from sample to sample. Most of the samples were small, and the coatings may have been degraded by "shadowing" of the deposition by the edge of the mounting washer. One smaller sample contained a rectangular array of roughly 8 X 7 pixels. Several representative pixels were measured across the sample. The devices had an average instrument width of 12 nm. The instrument widths varied in an apparently random way from pixel to pixel, with a few devices not showing any interference effect. The measured extreme spread in peak position was 5 nm.

(a)



(b)

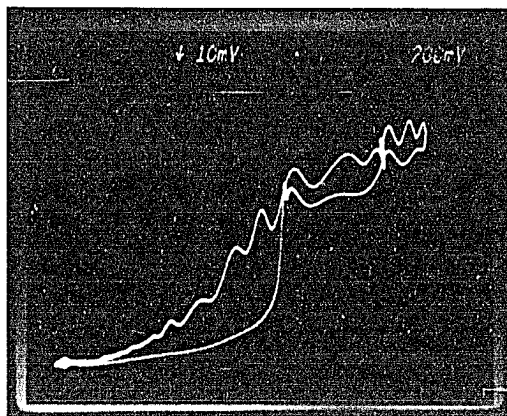


Figure 39. Fast optical bistability in etched  $9 \times 9 \mu\text{m}$  pixel (a) and in unetched "windowless" bulk GaAs (b). Strange loops are due to very noisy laser.

A much larger sample containing an estimated 350-400 devices was also measured for uniformity. The sample was approximately  $13 \times 29$  pixels with a

sizable region along one side without any etched pixels. The coatings seemed to be of higher quality, with an average instrument width for the pixels of 6 nm. Over comparable areas, the measurements showed similar variations in peak spectral positions as in the smaller sample. Over regions of 20-30 pixels, most would show Fabry-Perot peak positions within one-half instrument width of each other. By scanning over the larger area, it was possible to see that the sample had some wedge in its thickness. A measurement of pixels along the long sample axis, which corresponded roughly to the wedge direction, showed an extreme spread of 25 nm in Fabry-Perot-peak position. Expressed more quantitatively, using a measurement of the peak shift over a span of 22 pixels, one can calculate a corresponding change of sample thickness of  $660 \text{ \AA}$  per mm of sample length (assuming an index of 3.5). This was a disappointing result for the sample uniformity. It is reasonable to suspect that some of the nonuniformity was the result of the substrate removal process. The wedge observed corresponds to a 2 % thickness variation of the  $1.5 \text{ }\mu\text{m}$  GaAs layer over a two inch wafer, which is the current uniformity specification of some MBE system manufacturers. This illustrates how critical the uniformity requirements really are.

## Waveguide experiments

Previously reported work on optical bistability in GaAs/AlGaAs waveguides has included thermally-induced, increasing-absorption bistability in a slab waveguide (Walker, Aitchinson, Ritchie and Rogers [1985]) and increasing-absorption bistability utilizing the self-electro-optical effect in a slab waveguide (Weiner et al [1985]). Optical switching and dispersive optical bistability of electronic origin was reported for strain-induced channel waveguides (Li Kam Wa et al [1986]). The latter observation was very similar to ours, except the bistability and nonlinear phase shifts observed were less pronounced and the waveguide structure, based on induced strain, is very different (Kirby, Selway and Westbrook [1979]). Our own efforts focussed on observing optical bistability in waveguides produced by reactive ion etching as described earlier.

The experimental setup for observing optical bistability in the waveguide structures is illustrated in Figure 40. It is a straightforward modification of the ones used for earlier optical bistability experiments in shorter etalons. The laser source is a Coherent 599-01 dye laser with LDS-821 dye pumped by a Coherent Innova-20 Argon laser running single-line with approximately 7 watts at 514.5 nm. The dye laser output is modulated by an acousto-optic modulator (AOM) which is driven by a Tektronix PG 508 pulse generator. The modulated input beam is monitored through the beamsplitter with a silicon avalanche photodiode. A half-wave plate was used to rotate the polarization when desired.

The light is endfire coupled into and out-of the waveguide with microscope objectives as shown. An uncoated pellicle beamsplitter is used to send part of the transmitted light to a General Electric CID camera that is sensitive in the near

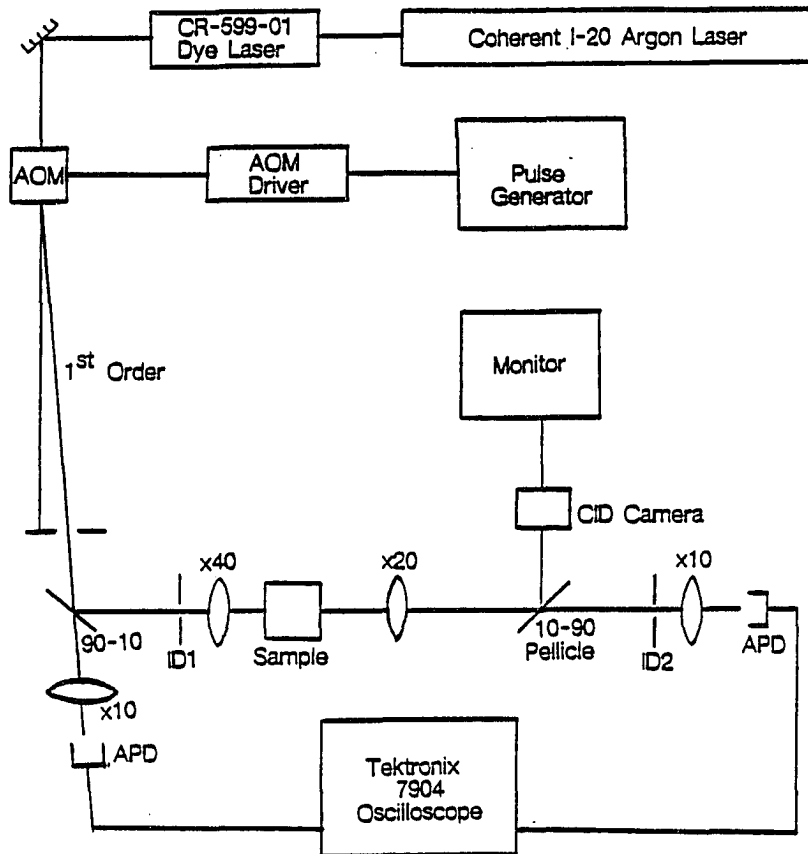


Figure 40. Experimental setup for observation of optical bistability in waveguides.

infrared. The television camera and monitor are essential for alignment and coupling into the waveguides. The remainder of the transmitted beam is incident on another silicon APD. The sample holder is a high-precision XYZ positioner mounted on a two-axis tilting table. The tilting table decreases the rigidity of the mounting somewhat, but the extra degrees of freedom are necessary for waveguide

coupling. The iris diaphragms (ID1 and ID2) are alignment aids. An optical multichannel analyzer was available during the experiments for calibration of the dye laser.

The procedure for coupling light into the waveguide consisted of first obtaining Lloyd's mirror fringes when the waveguides are positioned slightly below the optical axis. The fringes result from interference between the light reflected from the top of the waveguides, and the light propagating straight over the top of the sample. These are an indication that the waveguides are level with respect to the beam and that the focus of the front objective is somewhere in or near the waveguide sample. The front objective focus can be preset to some degree by having the objective tightly focussed at the object plane of the rear objective before inserting the sample, and then backing the front objective off by the length of the sample. (Both objectives were mounted on precision XYZ positioners). The waveguide length was determined with a small microscope with measuring reticle purchased from Edmund Scientific. Having obtained the fringes by adjusting the tilt of the sample, one then locates the presence of waveguides by the distortion they cause in the fringes. At this time it is usually possible to couple into the slab waveguide region between the etched waveguides. Raising the sample into the beam will show a bright line of light propagating through the guiding layer. The front and rear objectives can now be adjusted and the tilt of the sample can be further corrected. If the maximum coupling into the slab occurs higher on the monitor, the sample is tilted down in front. If the maximum coupling is low, the front of the waveguide is high. Coupling of light into the channel waveguides should be observable and the horizontal tilt of the sample can be corrected to get the maximum coupling at the center of the screen. Since the

waveguides were cleaved so short, there was some concern whether we could tell if waveguide confinement was actually occurring. The first waveguide samples clearly had much smaller light spots emerging from their exit faces than when light was transmitted, unguided through the GaAs substrate below. This is a clear indication of light confinement by the waveguides.

The first attempts to see optical bistability were with the ridge waveguides fabricated in the 1.5- $\mu\text{m}$  bulk-GaAs sample. We were unable to observe electronic optical bistability in those waveguides. This may be partly due to the fact that the waveguides were multi-mode in the direction perpendicular to the epitaxial layers. An additional shortcoming was the very thin etch-stop layer which served as an imperfect substrate cladding layer to isolate the guiding region from the substrate. The lack of a top "window" to inhibit carrier recombination should have a similar effect on the carrier lifetime in the waveguides. This would require the use of very short pulses as in the etched etalon array experiments and that capability was no longer available. We were able to observe increasing absorption optical bistability due to thermal shifting of the absorption band edge to longer wavelengths. This is a cavity-less mechanism that relies on the local thermal feedback and has previously been observed in AlGaAs slab waveguides (Walker et al [1985]). The hysteresis loop for thermal increasing-absorption bistability is shown in Figure 41. The waveguide was 200  $\mu\text{m}$  long with a 3- $\mu\text{m}$  wide rib and 0.5  $\mu\text{m}$  etch depth. The operating wavelength was 885 nm. The pulsewidth was 100  $\mu\text{s}$  FWHM for a triangular pulse with a peak power incident onto the waveguide of 70 mW.

It was possible to directly measure the finesse of the waveguide etalons at a given wavelength by measuring the contrast of the Fabry-Perot fringes. The

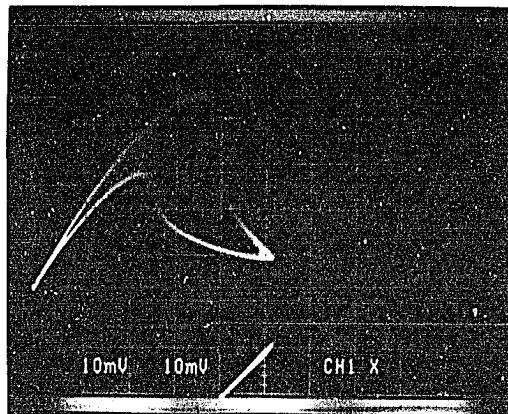


Figure 41. Hysteresis loop for increasing-absorption optical bistability in GaAs ridge waveguide.

contrast could be obtained either by tuning the laser through a free spectral range, or by heating the waveguide with an external light pulse. The effect of the latter technique was to thermally detune the waveguide etalon through a few FSR. The former technique was much simpler and more often used. Straightforward manipulation of equation (1) for a Fabry-Perot etalon for the case of maximum and minimum possible transmitted intensity gives equation (14):

$$\frac{I_{tmax}}{I_{tmin}} = 1 + \frac{4R}{[e^{\alpha L/2} - e^{-\alpha L/2}]^2} = 1 + F \quad (14)$$

The finesse  $F$  can be related to  $F$  by  $F^2 = \pi^2 F/4$  so the finesse can be calculated directly by

$$F = \frac{\pi}{2} \sqrt{\frac{I_{tmax}}{I_{tmin}} - 1},$$

where  $I_{tmax}$  and  $I_{tmin}$  could be obtained directly from measurement of the interference fringe modulation with the oscilloscope. If one assumes a value for  $R$  and that all of the losses are absorptive, one can obtain an effective  $\alpha L$  for the waveguide by simple, iterative solution of equation (14). The waveguides, of course, have other loss mechanisms besides material absorption, but this was still a useful way to compare the performance of the many waveguides that were tested.

There is one last, interesting observation with the GaAs ridge waveguides. Late one night, a hysteresis loop was found with one device that looked like what one expected with electronic bistability. The excitement was dampened when the loop did not show the variation with laser wavelength characteristic of dispersive optical bistability. In trying to get rid of what was assumed to be a phase loop, it was found to disappear and reappear as one moved the output detector in the vertical axis. The hysteresis loop was only present at the top and bottom of the transmitted intensity profile. The acousto-optic modulator was mounted so that the acoustic grating traveled transverse to the table. Consequently, phase error due to acousto-optic modulation is unlikely. The conclusion is that switching was occurring between the guided modes of the waveguide. This nonlinear mode-

switching could be an interesting phenomenon in its own right, but the immediate need was for single-mode devices.

After a suitable sample was obtained from NEC, waveguides based on the strip-loaded design were produced. A large number of actual devices were produced before successfully obtaining bistable operation. Each fabrication step, from photolithography through cleaving and mounting the sample, has the potential for disaster. It was found that checking the mounted waveguides under an optical microscope gave a good correlation between the appearance of a waveguide and its actual performance. This prescreening process saved a lot of time in dealing with many samples.

Waveguides with a MQWS guiding layer and etched to  $0.9 \mu\text{m}$  deep as shown in Figure 33 were successfully operated as optical bistable devices (Warren et al [1987]). The experimental results are shown in Figure 42, which is an oscilloscope trace showing the input and output pulses and a hysteresis loop. The waveguide used for Figure 42 was approximately  $200 \mu\text{m}$  long with a free spectral range of  $5 \text{ \AA}$ . The linewidth of the laser is approximately one angstrom. By scanning the laser through a few Fabry-Perot peaks, the contrast was measured to be 1.5 at  $867 \text{ nm}$ , which corresponds to an absorption of  $56 \text{ cm}^{-1}$ , if the end faces of the guide are assumed to be perfect 30 % reflectors. The exciton resonance of the MQWS sample was measured to be at  $845 \text{ nm}$  for light incident normal to the quantum well layers. For light polarized perpendicular to the quantum well layers, the exciton peak can be expected to be shifted by  $6 \text{ nm}$  to the blue for this well size (Weiner, et al [1985]). The bistable operation was observed over a range of approximately  $10 \text{ nm}$ , centered about the highest contrast operation at  $867 \text{ nm}$ . This is a somewhat larger detuning from the exciton resonance than is

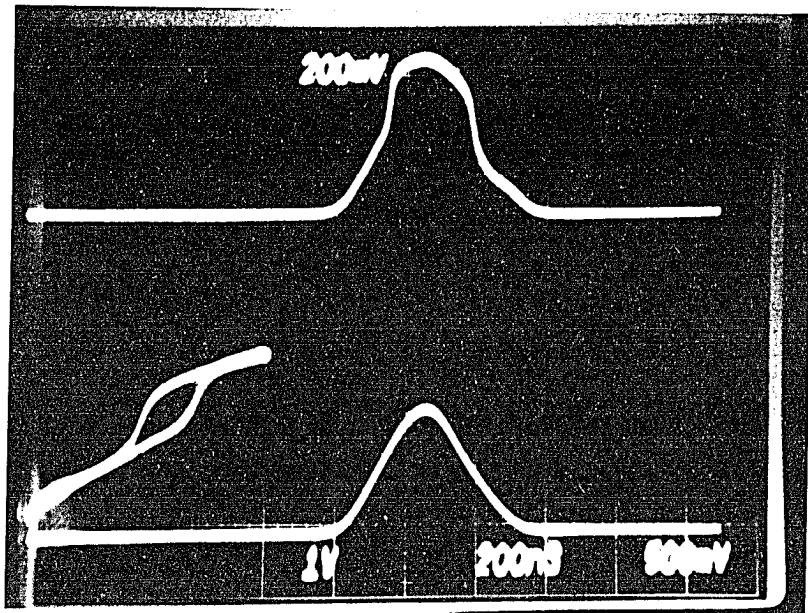


Figure 42. Optical bistability in strip-loaded waveguide. The upper trace is the output pulse and the lower trace is the input pulse of 300ns FWHM. The trace in the lower left is a hysteresis loop for the two pulses.

typical for non-waveguide MQWS etalon devices. The power coupled into the waveguide was estimated to be 60 mW. This is larger than the lowest published values of incident power required for GaAs based etalon devices (5 mW) (Tarnag et al [1984]), yet lower than in the earliest observations (100 mW) (Gibbs et al [1982]). Direct comparison of the devices may not be valid because of the differences in their coupling and loss mechanisms. The estimated coupled power

was arrived at by measuring the incident power and the power transmitted through the waveguide on resonance and measuring the losses in the guide by the previously mentioned Fabry-Perot modulation technique. The unaccounted losses are attributed to the coupling. Since the light was focussed tightly for coupling purposes, the intensities for waveguide operation were much higher than those of the non-waveguide bistability experiments. Two hysteresis loops were observed in some devices, as shown in Figure 43, indicating that the device was switching

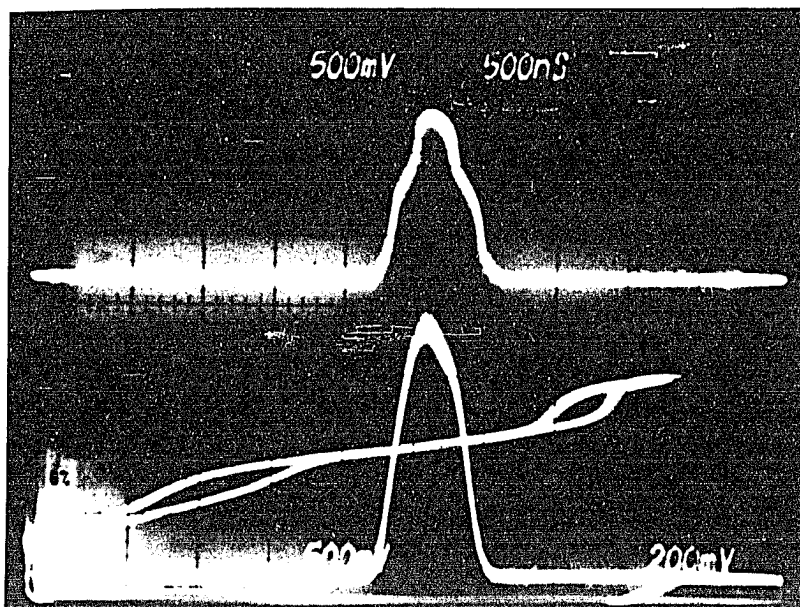


Figure 43. Bistable operation of MQWS waveguide showing switching through two orders of Fabry-Perot transmission.

through two Fabry-Perot transmission orders. This indicates a total phase shift in

the device on the order of  $2\pi$ . This is a very promising observation for future efforts in GaAs nonlinear waveguide devices.

Both thermal and electronic nonlinearities are present in GaAs and GaAs/AlGaAs MQWS materials. The dependence of the switching power on the laser wavelength was used to determine that the nonlinear mechanism was electronic. The index change for electronic processes is negative (the Fabry-Perot transmission shifts to shorter wavelength), and the index change for thermal processes is positive (the Fabry-Perot transmission shifts to longer wavelength). The switching power was observed to increase with decreasing laser wavelength, as is expected for an electronic nonlinear mechanism in GaAs due to the larger detuning through which the Fabry-Perot transmission peak has to be shifted. A thermal mechanism exhibits the opposite dependence. As an additional check, the pulse width was lengthened and the hysteresis was observed to narrow and then reverse direction, indicating the dominance of competing thermal mechanisms. This effect is illustrated in Figure 44. A waveguide exhibiting bistability was operated with pulses of two different pulse lengths: 300 ns and 8  $\mu$ s FWHM. For the longer pulse, the Fabry-Perot transmission peak is shifted by both the electronic and thermal mechanisms after the initial switch-on. Since the shifts are of opposite signs, the switch-off occurs at a higher intensity than the switch-on, yielding a backwards hysteresis loop.

Strip-loaded waveguides were also fabricated from the NEC sample with the bulk GaAs guiding layer. The finesse of the bulk GaAs waveguides was found to be comparable to most of the MQWS guides. The bulk guides showed hysteresis loops that were backwards, indicating that thermal effects were dominating the electronic nonlinearity. The actual incident intensity available at

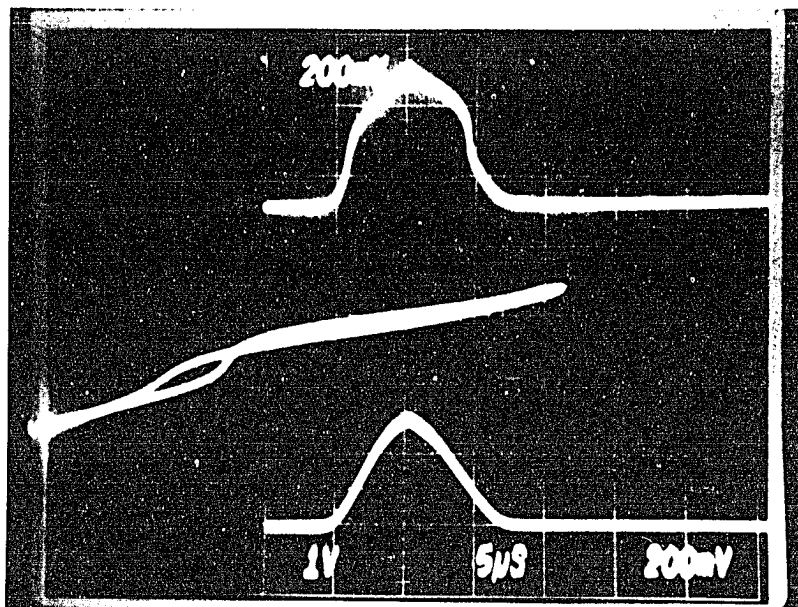


Figure 44. Hysteresis loop showing competition between thermal and electronic nonlinear mechanisms. Lower trace is input pulse of  $8 \mu\text{s}$  FWHM and upper trace is output pulse. Other experimental parameters are same as for Fig. 42.

the operating wavelength (around 900 nm) of the dye laser was less than for the MQWS measurements, but would have been enough to see some forward switching with the MQWS waveguides. It is possible that the nonlinearity of the bulk GaAs is less than the MQWS at those large detunings. More systematic studies are needed to be conclusive.

It is interesting to compare the MQWS waveguide optical bistability results with the predictions of the GaAs etalon model in Figure 23. The much lower

switching power (about 3 mW for a waveguide of  $1\text{-}\mu\text{m}$  X  $3\text{-}\mu\text{m}$  cross section and assuming uniform illumination) and the overshoot in the simulation are indications that the real waveguide losses are a significant factor.

## CONCLUSIONS

Progress in development of GaAs-based nonlinear-optical devices has included the development of fabrication techniques useful for both etalon arrays and waveguide devices, experimental observation of fast logic gating and optical bistability in etalon arrays, and optical bistability in waveguides. Computer modeling was performed with data from the plasma theory that predicted limitations on low-power and high-contrast optimization and high-speed, single-wavelength operation of GaAs etalons.

The fabrication processes for quantum dots and directional couplers were demonstrated. The actual demonstration of the operation of the structures has not been accomplished. A new sample for fabrication of  $800 \text{ \AA}$  quantum dots has been received during the writing of this dissertation. It is anticipated that the physics experiments to be performed will be reported in other dissertations. The progress on the nonlinear directional coupler has been slow. The indications so far are that the physical parameters determined by the fabrication of the NLDC are very critical, and a systematic, empirical attack on the problem will yield results.

The computer modeling that was performed has resulted in some useful, qualitative insight into the operation and limitations of the GaAs etalons. For the studies to go further, particularly to more quantitative properties, will require more systematic experimental testing of the model. A clear understanding of the limits of the model would allow one to apply it to more applied and system-

specific situations as a quick and easy way to test and develop ideas before trying them for real.

It is customary in the conclusions of a dissertation to recommend directions for future research to extend the work completed. Some of the implications of the work reported here are obvious. Reducing carrier lifetime through enhanced surface recombination is a viable approach for fast optical switching devices and such carrier lifetime reductions will be necessary for fast, single-wavelength operation. The development of waveguide fabrication capabilities opens up a whole range of guided-wave devices such as Mach-Zehnder interferometers and ring resonators. It is a short step further to start using electro-optic or mechanical effects to modify the properties of waveguide or etalon devices with fields, current injection, strain etc. The acquisition of semiconductor growth facilities will allow even more flexibility in tailoring the properties of the materials and fabricating new devices. To make good use of such opportunities requires two capabilities. One is an understanding of the needs and important issues of the field that motivates and funds research in nonlinear optical devices and materials. Light has many attributes that make it a desirable means for transporting information. It is obvious that it could be an advantage to do processing, switching or routing of the information in light form without converting to electrical signals. An understanding of what is really needed in a material or device for practical application is an asset in choosing meaningful and significant research directions. The other capability is an intimate understanding of the physics of the materials and devices and of the technology available to manipulate the physics. With both abilities one can come up with new ideas and clear directions and goals.

The emphasis of this dissertation has been on nonlinear optical devices. The devices described here are not yet suitable for the applications envisioned for them. The problems include high power requirements, difficulty of high speed cascading, thermal sensitivity and low switching contrast. The successful development of these devices depends on continued progress in understanding the physics involved and in developing the technology. For example, the fabrication of the quantum dots is an exercise in applying existing, albeit esoteric, technology. The motivation for the fabrication is to study the fundamental physics of semiconductors with such small dimensions. The physics may include isolated absorption features that could allow two-wavelength cascading and high-speed operation with differential gain. In another example, the MQWS waveguide devices that were fabricated for optical bistability now allow the start of studies of the anisotropic properties of MQWS that may yield information on the fundamental mechanisms of MQWS optical nonlinearities, and another possible means of achieving fast, cascading devices with differential gain. Semiconductors are rather unique in having a rich variety of optical and electronic phenomena and a highly developed technology for fabricating, modifying and testing them. Investment in learning new physics opens up new technologies, and investment in technology allows one to learn new physics. Too much emphasis on the application and practicality of what is already developed can weaken this process and end in disappointment what was begun with enthusiasm.

## APPENDIX A

## Program for dynamic optical bistability

```
PROGRAM INB4
C THIS IS SOURCE LISTING OF BISTABILITY SIMULATION
C THIS VERSION USES THE COMPLETE AIRY FUNCTION
C THIS VERSION USES TRIANGLE PULSES
C THIS VERSION USES LINEAR INTERPOLATION OF DATA POINTS
C THIS VERSION FOR EL = 1.4032 ONLY!
C ALFA(N) AND DELTA(N) FOR VALUES N > 10
C FOUND BY INTERPOLATION
C
C
PARAMETER (NDIM=1,NPLOT=4,NPT=500,NPPP=2000,ND=30)
C NPPP=NPLOT*NPT
C
DIMENSION X(NDIM,6),XX(NPPP),YY(NPPP)
DIMENSION Y(ND),DEN(ND),Z(ND),DEN2(ND)
DIMENSION XA(NPLOT,NPT),YA(NPLOT,NPT)
C
CHARACTER *60,XTEXT,YTEXT,HLINE
C
COMMON B,ZL,EMAX,TMAX,EINT,AVINT,PI,TKOEFF,HBAR
```

COMMON/CINT/ALFA,DELTA,DENSITY

C LABELING OF X-AXIS

XTEXT='INPUT INTENSITY IN KW/CM\*CM'

C LABELING OF Y-AXIS

YTEXT='TRANSMITTED INTENSITY IN KW/CM\*CM'

C HEADLINE OF PLOT

HLINE='TR=1.0,EN=1.4032,R=.95'

C

C SAMPLE PARAMETERS

C MIRROR REFLECTIVITY (BOTH ARE SAME)

R=.95

C LENGTH OF ETALON

C DETERMINES DETUNING OF ETALON

ZLM=1.1453

C EXCITATION ENERGY IN eV

EL=.14032E1

C MAXIMUM INTENSITY OF PULSE

EMAX=0.50E5

C LENGTH OF PULSE

TMAX=1.0E-6

C CARRIER RELAXATION TIME

TREL=1.0E-8

WRITE(6,23) R,EL

```
23 FORMAT(1X,'R=',E15.8,' EL=',E15.8)
C
  JPLT=1
  DO 100 J100=1,NPLOT
C TO DO 3 MORE ARBITRARY ETALON LENGTHS
  IF(J100.EQ.2)ZLM=1.1464
  IF(J100.EQ.3)ZLM=1.1486
  IF(J100.EQ.4)ZLM=1.1497
  WRITE(6,24) ZLM
24 FORMAT(1X,'LENGTH ZLM=',E15.8)
C
C INITIAL CONDITIONS
C
  T=0.
  XN0=0.
C HBAR IS IN EV*SEC
  HBAR =6.58296E-16
C INCREMENT IN TIME
C IF TOO LARGE, CALC
C IS UNSTABLE
  DT=1.0E-11
  PI=ACOS(-1.)
  B=TREL
  TKOEFF=1.-R
C CONVERT LENGTH TO CM
```

```
ZL=ZLM*1.E-4
C MUST MAINTAIN CONSTANT DT FOR ALGORITHM IN MOVE
C CALCULATE NUMBER OF ITERATIONS TO USE
  NT=TMAX/DT
C
C
  X(1,1)=XN0
  DO 10 I=1,NDIM
  DO 10 J=2,6
10      X(I,J)=0.
C
C NEED TO DETERMINE THE NUMBER TO DIVIDE
C INTO NT TO GET 500 PTS FOR PLOTTING
  JM=NT/500
      RM=JM
C
C ITERATE THE EQUATIONS
  DO 1 J=1,NT
  CALL MOVE(NDIM,T,X,FX,DT,EL,ND,Y,DEN,Z,DEN2)
  XN=X(1,1)
  TRANS=AVINT*TKOEFF/(2.-TKOEFF)
  IF((J/RM).EQ.INT(J/JM)) THEN
      K=J/JM
C CONVERT INPUT AND OUTPUT INTENSITIES
C TO X10**3 W/SQCM AND
```

C STORE IN ARRAY FOR PLOTTING

XA(JPLT,K)=EINT\*1.602E-22

YA(JPLT,K)=TRANS\*1.602E-22+(JPLT-1)\*1.E1

END IF

1 CONTINUE

101 CONTINUE

100 JPLT=JPLT+1

C

C THE FOLLOWING STATEMENTS ARE NEEDED TO PLOT

CALL TGI(8HTAPE63 ,63)

CALL RESET(3HALL)

DO 50 I=1,NPLOT

DO 51 II=1,NPT

K=(I-1)\*NPT+II

XX(K)=XA(I,II)

51 YY(K)=YA(I,II)

50 CONTINUE

C XX,YY,XMIN,XMAX,YMIN,YMAX,NPOINT=NUMBER OF CURVES \*  
POINTS

C PER CURVE,LINETYPE,NPLOT CURVES,TEXT

CALL DRAW2(XX,YY,0.,50.,0.,50.,NPPP,0,NPLOT,XTEXT,YTEXT,HLINE)

CALL DONEPL

C ABSORPTION AND CHANGE IN INDEX  
 C AS A FUNCTION OF CARRIER DENSITY  
 C DATA  
 C

DATA (Y(M),M=1,30)/.117E4,.117E4,.115E4,  
 \* .991E3,.978E3,.988E3,.109E4,.118E4,.126E4,.133E4,.138E4,  
 \* .142E4,.143E4,.143E4,.1403E4,.136E4,.130E4,.122E4,  
 \* .112E4,.101E4,.881E3,.745E3,.600E3,  
 \* .447E3,.14E2,.8E1,.5E1,0.,0.,0./

DATA (DEN(M),M=1,30)/0.0,0.01,.1,.9,  
 \* 1.,1.1,1.5,2.,2.5,3.,3.5,  
 \* 4.,4.5,5.,5.5,6.,6.5,7.,  
 \* 7.5,8.,8.5,9.,9.5,  
 \* 1.0E1,1.145E1,1.15E1,1.155E1,1.16E1,1.8E1,2.2E1/

DATA (Z(M),M=1,30)/0.,0.,-.446E-3,  
 \* -.696E-2,-.746E-2,-.795E-2,-.856E-2,-.959E-2,-.106E-1,  
 \* -.116E-1,-.127E-1,-.138E-1,-.149E-1,-.161E-1,-.173E-1,  
 \* -.186E-1,-.200E-1,-.213E-1,-.227E-1,  
 \* -.242E-1,-.257E-1,-.272E-1,-.288E-1,-.304E-1,  
 \* -.349E-1,-.350E-1,-.351E-1,-.351E-1,-.351E-1,-.351E-1/

DATA (DEN2(M),M=1,30)/0.,0.01,.1,  
 \* .9,1.,1.1,1.5,2.,2.5,3.,3.5,  
 \* 4.,4.5,5.,5.5,6.,  
 \* 6.5,7.,7.5,8.,8.5,9.,9.5,

```
* 1.0E1,1.145E1,1.15E1,1.155E1,1.16E1,1.8E1,2.2E1/
C
C THIS IS END OF MAIN PROGRAM
C
STOP
END
C
C
SUBROUTINE MOVE(NDIM,T,X,FX,DT,EL,ND,Y,DEN,Z,DEN2)
DIMENSION X(NDIM,6),FX(NDIM),TT(4),C(6)
DIMENSION Y(ND),DEN(ND),Z(ND),DEN2(ND)
C
C SOLUTION OF NDIM 1ST ORDER DIFF EQ
C USING 5TH ORDER NORDSIECK-GEAR ALGORITHM
C A.NORDSIECK, MATH COMP 16, 22 (1962) AND
C A.RAHMAN AND F.H. STILLINGER, JCP 55, 3336 (1971)
C
C NDIM NUMBER OF 1ST ORDER DIF EQ
C T ABSOLUTE TIME
C DT TIME INCREMENT
C X VARIABLES
C FX RHS OF DIF EQ
C
C INITIALIZING CONSTANTS
C
```

C(1)=95./288.

C(2)=1.

C(3)=25./24.

C(4)=35./72.

C(5)=5./48.

C(6)=1./120.

C

C COMPUTE PREDICTORS

DO 400 I=1,NDIM

DO 100 J=2,6

100 X(I,1)=X(I,1)+X(I,J)

DO 200 J=1,3

J1=J+3

HOLD=(J+2)\*1.

200 TT(J)=HOLD\*X(I,J1)

TT(4)=2.\*TT(3)

DO 300 J=1,3

300 X(I,2)=X(I,2)+TT(J)

X(I,2)=X(I,2)+2.\*X(I,3)

X(I,3)=X(I,3)+TT(1)+6.\*X(I,5)+TT(4)

X(I,4)=X(I,4)+TT(2)+TT(4)

X(I,5)=X(I,5)+TT(3)

400 CONTINUE

C

C COMPUTE RHS OF DIF EQ USING PREDICTORS

```

      CALL FORCE(NDIM,T,X,FX,DT,EL,ND,Y,DEN,Z,DEN2)
C
C COMPUTE CORRECTED VALUES
  DO 600 I=1,NDIM
    THETA=FX(I)*DT-X(I,2)
    DO 500 J=1,6
500      X(I,J)=X(I,J)+THETA*C(J)
600      CONTINUE
    T=T+DT
    RETURN
  END
C
C
  SUBROUTINE FORCE(NDIM,T,X,FX,DT,EL,ND,Y,DEN,Z,DEN2)
  DIMENSION X(NDIM,6),FX(NDIM)
  DIMENSION Y(ND),DEN(ND),Z(ND),DEN2(ND)
  COMMON B,ZL,EMAX,TMAX,EINT,AVINT,PI,TKOEFF,HBAR
  COMMON/CINT/ALFA,DELTA,DENSITY
C
C THIS SUBROUTINE COMPUTES RHS OF DIFF EQ
C IS CALLED BY 'MOVE'
  XN=X(1,1)
  DENSITY=XN*1.E-17
  DENS=DENSITY
  CALL LININT(ND,Y,DEN,DENS,ALFA)

```

```

CALL LININT(ND,Z,DEN2,DENS,DELTA)
IF(ALFA.LT.0.)THEN
ALFA=.1
WRITE(6,999)
999  FORMAT(IX,'ALFA HAS BEEN SET TO ARBITRARY VALUE')
END IF
C
C
C
TB=TMAX/2.
TRI=1.-ABS((T-TB)/TB)
EINT=EMAX*TRI*6.242E18
C MAX EINT = EMAX*6.242E18 (CONVERTING TO EV/S*SQCM)
PHASE=(EL*ZL*(3.5+DELTA))/(HBAR*3.E10)
AL=ALFA*ZL/2.
AB=EXP(AL)-(1.-TKOEFF)*EXP(-AL)
  ABSO=AB*AB
DISP=4.*(1.-TKOEFF)*(SIN(PHASE)**2)
AVINT=EINT*TKOEFF*(2.-TKOEFF)/(ABSO+DISP)
FX(1)=-XN/B+(ALFA/EL)*AVINT
RETURN
END
C
C
SUBROUTINE LININT(ND,Y,X,XD,YO)

```

```
DIMENSION Y(ND),X(ND)
C THIS SUBROUTINE TO PERFORM LINEAR
C INTERPOLATION OF DATA
C INPUT PARAMETERS:
C ND=NUMBER OF DATA POINTS AVAILABLE
C X=ND BY 1 ARRAY OF INDEP VAR DATA POINTS
C Y=ND BY 1 ARRAY OF DEP VAR DATA POINTS
C XD=GIVEN INDEP VAR FOR WHICH DEP POINT
C IS NEEDED
C OUTPUT PARAMETERS:
C YO=DEP VAR VALUE INTERPOLATED FROM DATA
C
DO 1 J=1,ND
    DE=0.
    YO=0.
    IF(X(J).GE.XD.AND.X(J-1).LE.XD)THEN
    IF(X(J).EQ.0..AND.X(J-1).EQ.0.)THEN
        YO=Y(J)
    ELSE
        DE=(Y(J)-Y(J-1))/(X(J)-X(J-1))
        YO=(XD-X(J-1))*DE+Y(J-1)
    END IF
    GO TO 2
END IF
1 CONTINUE
```

```
WRITE(6,999) DENS
999          FORMAT(1X,'ERROR IN DATA INTERP AT DENS = ',E15.8)
2 CONTINUE
RETURN
END
C
C FOLLOWING IS GRAPHICS ROUTINE FOR DISSPLA ON CYBER 205
SUBROUTINE DRAW2(X,Y,XMIN,XMAX,YMIN,YMAX,NPTS,
>LINETP,NLINE,XTEXT,YTEXT,HLINE)
C THIS SUBROUTINE PREPARES DATA FOR FIGURES
C TO BE SEEN ON PC-SCREEN AND PLOTTED ON LIGHTWRITER
REAL X(NPTS),Y(NPTS)
CHARACTER *60,XTEXT,YTEXT,HLINE
XMI=XMIN
XMA=XMAX
YMI=YMIN
YMA=YMAX
DO 10 I=1,NPTS
IF(X(I).GT.XMA)XMA=X(I)
IF(X(I).LT.XMI)XMI=X(I)
IF(Y(I).GT.YMA)YMA=Y(I)
IF(Y(I).LT.YMI)YMI=Y(I)
10 CONTINUE
CALL AREA2D(7.5,7.5)
```

```
CALL XNAME(XTEXT,100)
CALL YNAME(YTEXT,100)
CALL HEADIN(HLINE,100,1.,1)
CALL GRAF(XMI,'SCALE',XMA,YMI,'SCALE',YMA)
CALL MARKER(2)
CALL SCLPIC(.15)
TIME1=SECOND()
NH=NPTS/NLINE
DO 20 I=1,NLINE
DO 30 J=1,NH
X(J)=X(J+NH*(I-1))
30 Y(J)=Y(J+NH*(I-1))
20 CALL CURVE(X,Y,NH,LINETP)
TIME2=SECOND()
PRINT*,'PLOT2D BEGIN=',TIME1,' PLOT2D END=',TIME2
CALL ENDPL(0)
RETURN
END
```

## APPENDIX B

Program to calculate differential gain

## PROGRAM GSCAN

```
C THIS PROGRAM CALCULATES ENERGY GAIN
C FOR SCAN OF INPUT PULSE INTENSITIES
C INPUT DATA FILE IS UNIT 4 WITH ABSORPTION
C AND INDEX CHANGES AS
C A FUNCTION OF CARRIER DENSITY
C THIS PROGRAM USES GAUSSIAN PULSES
C THIS PROGRAM WRITES SOME VALUES TO
C OUT6 FOR DIAGNOSTICS
C THIS PROGRAM TO BE USED ON CYBER 205-ALL CAPS
C THIS VERSION USES ONE OR TWO ARBITRARY
C LENGTH AND ENERGY PULSES
C
  PARAMETER (NDIM=1,NPLOT=50,NPT=500,NPPP=500)
C NPPP=NPLOT*NPT
C
  DIMENSION X(NDIM,6),FX(NDIM)
  DIMENSION XX(NPPP),YY1(NPPP),YY2(NPPP),YYI(NPPP),YY3(NPPP)
  DIMENSION YY4(NPPP),YY3B(NPPP)
```

DIMENSION XA(NPLOT,NPT),YA2(NPLOT,NPT),YN(NPLOT,NPT)

DIMENSION YC(NPLOT,NPT),YB1(NPLOT,NPT),YB2(NPLOT,NPT)

DIMENSION YD(NPLOT,NPT)

DIMENSION YY(NPT),XXA(NPT),POUT(NPT)

DIMENSION EN1(NPLOT),EN2(NPLOT),EG(NPLOT)

DIMENSION AG(NPLOT),EMX(NPLOT)

DIMENSION YA1(1,NPT),YE(1,NPT)

REAL Y1(30),Y2(30),Z1(30),Z2(30),DEN1(30),DEN2(30)

C

CHARACTER \*60,XTEX,YTEXI,YTEX1,YTEX2

CHARACTER \*60,YTEXS,YTEXQ,YTEXN,HLIN

CHARACTER \*60,XTEXA,YTEXA,YTEXB,YTEXG,YTEXR

COMMON/COM1/ EL1,EL2,TCEN1,TCEN2,AVINT1,AVINT2

COMMON/COM2/ EINT1,EINT2,PULSE1,PULSE2

COMMON/COM3/ EMAX1,EMAX2,TMAX,TKOEFF1,TKOEFF2

COMMON/COM4/ HBAR,B,ZL,PI

COMMON/COM5/ TIN(500),SWIN(500)

COMMON/COM6/ ND,Y1,Y2,Z1,Z2,DEN1,DEN2

C

C LABELING OF PLOTS

C

C PROGRAM MAKES SEQUENTIAL PLOTS

C UNWANTED PLOTS MUST BE COMMENTED OUT

C

C LABELING OF X-AXIS

XTEX='TIME IN SECONDS'

C LABELING OF Y-AXIS FOR INPUT PULSES

YTEXI='INPUT INTENSITY IN W/CM\*CM'

C LABELING OF X-AXIS

XTEXA='PULSE 2 INTENS IN W/CM\*CM'

C LABELING OF Y-AXIS FOR PULSE 2 ENERGY

YTEXA='INPUT PULSE ENERGY IN J/CM\*CM'

C LABELING OF Y-AXIS FOR TRANSMITTED PULSE ENERGY

YTEXB='TRANSMITTED PULSE ENERGY IN J/CM\*CM'

C LABELING OF Y-AXIS FOR ADDITIVE ENERGY GAIN

YTEXG='TRANS PULSE ADD ENERGY GAIN'

C LABELING OF Y-AXIS FOR ENERGY GAIN RATIO

YTEXR='TRANS PULSE ENERGY GAIN RATIO'

C

C HEADLINE OF PLOT

HLIN='EL1=1.4032,EL2=1.4032,L=2.042,R1=.9,R2=.9,P1=10,20'

C

C

C SAMPLE PARAMETERS, OBTAINED FROM DATA

C FILE LABELED GSCAN.DAT4

C GET DENS,ALFA,DELTA-N VALUES

READ(4,\*) ND

READ(4,\*) (DEN1(I),Y1(I),Z1(I),I=1,ND)

DO 17 I=1,ND

DEN2(I)=DEN1(I)

Y2(I)=Y1(I)

Z2(I)=Z1(I)

17 CONTINUE

C REFLECTIVITY OF FRONT AND BACK MIRRORS

R1=.9

R2=.9

C LENGTH OF ETALON (MICRONS)

C DETERMINES DETUNING OF ETALON

ZLM=2.042

C INPUT BEAM ENERGIES

EL1=.14032E1

EL2=.14032E1

C TWO INPUT PULSES: PULSE 1 IS BIAS PULSE

C PULSE 2 IS SWITCHING PULSE

C SWITCHING PULSE IS SCANNED IN PEAK

C INTENSITY WITH INCREMENT DELTIN

C MAX INTENSITIES OF INPUT PULSES (W/CM\*CM)

EMAX1=425.0E5

EMAX2=.10E5

C SET LIMITS OF INTENSITY OF PULSE 2

P2MAX=100.1E5

P2MIN=EMAX2

P2DEL=P2MAX-P2MIN

C FIND INCREMENT IN INTENSITY OF PULSE 2

```
DELTA=PI*P2DEL/NPLOT
C TMAX SETS THE TIME WINDOW FOR CALCULATION
C TMAX SHOULD BE SET AT LEAST 4X MAXIMUM PULSE FWHM
C MAX TIME FOR PLOTTING ROUTINES
  TMAX=4.0E-11
C PULSE TIME POSITIONS
  TCEN1=2.0E-11
  TCEN2=2.0E-11
C SET PULSE FWHM FOR BOTH PULSES
  PULSE1=1.0E-11
  PULSE2=1.0E-11
C RELAXATION TIME FOR CARRIERS
  TREL=1.0E-8
C
C START LOOP DO CALCULATION FOR EACH INCREMENT
C OF PULSE 2 INTENSITY
  NPLOTS=NPLOT
  IFLAG=0
111      DO 100 J100=1,NPLOTS
  JPLT=J100
C SET INITIAL CONDITIONS
C FOR EACH CALCULATION
  T=0.0E-11
  XN0=0.
C HBAR IS IN EV*SEC
```

```
HBAR =6.58296E-16
C SET TIME INCREMENT:  NEED 1.E4 OR 1.E5 POINTS
C PER CALCULATION TO INSURE NUMERICAL STABILITY
C LONG PULSES NEED DT ≥ 1.E-11
DT=4.0E-15
PI=ACOS(-1.)
B=TREL
TKOEFF1=1.-R1
TKOEFF2=1.-R2
C CONVERT LENGTH TO CM
ZL=ZLM*1.E-4
WRITE(6,193)ZL
193          FORMAT(1X,'ZL=',E15.8)
C MUST MAINTAIN CONSTANT DT FOR ALGORITHM IN MOVE
C CALCULATE NUMBER OF ITERATIONS TO USE
NT=TMAX/DT
C
C NEED TO DETERMINE THE NUMBER TO DIVIDE INTO NT TO GET 500
PTS
C FOR PLOTTING
JM=NT/500
RM=JM
C
C
X(1,1)=XN0
```

```
DO 10 I=1,NDIM
DO 10 J=2,6
10      X(I,J)=0.
C
C
C
C
C INCREMENT INTENSITY OF PULSE 2
      IF(J100.GT.1)EMAX2=EMAX2+DELTIN
      WRITE(6,24)EMAX2
24 FORMAT(1X,'PULSE 2 INTENSITY =',E15.8)
      EMX(J100)=EMAX2
C
C
C ITERATE THE EQUATIONS
DO 1 J=1,NT
CALL MOVE(NDIM,T,X,FX,DT)
XN=X(1,1)
TRANS1=A VINT1*TKOEFF1/(2.-TKOEFF1)
TRANS2=A VINT2*TKOEFF2/(2.-TKOEFF2)
IF((J/RM).EQ.INT(J/JM)) THEN
      K=J/JM
      IF(K.LT.1.OR.K.GT.NPT) GOTO 1
C CONVERT INPUT AND OUTPUT INTENSITIES TO W/SQCM AND
C STORE IN ARRAY FOR PLOTTING
```

```
IF(IFLAG.NE.1)THEN
      XA(JPLT,K)=J*DT
      YA1(1,K)=EINT1*1.602E-19
      YA2(JPLT,K)=EINT2*1.602E-19
      YC(JPLT,K)=(TRANS1+TRANS2)*1.602E-19
ELSE
      YE(1,K)=TRANS1*1.602E-19
END IF
END IF
1 CONTINUE
      WRITE(6,293)J100
293      FORMAT(1X,'J100=',I3)
C
C FOLLOWING LINES ARE TO CALCULATE
C INTEGRATED ENERGY GAIN
C ENERGIES ARE IN J/cm*cm
C
      IF(IFLAG.NE.1)THEN
C EN1 IS PULSE 1 ENERGY
      EN1(J100)=0.0
      DO 670 L=1,NPT
670      EN1(J100)=EN1(J100)+(JM*DT*YA2(J100,L))
C EN2 IS PULSE 2 ENERGY
      EN2(J100)=0.0
```

```
DO 681 II=1,NPT
681      EN2(J100)=EN2(J100)+(JM*DT*YC(J100,II))
      ELSE
C EN3 IS TRANSMITTED PULSE ENERGY
      EN3=0.
      DO 685 LL=1,NPT
685      EN3=EN3+JM*DT*YE(1,LL)
      END IF
C
C
100      CONTINUE
C
C THE FOLLOWING LINES ARE TO CALC THE TRANS W/O SW PULSE
      IF(IFLAG.NE.1)THEN
      EMAX2=0.
      NPLOTS=1
      IFLAG=1
      GOTO 111
      END IF
C
      DO 691 JL=1,NPLOT
      AG(JL)=EN2(JL)-EN3
691      EG(JL)=AG(JL)/EN1(JL)
C
C THE FOLLOWING STATEMENTS ARE NEEDED TO PLOT
```

```
CALL TGI(8HTAPE63 ,63)
CALL RESET(3HALL)
C
I=1
DO 61 II=1,NPT
K=II
XXA(K)=XA(I,II)
YY(K)=YA1(I,II)
61 CONTINUE
C
C
C FOLLOWING SUBROUTINE CALLS ARE TO DO PLOTS
C COMMENT OUT UNWANTED PLOTS
C XX,YY,XMIN,XMAX,YMIN,YMAX,NPOINT=NUMBER OF CURVES * POINTS
C PER CURVE,LINETYPE,NPLOT CURVES,TEXT
C
C TO PLOT INPUT PULSE 1 VS TIME
CALL DRAW2(XXA,YY,0.,TMAX,0.,50.,NPT,0,1,XTEX,YTEX1,HLIN)
C
C TO PLOT PULSE 2 ENERGY VS MAX PULSE 2 INTENSITY
CALL DRAW2(EMX,EN1,100.E5,100.E5,0.,2.E-4,NPLOT,0,1,
*XTEXA,YTEXA,HLIN)
C
C TO PLOT TRANS ENERGY VS MAX PULSE 2 INTENSITY
C CALL DRAW2(EMX,EN2,100.E5,100.E5,0.,1.E-3,NPLOT,0,1,
```

```
C  *XTEXA,YTEXB,HLIN)
C
C TO PLOT ADD ENERGY GAIN VS PULSE 2 INTENSITY
  CALL DRAW2(EMX,AG,100.E5,100.E5,0,..5E-3,NPLOT,0,1,
    *XTEXA,YTEXG,HLIN)
C
C TO PLOT ENERGY GAIN RATIO VS PULSE 2 INTENSITY
  CALL DRAW2(EMX,EG,100.E5,100.E5,0.,10.,NPLOT,0,1,
    *XTEXA,YTEXR,HLIN)
C TO PLOT OUTPUT ENERGY VS INPUT ENERGY
  CALL DRAW2(EN1,EN2,0.,2.5E-4,0.,2.5E-4,NPLOT,0,1,
    *YTEXA,YTEXB,HLIN)
C
  CALL DONEPL

C THIS IS END OF MAIN PROGRAM
C
  STOP
  END
C
C
  SUBROUTINE MOVE(NDIM,T,X,FX,DT)
  DIMENSION X(NDIM,6),FX(NDIM),TT(4),C(6)
C
C SOLUTION OF NDIM 1ST ORDER DIFF EQ
```

```
C USING 5TH ORDER NORDSIECK-GEAR ALGORITHM
C A.NORDSIECK, MATH COMP 16, 22 (1962) AND
C A.RAHMAN AND F.H. STILLINGER, JCP 55, 3336 (1971)
C
C NDIM  NUMBER OF 1ST ORDER DIF EQ
C T     ABSOLUTE TIME
C DT    TIME INCREMENT
C X     VARIABLES
C FX    RHS OF DIF EQ
C
C INITIALIZING CONSTANTS
C
C(1)=95./288.
C(2)=1.
C(3)=25./24.
C(4)=35./72.
C(5)=5./48.
C(6)=1./120.
C
C COMPUTE PREDICTORS
DO 400 I=1,NDIM
DO 100 J=2,6
100      X(I,1)=X(I,1)+X(I,J)
DO 200 J=1,3
J1=J+3
```

```
HOLD=(J+2)*1.  
200      TT(J)=HOLD*X(I,J1)  
      TT(4)=2.*TT(3)  
      DO 300 J=1,3  
300      X(I,2)=X(I,2)+TT(J)  
      X(I,2)=X(I,2)+2.*X(I,3)  
      X(I,3)=X(I,3)+TT(1)+6.*X(I,5)+TT(4)  
      X(I,4)=X(I,4)+TT(2)+TT(4)  
      X(I,5)=X(I,5)+TT(3)  
400      CONTINUE  
C  
C COMPUTE RHS OF DIF EQ USING PREDICTORS  
      CALL FORCE(NDIM,T,X,FX,DT)  
C  
C COMPUTE CORRECTED VALUES  
      DO 600 I=1,NDIM  
      THETA=FX(I)*DT-X(I,2)  
      DO 500 J=1,6  
500      X(I,J)=X(I,J)+THETA*C(J)  
600      CONTINUE  
      T=T+DT  
      RETURN  
      END  
C  
C
```

```

SUBROUTINE FORCE(NDIM,T,X,FX)
DIMENSION X(NDIM,6),FX(NDIM)
DIMENSION Y1(30),Y2(30),Z1(30),Z2(30),DEN1(30),DEN2(30)
COMMON/COM1/ EL1,EL2,TCEN1,TCEN2,AVINT1,AVINT2
COMMON/COM2/ EINT1,EINT2,PULSE1,PULSE2
COMMON/COM3/ EMAX1,EMAX2,TMAX,TKOEFF1,TKOEFF2
COMMON/COM4/ HBAR,B,ZL,PI
COMMON/COM5/ TIN(500),SWIN(500)
COMMON/COM6/ ND,Y1,Y2,Z1,Z2,DEN1,DEN2

```

C

C

C THIS SUBROUTINE COMPUTES RHS OF DIF EQ, CALLED BY 'MOVE'

```

XN=X(1,1)
DENSITY=XN*1.E-17
DENS=DENSITY
IF(DENS.LE.1.6E1)THEN
CALL LININTV(ND,Y1,DEN1,DENS,ALFA1)
CALL LININTV(ND,Z1,DEN1,DENS,DELTA1)
CALL LININTV(ND,Y2,DEN2,DENS,ALFA2)
CALL LININTV(ND,Z2,DEN2,DENS,DELTA2)
ELSE
CALL LININTV(ND,Y1,DEN1,1.6E1,ALFA1)
CALL LININTV(ND,Z1,DEN1,1.6E1,DELTA1)
CALL LININTV(ND,Y2,DEN2,1.6E1,ALFA2)
CALL LININTV(ND,Z2,DEN2,1.6E1,DELTA2)

```

```
WRITE (6,299) XN,T
299      FORMAT(1X,'N SET TO 1.6E18 AT N=',E15.8,' T=',E15.8)
      END IF
      IF(ALFA1.LE.0.)THEN
      ALFA1=.1
      WRITE(6,999)
999      FORMAT(1X,'ALFA1 HAS BEEN SET TO ARBITRARY VALUE')
      END IF
      IF(ALFA2.LE.0.)THEN
      ALFA2=.1
      WRITE(6,998)
998      FORMAT(1X,'ALFA2 HAS BEEN SET TO ARBITRARY VALUE')
      END IF
C
C USING GAUSSIAN PULSE SHAPE FOR PULSE 1
C
      XPON1=2.0E0*((T-TCEN1)*4.697E-1)/PULSE1
      GAUS1=EXP(-PI*(XPON1**2))
      EINT1=EMAX1*GAUS1*6.242E18
C
C
C USING GAUSSIAN PULSE SHAPE FOR PULSE 2
C
      XPON2=2.0E0*((T-TCEN2)*4.697E-1)/PULSE2
      GAUS2=EXP(-PI*(XPON2**2))
```

EINT2=EMAX2\*GAUS2\*6.242E18

C

C MAX EINT = EMAX\*6.242E18 (CONVERTING TO EV/S\*SQCM)

C

C FOLLOWING IS CALCULATION OF ETALON AIRY EQUATION

PHASE1=(EL1\*ZL\*(3.5+DELTA1))/(HBAR\*3.E10)

PHASE2=(EL2\*ZL\*(3.5+DELTA2))/(HBAR\*3.E10)

AL1=ALFA1\*ZL/2.

AL2=ALFA2\*ZL/2.

AB1=EXP(AL1)-(1.-TKOEFF1)\*EXP(-AL1)

AB2=EXP(AL2)-(1.-TKOEFF2)\*EXP(-AL2)

ABSO1=AB1\*\*2

ABSO2=AB2\*\*2

DISP1=4.\*(1.-TKOEFF1)\*(SIN(PHASE1)\*\*2)

DISP2=4.\*(1.-TKOEFF2)\*(SIN(PHASE2)\*\*2)

TEST1=ABSO1+DISP1

IF(TEST1.LE.0.0)THEN

WRITE(6,99)TEST1

99 FORMAT(1X,'TEST1=',E15.8)

END IF

TEST2=ABSO2+DISP2

IF(TEST2.LE.0.0)THEN

WRITE(6,98)TEST2

98 FORMAT(1X,'TEST2=',E15.8)

END IF

```

AVINT1=EINT1*TKOEFF1*(2.-TKOEFF1)/(ABSO1+DISP1)
AVINT2=EINT2*TKOEFF2*(2.-TKOEFF2)/(ABSO2+DISP2)
FX(1)=-XN/B+(ALFA1/EL1)*AVINT1+(ALFA2/EL2)*AVINT2

```

C

```

RETURN

```

```

END

```

C

C

```

SUBROUTINE LININTV(ND,Y,X,XD,YO)

```

```

DIMENSION Y(ND),X(ND)

```

C THIS SUBROUTINE TO PERFORM LIN INTERP OF DATA

C VECTORIZED VERSION FOR USE ON CYBER 205

C INPUT PARAMETERS:

C ND=NUMBER OF DATA POINTS AVAILABLE

C X=ND BY 1 ARRAY OF INDEP VAR DATA POINTS

C Y=ND BY 1 ARRAY OF DEP VAR DATA POINTS

C XD=GIVEN INDEP VAR FOR WHICH DEP POINT

C IS NEEDED

C OUTPUT PARAMETERS:

C YO=DEP VAR VALUE INTERPOLATED FROM DATA

C

```

ID=1

```

```

IF(XD.LT.X(2)) GOTO 3

```

```

IF(XD.GE.X(ND)) GOTO 4

```

```

ID=Q8SGE(X(1;ND),XD)

```

```
3      DE=(Y(ID+1)-Y(ID))/(X(ID+1)-X(ID))
      YO=(XD-X(ID))*DE+Y(ID)
      GOTO 5
4      YO=Y(ND)
5      RETURN
      END
```

C

C FOLLOWING IS GRAPHICS ROUTINE FOR DISSPLA ON CYBER 205

C

```
      SUBROUTINE DRAW2(X,Y,XMIN,XMAX,YMIN,YMAX,NPTS,
>LINETP,NLINE,XTEXT,YTEXT,HLINE)
C THIS SUBROUTINE PREPARES DATA FOR FIGURES
C TO BE SEEN ON PC-SCREEN AND PLOTTED ON LIGHTWRITER
      REAL X(NPTS),Y(NPTS)
      CHARACTER *60,XTEXT,YTEXT,HLINE
      XMI=XMIN
      XMA=XMAX
      YMI=YMIN
      YMA=YMAX
      DO 10 I=1,NPTS
      IF(X(I).GT.XMA)XMA=X(I)
      IF(X(I).LT.XMI)XMI=X(I)
      IF(Y(I).GT.YMA)YMA=Y(I)
      IF(Y(I).LT.YMI)YMI=Y(I)
```

```
10 CONTINUE
   CALL AREA2D(7.5,7.5)
   CALL XNAME(XTEXT,100)
   CALL YNAME(YTEXT,100)
   CALL HEADIN(HLINE,100,1.,1)
   CALL GRAF(XMI,'SCALE',XMA,YMI,'SCALE',YMA)
   CALL MARKER(2)
   CALL SCLPIC(.15)
   TIME1=SECOND()
   NH=NPTS/NLINE
   DO 20 I=1,NLINE
     DO 30 J=1,NH
       X(J)=X(J+NH*(I-1))
30  Y(J)=Y(J+NH*(I-1))
20  CALL CURVE(X,Y,NH,LINETP)
     TIME2=SECOND()
     PRINT*,'PLOT2D BEGIN=',TIME1,' PLOT2D END=',TIME2
     CALL ENDPL(0)
     RETURN
   END
```

## APPENDIX C

### Photolithography Recipe

#### Cleaning

Ultrasonic cleaning in acetone for 15 minutes. Rinse and ultrasonic cleaning in methanol for 15 minutes (not always necessary). Rinse ultrasonic cleaning in deionized water for 10 minutes. Be sure to clean tweezers too. Sample is clean if water wets surface evenly. Blow off water solvents with filtered, dry N<sub>2</sub>. Bake samples for 30 minutes at 90 °C. Let cool for a few minutes before further processing. Always prepare some dummy samples for testing exposure, development, etc.

#### Spinning

This is assuming KTI 820 diluted to 27 centistokes at room temperature. Set spinner for 9000 rpm and 30 seconds duration. This will vary with desired thickness of photoresist. Always handle photoresist under yellow lights, since it is photosensitive to blue light. Turn on vacuum pump. Carefully place sample on spinner's vacuum chuck. Turn on foot switch. Check and adjust the rpm readout. While spinning, blow off sample with filtered, dry N<sub>2</sub>. Spinner will automatically turn off after set time, or you can hit foot switch a second time. Drop photoresist on sample with medicine dropper and immediately start spinner. After spinning is complete, pick up the sample by one corner with tweezers. This is a delicate operation. Usually the sample is stuck to the chuck with

photoresist. Move the sample carefully with the tip of the tweezers until one corner is hanging over the edge of the chuck. When finished with all samples, clean spinner with acetone. Be very careful about letting photoresist or other viscous materials down the vacuum chuck. Repair of the spinner motor will be necessary and expensive.

### **Prebake**

Bake the samples at 90 °C for 30 minutes to harden photoresist layer. This must be done consistently from sample to sample. Cool sample for a few minutes before next processing.

### **Exposure**

Exposure and development are best attempted with two people. The exposure system should be allowed to warm up for an hour or two. Vacuum chuck and its O-ring should be clean. Mask must be cleaned same as for the samples. Mask must be cleaned after exposure of a few samples because it quickly accumulates residue from contact with the photoresist. Check light intensity with the UV power meter. The exposure lamp projects a disk about three inches in diameter. Measure the intensity at center and four compass points in disk with both detector heads. If the intensity is not very uniform, the exposure lamp can be adjusted. The center of the beam is the usual place to put the mask pattern that will be exposed. The empirical formula (using the center value from the exposure meter) for the approximate exposure time is:

$$\text{Exposure time (sec)} = \frac{100}{\text{measured intensity (mW/cm}^2\text{) with 405nm head}}$$

The exposure time must be checked by making dummy runs before the real sample exposure.

Set the exposure time on the shutter timer. (The shutter timer is normally set for 0-99.9 seconds duration for exposing photoresist. It is possible to remove it from the metal chassis and set several different ranges for other uses.) Place the sample on the vacuum chuck. Make sure O-ring is in its groove. Place mask on O-ring and check alignment of mask pattern you want to use with the sample, without touching the sample yet. Turn on vacuum pump and press mask firmly against sample to seal the vacuum. You can tell from the sound of the pump is O-ring is sealing. Observe the interference fringes between the mask surface and the sample surface with the yellow light. If you are getting good, even contact, the fringes will be well centered and almost circular. It will probably be necessary to put a shim under the sample or mask to even the contact. Scotch-brand double-sided foam tape for mounting posters has made very good shims. Place vacuum chuck under lamp housing so that sample is in the center and turn on the timer. After exposure, the vacuum pump is turned off and the mask should be put back in its box. Do not let the sample get exposed to room light until after development, which should be done immediately following exposure of the samples.

### Development

The developer is KTI 932 diluted 1:1 with deionized water. Prepare a small beaker of developer solution, and one with deionized water for rinsing. Dip the

sample into the developer with tweezers and start timing immediately. Sample can be agitated gently. Watch the surface of the sample. The surface of the sample will show a visible change when the photoresist develops, and the photoresist can be seen streaming into solution. Wait 10 seconds after photoresist stops dissolving. Total development time should be 20-45 seconds if the exposure time is correct. Rinse sample for about 30 seconds in deionized water. Blow sample dry with  $N_2$ .

#### **Post-bake**

Bake the samples for 30 minutes at 115 °C. Recommended temperature from KTI is higher, but there is some possibility of GaAs reacting with photoresist. After baking, the sample is ready for etching. The samples can be stored in very clean place, but post-bake should be repeated for 5 minutes to remove adsorbed moisture.

## REFERENCES

- Adachi, S., *J. Appl. Phys.* **58**, R1 (1985)
- Alperovich, V.L., V.M. Zaletin, A.F. Kravchenko and A.S. Terekhov, *Phys. Stat. Sol. (b)* **77**, 465 (1976)
- Banyai, L. and S.W. Koch, *Z. Phys. B-Condensed Matter* **63**, 283 (1986)
- Banyai, L. and S.W. Koch, *Phys. Rev. Lett.* **57**, 2722 (1986)
- Bischofberger, T. and Y.R. Shen, *Phys. Rev. A* **19**, 1169 (1979)
- Bondur, J.A., *J. Vac. Sci. Technol.* **13**, 1023 (1976)
- Born, M. and E. Wolf, Principles of Optics, 4th ed. (Pergamon, New York, 1970)
- Burton, R.H., R.A. Gottscho and G. Smolinsky in Dry Etching for Microelectronics ed. by R.A. Powell (North Holland, New York, 1984)
- Casey, H.C. and M. B. Panish, Heterostructure Lasers, Part A (Academic, New York, 1978)
- Chapman, B., Glow Discharge Processes (John Wiley, New York, 1980)
- Chemla, D.S., D.A.B. Miller, P.W. Smith, A.C. Gossard and W. Wiegmann, *IEEE J. Quant. Electron.* **QE-20**, 265 (1984)
- Coburn, J.W., Plasma Etching and Reactive Ion Etching (Am. Vac. Soc. Monograph Series, New York, 1982)
- Dow, J.D. and D. Redfield, *Phys. Rev. B* **5**, 594 (1972)
- Elliott, R.J., *Phys. Rev.* **108**, 1384 (1957)
- Fehrenbach, G.W., W. Schafer, J. Treusch and R.G. Ulbrich, *Phys. Rev. Lett.* **49**, 1281 (1982)
- Furuta, H., H. Noda and A. Ihaya, *Appl. Opt.* **13**, 322 (1974)
- Gibbons, W., dissertation, University of Arizona (1987)
- Gibbons, W. and D. Sarid, *Appl. Phys. Lett.* **51**, 403 (1987)

- Gibbs, H.M. Optical Bistability: Controlling Light With Light (Academic Press, New York, 1985)
- Gibbs, H.M., S.L. McCall, T.N.C. Venkatesan, A.C. Gossard, A. Passner and W. Wiegmann, *Appl. Phys. Lett.* **35**, 451 (1979)
- Gibbs, H.M., S.S. Tarng, J.L. Jewell, D.A. Weinberger, K. Tai, A.C. Gossard, S.L. McCall, A. Passner and W. Wiegmann, *Appl. Phys. Lett.* **41**, 221 (1982)
- Goell, J.E., *Appl. Opt.* **12**, 2797 (1973)
- Haug, H., Nonlinear Optical Properties of Semiconductors (Academic Press, New York, 1988)
- Haug, H. and S. Schmitt-Rink, *Progr. Quant. Electron.* **9**, 3 (1984)
- Haug, H. and S. Schmitt-Rink, *J. Opt. Soc. Am. B* **2**, 1135 (1985)
- Hendricks, D.R., MS thesis, University of Arizona (1987)
- Hikosaka, K., T. Mimura and K. Joshin, *Jpn. J. Appl. Phys.* **20**, L847 (1981)
- Hogsdon, J.N., Optical Absorption and Dispersion in Solids (Chapman and Hill, London, 1970)
- Jewell, J.L., dissertation, University of Arizona (1984)
- Jewell, J.L., H.M. Gibbs, A.C. Gossard, A. Passner and W. Wiegmann, *Mat. Lett.* **1**, 148 (1983)
- Jewell, J.L., Y.H. Lee, J.F. Duffy, A.C. Gossard and W. Wiegmann, *Appl. Phys. Lett.* **48**, 1342 (1986)
- Jewell, J.L., Y.H. Lee, M. Warren, H.M. Gibbs, N. Peyghambarian, A.C. Gossard and W. Wiegmann, *Appl. Phys. Lett.* **46**, 918 (1985)
- Jewell, J.L., A. Scherer, S.L. McCall, A.C. Gossard and J.H. English, Technical Digest, Conferences on Lasers and Electro-Optics (Optical Society of America, 1987) pg. 348
- Karpushko, F.V. and G.V. Sinitsyn, *Zh. Prikl. Spektros.* **29**, 820 [J. Appl. Spectrosc. USSR **29**, 1323] (1978)
- King, M.C. in VLSI Electronics Microstructure Science, Vol. 1 ed. by N.G. Einspruch (Academic Press, New York, 1981)
- Kirby, P.A., P.R. Selway and L.D. Westbrook, *J. Appl. Phys.* **50**, 4567 (1979)

- Koch, S.W., N. Peyghambarian and H.M. Gibbs, to be published *Appl. Phys. Rev.* Jan. (1988)
- Kogelnick, H. in Integrated Optics, 2nd ed., edited by T. Tamir (Springer-Verlag, New York, 1985)
- Lee, Y.H., A. Chavez-Pirson, S.W. Koch, H.M. Gibbs, S.H. Park, J. Morhange, N. Peyghambarian, L. Banyai, A.C. Gossard and W. Wiegmann, *Phys. Rev. Lett.* 57, 2446 (1987)
- Lee, Y.H., H.M. Gibbs, J.L. Jewell, J.F. Duffy, T. Venkatesan, A.C. Gossard, W. Wiegmann and J.H. English, *Appl. Phys. Lett.* 49, 486 (1986)
- Lee, Y.H., M. Warren, G.R. Olbright, H.M. Gibbs, N. Peyghambarian, T. Venkatesan, J.S. Smith and A. Yariv, *Appl. Phys. Lett.* 48, 754 (1986)
- LePore, J.J., *J. Appl. Phys.* 51, 6441 (1980)
- Li Kam Wa, P., P.N. Robson, J.P.R. David, G. Hill, P. Mistry, M.A. Pate and J.S. Roberts, *Electron. Lett.* 22, 1129 (1986)
- Littman, M.G. and H.J. Metcalf, *Appl. Opt.* 17, 2224 (1978)
- Ma, S., Modern Theory of Critical Phenomena (Benjamin/Cummings, Reading, 1976)
- McCall, S.L., H.M. Gibbs, G.G. Churchill and T.N.C. Venkatesan, *Bull. Am. Phys. Soc.* 20, 636 (1975)
- Melliard-Smith, C.M. and C.J. Mogab in Thin Film Processes, ed. by J.L. Vossen and W. Kern (Academic Press, New York, 1978)
- Migus, A., A. Antonetti, D. Hulin, A. Mysyrowicz, H.M. Gibbs, N. Peyghambarian and J.L. Jewell, *Appl. Phys. Lett.* 46, 70 (1985)
- Miller, D.A.B., *IEEE J. Quant. Electron.* QE-17, 306 (1981)
- Miller, D.A.B., S.D. Smith and A. Johnston, *Appl. Phys. Lett.* 35,658 (1979)
- Mott, N.F., Metal-Insulator Transitions (Taylor and Francis, London, 1974)
- Newman, R. ed., Fine Line Lithography (North Holland, New York, 1980)
- Park, S.H., J.F. Morhange, A.D. Jeffery, R.A. Morgan, A. Chavez-Pirson, H.M. Gibbs, S.W. Koch, N. Peyghambarian, M. Derstine, A.C. Gossard, J.H. English and W. Wiegmann, submitted to *Appl. Phys. Lett.*

- Powell, R.A. and D.F. Downey in Dry Etching for Microelectronics, ed. by R.A. Powell, (North Holland, New York, 1984)
- Ramaswamy, V., Bell Sys. Tech. J. 53, 697 (1974)
- Sahlen, O., U. Olin, E. Masseboeuf, G. Lundgren and M. Rask, Appl. Phys. Lett. 50, 1559 (1987)
- Schmitt-Rink, S., D.S. Chemla and D.A.B. Miller, Phys. Rev. B 32, 6601 (1985)
- Silberberg Y., P.W. Smith, D.A.B. Miller, B. Tell, A.C. Gossard and W. Wiegmann, Appl. Phys. Lett. 46, 701 (1985)
- Smith, S.D., A.C. Walker, F.A.P. Tooley and B.S. Wherret, Nature 325, 27 (1987)
- Smolinsky, G., R.P. Chang and T.M. Mayer, J. Vac. Sci. Technol. 18, 12 (1981)
- Somekh, S., E. Garmire, A. Yariv, H.L. Garvin and R.G. Hunsperger, Appl. Opt. 13, 327 (1974)
- Sumi, H. and Y. Toyozawa, J. Phys. Soc. Japan 31, 342 (1971)
- Tai, K., J.V. Moloney and H.M. Gibbs, Opt. Lett. 1, 429 (1982)
- Tamura, H. and H. Kurihara, Jpn. J. Appl. Phys. 23, L731 (1984)
- Tarng, S.S., H.M. Gibbs, J.L. Jewell, N. Peyghambarian, A.C. Gossard, T. Venkatesan and W. Wiegmann, Appl. Phys. Lett. 44, 360 (1984)
- Tihany, P., D.K. Wagner, H.J. Vollmer, A.J. Roza, C.M. Harding, R.J. Davis and E.D. Wolf, Appl. Phys. Lett. 50, 1640 (1987)
- Urbach, F., Phys. Rev. 92, 1324 (1953).
- Venkatesan, T., B. Wilkens, Y.H. Lee, M. Warren, G. Olbright, H.M. Gibbs, N. Peyghambarian, J.S. Smith and A. Yariv, Appl. Phys. Lett. 48, 145 (1986)
- Walker, A.C., J.S. Aitchinson, S. Ritchie and P.M. Rodgers, Electron. Lett. 21, 26 (1985)
- Warren, M., Y.H. Lee, G.R. Olbright, B.P. McGinnis, H.M. Gibbs, N. Peyghambarian, T. Venkatesan, B. Wilkens, J. Smith and A. Yariv, pg. 42 in Optical Bistability III, ed. by H.M. Gibbs, P. Mandel, N. Peyghambarian and S.D. Smith (Springer-Verlag, New York, 1986)
- Warren, M., W. Gibbons, K. Komatsu, D. Sarid, D. Hendricks, H.M. Gibbs and M. Sugimoto, Appl. Phys. Lett. 51, 1209 (1987)

Warren, M.E., S.W. Koch and H.M. Gibbs, *Computer* **20** 12, 68 (1987)

Warren, M., D. Richardson, S.W. Koch and H.M. Gibbs, to be published *SPIE Proceedings*

Weiner, J.S., D.S. Chemla, D.A.B. Miller, H.A. Haus, A.C. Gossard, W. Wiegmann and C.A. Burrus, *Appl. Phys. Lett.* **47**, 664 (1985)